ISSUES SURROUNDING FRACTURING OF GEOTHERMAL SYSTEMS – PREDICTING THERMAL CONDUCTIVITY OF RESERVOIR ROCKS AND EVALUATING PERFORMANCE OF FRACTURE PROPPANTS

by

Daniel Brinton

A thesis submitted to the faculty of
the University of Utah
in partial fulfillment of the requirements for the degree of

Master of Science

Department of Chemical Engineering

The University of Utah

August 2011

The University of Utah Graduate School

STATEMENT OF THESIS APPROVAL

The thesis of **Daniel Brinton**

has been approved by the following supervisory committee members:

John McLennan	, Chair	**5/12/2011** Date Approved
JoAnn Lighty	, Member	**5/12/2011** Date Approved
Joseph Moore	, Member	**5/12/2011** Date Approved

and by **JoAnn Lighty** , Chair of

the Department of **Chemical Engineering**

and by Charles A. Wight, Dean of The Graduate School.

ABSTRACT

Traditional geothermal systems have been limited to geologic systems in which elevated temperatures, abundant water, and high porosity and permeability are found. Engineered geothermal systems (EGS) have been proposed for thermal reservoirs in which insufficient water and/or permeability are present. The EGS model calls for the creation of large fracture networks which penetrate the hot rock resource. These fracture networks are formed by reopening sealed fractures or by creating new fractures using hydraulic fracturing methods common to the oil and gas industry. Application of hydraulic fracturing technologies in geothermal systems and operation of engineered geothermal systems present new issues including the formation of thermal fractures due to temperature differentials and rock shrinkage; and the performance of hydraulic fracturing materials such as proppants under geothermal conditions.

The formation of thermal fractures in a geothermal reservoir will be governed by the thermophysical properties of the reservoir rock, including heat capacity, thermal conductivity, coefficient of thermal expansion, etc. Thermal conductivity may be estimated using data obtained from geophysical well logs. Multivariate data analysis methods such as principal components analysis and regression analysis have been used to interpret log data. Significant discrepancies between experimentally-determined thermal conductivity and model-derived thermal conductivity were noted. Possible sources of the

discrepancies include rock anisotropy and insufficient data. However, principal components analysis proved to be a valuable resource for data interpretation.

The resilience of proppants under geothermal conditions was evaluated. Three proppant types were tested in the presence of water and crushed granite at elevated temperatures for periods up to 11 weeks. Sintered bauxite proppant was found to be susceptible to dissolution in hot geothermal water. Quartz sand proppant and resin-coated bauxite proppant appeared to experience less dissolution. Sintered bauxite and resin-coated bauxite proppants were crush tested both before and after exposure to geothermal conditions and the resistance of the proppants to crushing remained unchanged. Based on the testing regime, resin-coated bauxite proppant appears to be well-suited for use in engineered geothermal systems.

TABLE OF CONTENTS

Appendices

ACKNOWLEDGMENTS

The author wishes to acknowledge the contributions of many colleagues whose support and contributions were vital in the completion of this work. The support of the thesis committee – Drs. John McLennan (chair), Joseph Moore, and JoAnn Lighty – is acknowledged. In particular, Drs. John McLennan and Joseph Moore have provided both technical guidance and moral support. The financial support of the US Department of Energy is also acknowledged.

Many colleagues at the Energy and Geoscience Institute and the University of Utah Department of Chemical Engineering and Department of Mechanical Engineering have played vital roles in support of this research. Specifically, the author wishes to thank Kevin Leecaster and Nick Dahdah, of the Energy and Geoscience Institute and Prashanth Mandalaparty of the Department of Chemical Engineering for their contributions to experimental work on proppants; Marylin Segall and Kristie McLin of the Energy and Geoscience Institute for contributions to chemical analyses and mineral identification; Seth Craig of the University of Utah Department of Mechanical Engineering and the Energy and Geoscience Institute for work on the design of equipment; Anthony Rice of the Energy and Geoscience Institute for operational support of tests of proppant crushability; Glenn Johnson and Anthony Gary of the Energy and Geoscience Institute for their invaluable guidance in multivariate statistical analyses; David Langton of the Energy and Geoscience Institute who made samples available; and

Louise Spann and Clay Jones who prepared many samples and performed x-ray diffraction analyses. These colleagues were generous with their talents and time and truly facilitated the present work.

1. INTRODCUTION

1.1 Hydraulic Fracturing

Hydraulic fracturing (*hydrofracing* or just *fracing*) has been performed in oil and gas reservoirs since the late 1940s and is performed to increase fluid flow from a formation to a well. Relative to a rock formation, fractures have extremely high permeability; in fact, fracture permeability is often assumed infinite. Hydraulic fracturing treatments are designed to create or reopen existing fractures in otherwise low permeability rock. In order to maintain fracture permeability after the fracture treatment is complete, fracture treatments of oil and gas reservoirs almost always include the injection of a granular material called *proppant* slurried with the fracture fluid. Proppant is emplaced in fractures to hold them open against the in situ earth stresses, thereby maintaining the permeability of the fracture. The method has been used with extremely positive results in oil and gas wells.

Hydraulic fractures in virgin rock are often assumed to have an idealized bi-wing rectangular, ellipsoid, or penny-shaped geometry. Fractures tend to form in the direction of the maximum total principal stress. In shallow reservoirs, horizontal hydraulic fractures may form; however, at greater depth where overburden stresses are large, hydraulic fractures are more likely to be oriented vertically. These deep fractures extend into the formation in the direction of the greatest horizontal earth stress (i.e., normal to the least horizontal earth stress).

More recently, hydraulic fracturing has been implemented in traditional hydrothermal geothermal reservoirs in attempts to increase the productivity or injectivity of geothermal wells. As outlined by Entingh (2000), those attempts have met with limited success. Since the late 1970s, hydraulic fracturing technologies have been applied to "hot dry rock" reservoirs (i.e., thermal reservoirs lacking sufficient water and/or permeability to make the thermal energy economically recoverable). Fracturing in these hot dry rock (HDR) reservoirs has been implemented in attempts to create so-called engineered geothermal systems (EGS). The EGS concept is based on the creation of a complex fracture network within the thermal reservoir by either creating new fractures or, as is assumed to frequently be the case, reopening existing fractures. Hydraulic fracturing in low porosity, ultralow permeability crystalline thermal reservoirs has been performed in several locations including Fenton Hill, New Mexico, USA; Soultz-sous-Forêts, France; and Rosemanowes, United Kingdom. Fenton Hill and Soultz-sous-Forêts will be discussed presently.

1.**1.1 Hydraulic Fracturing in Geothermal Applications –**

Case Studies

Though examples are fewer, hydraulic fracturing methods have been using in geothermal reservoirs, both in porous rocks and in low-porosity crystalline rocks. The engineered geothermal system model calls for large underground "heat exchangers" to be "manufactured" by creating or enhancing large fracture networks which penetrate hot rock resources. Two examples of the successful creation of working, albeit small, EGS are discussed.

1.1.1.1 Fenton Hill, New Mexico, USA

Fenton Hill, New Mexico was the site of the first ever attempt at creating an engineered geothermal system in crystalline rock using hydraulic fracturing technology. Work at Fenton Hill was conducted by Los Alamos National Laboratory (formerly Los Alamos Scientific Laboratory).

The first phase of work at Fenton Hill began in 1974 with the drilling of the first deep well (Duchane and Brown, 2002). A hydraulic fracture was created and a second well was drilled to intersect the fractured zone. Only low flow rates connecting the two wells were obtained. After several more fracture jobs, a better hydraulic connection was created but flow tests showed that the temperature was being drawn down rapidly (Duchane and Brown, 2002). Additional fracture jobs were done resulting in two vertical hydraulic fractures coincident with the two wells, and a series of natural subhorizontal joints connecting the two main vertical fractures. Flow tests showed a much slower rate of temperature drawdown (Duchane and Brown, 2002).

The second phase of work at Fenton Hill commenced in 1979. Two deep wells were drilled and multiple hydraulic fracturing treatments were conducted. However, these jobs failed to connect the two wells. The lower portion of one of the wells was closed in and a new leg of the well was drilled to intersect the fracture zone indicated by microseismic data (Duchane and Brown, 2002). The lower portion of the second well, which had been damaged during fracturing, was also closed in and the well re-drilled. Tests of the fractured region indicated that the liquid-swept region encompassed between $6 \cdot 10^6$ and $8 \cdot 10^6$ m^3 (Duchane and Brown, 2002).

Surface equipment was installed and flow tests were conducted. The tests were plagued by equipment difficulties at the surface, including the failure of two circulation pumps; these equipment difficulties slowed progress and limited results. Long-term flow testing consisted of three steady-state flow periods ranging from 55 to 112 days (Duchane and Brown, 2002). While relatively short in duration, those tests were characterized by stable produced fluid temperature. Thermal power production was 4 to 6 MW, which would have amounted to approximately 0.5 MW electric power production (Duchane and Brown, 2002).

1.1.1.2 Soultz-sous-Forêts, France

Development of an engineered geothermal system in Soultz-sous-Forêts began in 1987 with funding provided by France, Germany and the European Commission. Since that time, organizations and scientific parties from various other European countries have been involved in development of the site (Baria et al., 1999). Early stages of the development of the proposed EGS project included the drilling of two deep boreholes that both penetrated the crystalline basement. Hydraulic fracturing in the two wells was conducted. Fracturing resulted in pressure response between the two wells that was evident during injection. Seismic events indicated a connection between the two wells (Baria et al., 1999). Testing indicated that the reservoir was highly jointed and that flow was closely related to the presence of those joints (Baria et al., 1999).

Later work at Soultz-sous-Forêts included drilling two additional deep holes. The two new wells were drilled from the platform of one of the existing wells and were deviated from that central location (Genter et al., 2009). The three wells are arranged in a *triplet* consisting of an injection well with production wells on either side. The three

wells are approximately collinear at depth and are aligned in the direction of maximum horizontal stress (Genter et al., 2009). The wells were hydraulically fractured leading to significant and permanent increases in injectivity (Genter et al., 2009). A binary organic Rankine cycle power plant was built. Submersible pumps were installed to improve flow rates above artesian flow rates. The first power was produced in June, 2008 (Genter et al., 2009).

1.2 Thermal Fracturing

Temperature changes and associated changes in in situ stresses due to thermal contraction in a hot reservoir may lead to the formation of thermal fractures. Perkins and Gonzalez (1985) discuss the effects of reservoir cooling on in situ stresses is permeable reservoirs. As cool (i.e., below reservoir temperature) fluid is injected, a cooled region grows out from the wellbore. The cooled region is initially circular in the plan view but as hydraulic fractures extend into the reservoir in the direction of greatest horizontal earth stress, the cooled region becomes elliptical. Eventually, when the cooled region is sufficiently elongated, in situ stresses within the cooled region may change their orientation due to thermal contraction. The result of this change in stress orientation may be, according to Perkins and Gonzalez (1985), the creation of thermal fractures extending from the main fracture face in a direction normal to the main fracture face.

In a low porosity hot crystalline reservoir, heat will move through the reservoir primarily by conduction. The size and rate of growth of the cooled region of the reservoir will be governed by thermal and physical properties such as thermal conductivity, specific heat capacity and density. These properties, as well as fracture

geometry and temperatures of the reservoir and the fluid must be understood to predict the development of the cooled region and associated thermal fractures that may form.

Tester et al. (1989) interpreted data from Fenton Hill and outlined evidence for possible reservoir growth due to thermal fracturing. Another possible conclusion is that fracture aperture increased rather than that new fractures formed. However, if the size (i.e., effective contact surface area) of the Fenton Hill reservoir did increase as a result of thermal fracturing, the life of the well may have been extended as new volumes of reservoir came into contact with circulating fluids.

Hydraulic fracturing of geothermal reservoirs presents new challenges which much be addressed. For example, thermophysical properties of the reservoir rocks must be understood in order to predict the growth of the cooled region and associated thermal fracturing which is expected to take place. Additionally, if proppant is to be used in geothermal systems, the resilience of the proppant to geothermal conditions must be understood. Proppant degradation could lead to decreases in hydraulic conductivity, fluid flow rates and power production. The present work is subdivided into two parts, the first of which suggests a method for predicting rock thermal conductivity based on geophysical well logs. The second part discusses laboratory tests of proppant exposed to simulated geothermal conditions.

1.3 Literature Review

1.3.1 Well Log Data Analysis for Determination of Physical Properties

The development of wireline well logging technology began as early as the 1920s when the Schlumberger brothers produced the first resistivity logs (Hearst and Nelson,

1985). Since that time, new well logs have been developed and the technology has improved to increase precision and accuracy. Today, modern well log "suites" include gamma ray logs, which measure natural and induced radioactivity; caliper logs, which measure borehole size and help identify washout zones and areas of increased faulting; induction logs, which measure electrical resistivity and can be used to identify hydrocarbons present in pore spaces; spontaneous potential logs, which measure electrochemical potential; density logs, which measure density as a function of Compton scattering of gamma rays; neutron logs, which measure attenuation of neutrons due to interaction with hydrogen; and acoustic logs, which measure the velocity of acoustic waves; and many others (Hilchie, 1982). Various correlations and mixing rules have been developed, which allow quantitative, not just qualitative, analysis to be performed based on well log data (Hearst and Nelson, 1982). For example, porosity can be calculated based on density logs or neutron logs. Modern spectral gamma ray logs even allow rock mineralogy to be calculated as long as a few assumptions can be justified (Williams and Anderson, 1990).

The oil and gas drilling and production industry has long used well logging to great benefit. Using well logs, analysts have identified zones of high and low porosity and zones rich in hydrocarbons. However, in addition to those traditional methods and applications, methods of statistical analysis of well log data have also been developed which allow well log data to be correlated with rock properties for which no mixing rules are known (Hearst and Nelson, 1982). Such statistical techniques include multivariate methods such as principal components analysis, multiple regression and cluster analysis.

Alternatively, log-obtained data may be used in calculations of other properties not measured directly by logging tools themselves.

Multivariate cluster analysis has been applied to well log data sets by various researchers. Cluster analysis methods commonly also incorporate principal components analysis. Discussions of principal components and cluster analyses are included in Appendix A.

As part of the Ocean Drilling Program, Gonçalves (1998) published his findings on a non-hierarchical clustering algorithm applied to a large well log data set from four holes drilled in the Côte d'Ivoire-Ghana Transform Margin. The holes were extensively logged; the available log data included neutron porosity, deep resistivity, medium resistivity, shallow resistivity, density, photoelectric cross section, gamma ray, spectral gamma ray and acoustic compressional wave velocity, although not all log curves were available for all four holes. A correlation matrix was calculated and principal components analysis was applied.

Nonhierarchical cluster analysis methods were applied both using well log data standardized to have zero mean and standard deviation of one and using principal component scores. Gonçalves notes that statistically speaking, the method in which principal component scores were used should perform better because principal components are normal to one another by definition. In the end, cluster analysis of original log data and principal component score data yielded similar results with the results of the method using principal components being somewhat more detailed. The results of both methods were found to be in good agreement with the stratigraphy defined by analysis of drill core.

Tavakoli and Amini (2006) performed a similar cluster analysis method on a well in the Marun Field in southern Iran. The well was logged and cored over its entire depth, allowing correlation of cluster analysis results with actual core samples. The aim of the study was to extrapolate information obtained from the cluster analysis of the fully-cored well to nearby wells which were not cored. Four logs – gamma ray, computed gamma ray (sum of potassium-40 and thorium), sonic and density logs – were analyzed using a hierarchical cluster analysis algorithm. The algorithm yielded 12 *logfacies* which were correlated with lithostratigraphic descriptions published in earlier studies. Tavakoli and Amini note the importance of validating the cluster analysis model by comparison to core and cuttings data.

Crampin (2008) performed a cluster analysis study on 14 offshore exploration wells and 123 percussion sidewall samples. Well logs were conditioned by removing effects of anything other than rock composition and texture. For example, an effective vertical stress model, developed previously, was used to remove burial depth effects from acoustic log data. The sidewall samples were categorized into six *petrofacies*. Cross-plots of the data from the sidewall samples were created. Only the logs which best differentiated between petrofacies, as shown in the cross-plots, were selected for inclusion in the cluster analysis.

The cluster analysis itself was performed using GEOLOG, a commercially available software package by Paradigm, Ltd. The cluster analysis identified five *electrofacies*, defined as zones with similar electric well log responses. One of the petrofacies was not matched with an electrofacies due to inconsistent log response. However, the other five petrofacies correlated well with the cluster analysis results.

Crampin notes that the results of cluster analyses are highly sensitive to the logs selected for input.

Other investigators have suggested that log data can be correlated with other physical properties. Chang, Zoback and Khaksar (2006) present a review of 31 correlations for determining rock unconfined compressive strength as a function of log-obtained data such as porosity and compressional wave slowness. They conclude that most of the correlations they reviewed, while valid for the data set from which each was originally derived, fail to predict compressive strength of rocks from a broad data set. Their conclusion is probably true of attempts at correlating other rock properties, as well, because these types of empirical correlations are largely limited by the scope of available data and almost certainly do not contemplate all possible variables that could have an effect on the property being predicted.

Brocher (2005) summarized the work of other investigators and published his work on correlations between compressional and shear wave acoustic velocities, rock density and Poisson's ratio. Brocher's data set was large and broad in scope (although a large portion of the data came from California) and included in situ data from well logs, vertical seismic profiles and laboratory data collected from hand samples. The data represented sedimentary as well as metamorphic and igneous crystalline rocks. A linear polynomial regression on a subset of the data (calcium-rich and mafic rock data were excluded, as were data from serpentinites and gabbros) of shear wave velocity over compressional wave velocity yielded "Brocher's regression fit" which matched the data well ($R^2 = 0.979$). Brocher's "mafic line" more accurately describes the relationship

between shear and compressional wave velocities in rocks such as basalts, anorthosites, marbles and dolomites.

Williams and Anderson (1990) used well log data directly in calculating thermal conductivity of low-porosity crystalline rocks. Their model is based on the theory of phonon conduction. Williams and Anderson review other methods of determining thermal conductivity, such as empirical correlations and calculations based on known conductivities of constituent minerals. They then outline their method for estimating thermal conductivity based on phonon conduction theory. A proportionality relates thermal conductivity to mean interatomic distance, isentropic bulk modulus, mean phonon velocity, shear modulus and temperature. The proportionality is given quantitative functionality through regression analysis performed on laboratory samples for which the necessary properties are known.

All the values necessary for the application of the model of Williams and Anderson can be obtained from modern well log suites. Mean interatomic distance is a function of density and mean atomic mass, which itself can be calculated from photoelectric cross section. Both density and photoelectric cross section can be obtained from well logs. Mean phonon velocity is a function of shear and compressional acoustic wave velocities. Bulk modulus is a function of acoustic velocities and density. Shear modulus is a function of density and shear velocity. Compressional and shear velocities can also be obtained from well logs.

Williams and Anderson note that their model is highly sensitive to both compressional and shear wave velocities, and the ratio of those velocities. As a result, accurate sonic wave velocities are important and any factors which might negatively

affect the quality of acoustic data would have an even more pronounced negative effect on calculated thermal conductivity. Fracturing, including microfracturing, can have a significant negative effect because open fractures tend to attenuate acoustic waves. However, Williams and Anderson also point out that fractures intersecting the borehole can be expected to be closed at sufficient depth due to in situ stress. A correction to shear and compressional wave velocities based on depth of burial was applied. The resultant calculated thermal conductivity matched thermal conductivity measured on drill core to within ±15%. However, the model breaks down in areas of large-scale fracturing where open fractures remain.

The thermal conductivity predicted by the model of Williams and Anderson is the vertical thermal conductivity. As discussed, the model is a strong function of compressional and shear acoustic wave velocities. When those velocities are measured in situ by an acoustic well logging tool, the waves travel from the acoustic emitter vertically up the wellbore wall to the receiver. The velocities are measured vertically and therefore the calculated thermal conductivity is the vertical thermal conductivity. The divergence of vertical and horizontal thermal conductivity would be greatest in anisotropic formations.

While the model proposed by Williams and Anderson is a function of mean interatomic distance, in reality, that distance varies only very slightly among rock types. Therefore, if the mean interatomic distance is assumed to be constant and if density and sonic wave velocities can be obtained from gravity and seismic surveys, then the model can be applied in the absence of any well log data.

Pribnow and Sass (1995) used Williams and Anderson's method to predict thermal conductivity in the Kontinentales Tiefbohrprogramm der Bundesrepublik Deutschland (KTB) in Germany. They found significant discrepancies between thermal conductivities calculated by the model and those measured on core samples. The discrepancies are attributed to the presence of microcracks, cleavage plains (specifically, in the case of micas) and anisotropy. However, the model was verified in crystalline rocks in isotropic zones or regions of transverse isotropy.

1.3.2 Proppant Stability and Strength

The second part of the present work discusses proppant compatibility with simulated geothermal conditions. Proppant testing to evaluate performance at expected geothermal conditions has been conducted by various groups since the late 1970s. Very early work on proppants for use in geothermal systems was conducted by Maurer Engineering, Inc (1980, 1981) in support of the Geothermal Reservoir Well Stimulation Program (GRWSP). Between July 1980 and January 1981, a report in four volumes was published detailing experiments conducted in support of the development of geothermal fracture stimulation technologies. Central to their work was significant testing of various proppants under simulated geothermal conditions (temperature, fluid chemistry and confining stress). Tests were conducted on four different sand proppants: glass beads, sintered bauxite, resin-coated sand and resin-coated bauxite.

Proppant was tested under varying confining stress and varying temperature (Maurer Engineering Inc., 1980). Permeability was found to decrease with increasing closure stress. Permeability also decreased with increasing temperature for several proppant types tested. Under the test conditions, resin-coated proppant was found to

maintain permeability best and to be less sensitive to temperature variation than some sands. Sintered bauxite appeared to be unaffected by temperature increase. These early tests were short-term and further "long-term" testing was begun.

The early short-term experiments pointed to temperature and chemical effects but long-term tests were required to quantify the effects. Long-term tests lasting 50 hours were conducted on proppant under the same simulated geothermal conditions (Maurer Engineering, Inc., 1981). These tests were conducted at temperatures up to 500 °F and closure stresses up to 10,000 psi. Results of the experiments showed that sintered bauxite and resin-coated proppant maintained permeability well for the duration of the experiments. Tests on sand proppant were characterized by permeability which dropped throughout the duration of the experiments and the generation of significant amounts of fines. The conclusion reached was that the rate of chemical attack was strongly related to surface area. Weaker proppants were thought to also be more susceptible to chemical attack due to increased surface area associated with breakage from the initial loading. Thus, proppant degradation was tied to closure stress and chemical attack.

Sintered bauxite and resin-coated proppants performed much better in these long-term tests. Sintered bauxite was found to be more deformable than sand used as proppant, allowing for much larger proppant grain contact areas, thus reducing stress concentrations. Additionally, when sintered bauxite proppant grains did break, the fragments tended to be relatively large. Resin coating was also found to increase proppant grain deformability and add additional value by holding proppant grains together even after they had broken.

Sinclair (1980) provided a summary of available data on the compatibility of proppant with geothermal conditions. Resin-coated sand, resin-coated bauxite and sintered bauxite were found to be unaffected by elevated temperatures. Resin-coated bauxite was identified as the strongest proppant tested and was characterized by temperature and load insensitivity. Resin-coated sand was found to have slightly lower permeability but was also characterized as insensitive to temperature and load up to 10,000 psi. Sintered bauxite was somewhat more susceptible to crushing but was considered inert in simulated hot geothermal brine. The same findings are reported by Campbell et al. (1981) in a report of progress made by the GRWSP.

Knox and Weaver (1989) caution that dissolution of bauxite is a possibility because formation fluids are probably not in equilibrium with bauxite. In flow tests conducted by Knox and Weaver using a pH-modified fluid (pH = 11), significant loss of proppant mass was identified. Sand proppants lost up to 77% of initial mass while other "popular, high performance proppants" lost between 37 and 60% of their initial mass over the course of these 3-day tests. Results also indicated the development of amorphous precipitates and crystal growth.

In later work presented by Weaver et al. (2006), diagenesis or pressure-solution-type reactions are proposed as other sources of observed permeability decline, particularly in high temperature and high closure stress environments. They also point out that the use of high strength proppants composed of non-native materials may have a negative impact on permeability and specifically point out the risk of clay formation. Surface modification additives (SMA) were investigated as a potential method of reducing permeability decline due to these chemical effects. SMAs were found to be

effective at preventing water from reaching proppant-proppant and proppant-rock contact areas, thus preventing chemical reactions and better maintaining fracture permeability.

Freeman et al. (2009) found that proppant crushability increased when proppant was tested in the presence of a hot saturating fluid. Three bauxite proppants were tested according to the ISO standard test and percent of crush was calculated. In modified tests, the same three proppants were then tested at 500 °F and 20,000 psi closure stress and only small increases in the crush fraction were noted. However, when saturating fluid was added, the crush fractions increased and the three proppants, which had performed comparably to that point, diverged significantly with crush fractions, defined as the ratio of mass of fine particles to total proppant mass, ranging from 9.7 to 25.1% fines.

1.4 Raft River, Idaho

The Raft River valley is located in extreme southern Idaho, just north of the Utah border. The valley is bounded on the west by the Jim Sage and Cotterel mountain ranges, on the east by the Black Pine and Sublette mountains, and on the south by the Raft River range. The valley opens onto the Snake River plain to the north.

Nine geothermal wells have been drilled in the valley to depths of up to 6500 ft and have intersected three distinct geologic formations. The Precambrian basement is comprised of quartz monzonite which is overlain by a series of four metasedimentary units: The Older Schist, the Elba Quartzite, the Upper Narrows Schist and the Quartzite of Yost (Blackett and Kolesar, 1983). Rock units from the Precambrian basement have been correlated with rocks in the Raft River Range (Covington, 1980). Above these basement rocks lies a thick (up to 5250 ft) series of highly fractured tuffs, sandstones and siltstones known as the Salt Lake Formation. The Salt Lake Formation is overlain by the

Raft River Formation, comprised of sand, silt and gravel; the boundary between the Salt Lake and Raft River Formations is gradational (Blackett and Kolesar, 1983).

Two major north-south trending fault zones—the Bridge Fault and the Horse Well Fault—have been identified on the east side of the valley in the Tertiary sediments (Blackett and Kolesar, 1983). These fault zones are responsible for the upward transport of the geothermal water from greater depths. In addition to the Bridge and Horse Well faults, there is some evidence, including seismic surveys and lateral displacement of volcanic rocks at the surface (Blackett and Kolesar, 1983), for a shear fault in the Precambrian basement known as the Narrows structure.

Meteoric recharge of the hydrothermal system likely occurs in the Raft River and Albion mountains where rocks have been correlated with the Precambrian basement. Water is circulated at depth in the fractured basement, flows along the Narrows structure and then flows up the Bridge and Horse Well faults to the surface (Covington, 1980). The majority of the hydrothermal activity in the valley coincides with the proposed intersection of the Bridge and Horse Well fault zones with the Narrows structure.

A thermal and hydraulic fracture campaign is planned for well RRG-9. The well lies at the southwest corner of the Raft River geothermal field and while it is in line with the proposed location of the Narrows structure, it does not penetrate any deep permeable zones. Well RRG-9 was drilled into Precambrian crystalline rocks, reaching metamorphosed sediments at 4795 ft true vertical depth (TVD).

Initially, cool water (cooling tower blow-down water at approximately 140 °F) will be injected into the well. Next, cold water will be injected. Injection pressures will be kept below fracture pressures unless injectivity is too low, in which case pressures will

be increased. Temperature changes due to fluid injection will lead to the formation of a cooled region, and, potentially, creation of thermal fractures. Properties of the rock reservoir including thermal conductivity must be understood in order to predict the effects of cool fluid injection on the reservoir. Initial plans called for thermal and hydraulic fractures to be propped, though plans have changed due to budgetary factors. Many engineers contend that propping of fractures in geothermal systems is unnecessary and suggest that these fractures will be "self-propped" by fracture face asperities. Still, if proppants are to be used, the effects of geothermal conditions (geothermal brine at elevated temperatures) on those proppants must also be understood since the use of an incompatible proppant may lead to reduction of fracture permeability.

2. MULTIVARIATE STATISTICAL ANALYSES FOR DETERMINATION OF THERMAL CONDUCTIVITY USING WELL LOG DATA

2.1 Introduction

The literature regarding the thermal conductivity of rocks is relatively plentiful, however, most investigators have published on the thermal conductivity of sedimentary units. This comes as little surprise since, until recently, the primary patron of reservoir engineering and geophysics research was the oil and gas industry. As the interest in geothermal energy, especially engineered geothermal systems (EGS), has increased, the crystalline basement has become an active area of investigation, although available data are much less prevalent than data from sedimentary reservoirs.

Well log data are ubiquitous from both hydrocarbon and geothermal systems. However, while well log data are plentiful and relatively easily obtainable, current logging tools and analyses focus on the factors of greatest importance in oil wells: porosity and permeability. In an EGS candidate well, matrix porosity and permeability are generally considered to be essentially zero, and, accordingly, water cannot flow through the hot rock. In fact, the success or failure of the EGS concept hinges on successfully and consistently creating networks of fractures in such a way that significant amounts of water, the heat transfer fluid, can come in contact with a sufficiently large

rock surface area to extract enough thermal energy to make an EGS reservoir and power plant economically viable.

Rocks are hydraulically fractured to create fluid flow pathways in the reservoir rock. Hydraulic fracturing has been practiced with great benefit in the oil and gas industry for more than 60 years. Experience with hydraulic fracturing of geothermal reservoirs is much more limited, though fracture treatments have been performed in traditional hydrothermal systems with limited success (Entingh, 2000). While application of fracturing technologies in nominally impermeable rock has been even more limited – for examples, see Genter et al. (2009) and Duchane and Brown (2002) – hydraulically fractured EGS remain an area of significant interest and active research. Rock fracturing is largely controlled by the magnitude and orientation of in situ stresses and rock strength and deformation properties. In addition to hydraulic fracturing, thermal fracturing is expected to occur in geothermal systems in which significant temperature differences can be applied. Therefore, in addition to the mechanical properties of rock which govern fracture propagation, thermophysical rock properties such as thermal conductivity and heat capacity, which govern heat flow and temperature gradients, are also important.

2.2 Theory

Many different models for estimating thermal conductivity have been proposed, including regression of thermal conductivity over well log data (e.g., acoustic velocity, gamma and density response); estimating thermal conductivity as the geometric mean of the conductivity of the oxide constituents of a rock, with compositional data obtained from X-ray diffraction (XRD) analyses; and methods based on spectral gamma logs (Williams and Anderson, 1990). Williams and Anderson caution that such methods may

be lithologically or geographically limited and make no attempt to incorporate the physics of conduction in solids. Williams and Anderson (1990) present a new, semi-empirical model for predicting thermal conductivity based on theory of conduction on crystalline solids. Their model was selected for application to the Raft River geothermal wells because it was derived from conduction theory (as opposed to only empirical relationships), was specifically developed for application to low porosity rocks and gives thermal conductivity as a function of data obtained from well logs.

2.3 Method

2.3.1 Model of Williams and Anderson

Williams and Anderson's model is semi-empirical and was developed using phonon conduction theory. From phonon conduction theory, Williams and Anderson obtained a proportionality for conductivity. They then performed laboratory measurements of thermal conductivity on various bulk minerals for which all necessary physical properties were already known. A regression analysis was then performed to fit the measured thermal conductivity of their samples to the phonon conduction theory proportionality. Their model of conduction in nonmetallic crystalline solids then became

$$k_{phonon} = 0.7531 + 0.1005\left(\frac{aV_m\mu^2}{3K_sT}\right); \quad R = 0.97 \tag{2.1}$$

where a is the mean interatomic distance, K_s is the isentropic bulk modulus, μ is the shear modulus, V_m is the mean phonon velocity and the constants represent the regression parameters. Temperature, T, in the model is the temperature at which laboratory measurements were taken, in this case, 298 K.

In order to apply the model, a significant amount of information about the rocks of interest must be known. As written, the model is a function of the mean interatomic distance, shear and bulk moduli, and mean phonon velocity. Shear modulus can be calculated from bulk density and shear wave velocity. Bulk modulus can be calculated from bulk density and shear and compressional wave velocities. Mean interatomic distance can be calculated from density and mean atomic mass, which itself can be determined based on photoelectric cross section. In order to calculate the thermal conductivity of a crystalline solid, then, only four parameters must be known: bulk density, shear and compressional wave velocities, and photoelectric cross section. All of these parameters can be obtained from modern well logs. Additionally, Williams and Anderson point out that mean interatomic distance varies only slightly and, optionally, a constant average value may be used. The model can be used to determine the thermal conductivity of low-porosity rocks based exclusively on well log data. The model of Williams and Anderson was applied to Raft River, Idaho well RRG-3. A similar method will be used and validated when well RRG-9 is logged in preparation for the planned thermal and hydraulic fracturing campaign in that well.

The bottom ~1500-foot interval of well RRG-3 was selected for investigation. Complete modern well log suites commonly include all the log data necessary to apply the model of Williams and Anderson. However, logging of early wells at the Raft River geothermal site was conducted in the mid to late 1970s and the available logging suites are incomplete by today's standards. Density and compressional wave velocity data were available but photoelectric and shear wave velocity data were not. In order to apply Williams and Anderson's model, proxies for the shear wave velocity and photoelectric

data had to be identified. Alternatively, a constant average mean interatomic distance could have been assumed making photoelectric data unnecessary.

2.3.2 Brocher's Regression Equation

Brocher (2005) presented an empirical relationship between shear and compressional wave velocities. Brocher performed a polynomial linear regression on a large dataset which included velocity data from sedimentary and granitic rocks. "Brocher's regression equation" (eq 2.2) is a polynomial curve fit ($R^2 = 0.979$) and gives shear wave velocity[1] (V_S) as a function of compressional wave velocity (V_P), both of which have units of kilometers per second.

$$V_S = 0.7858 - 1.2344V_P + 0.7949V_P^2 - 0.1238V_P^3 + 0.0064V_P^4 \qquad (2.2)$$

Brocher's regression equation was used to create a "shear wave velocity pseudo log." Data from the shear wave slowness pseudo log were then used in the application of the Williams and Anderson model.

2.3.3 Well Log Data Analysis

Lacking a photoelectric log, a "photoelectric pseudo log" had to be derived to avoid assuming constant mean interatomic distance in the model of Williams and Anderson. Well RRG-3 was completed with three directionally-drilled legs (sidetracks); data from well RRG-3 leg A (RRG-3A) included five log tracks: neutron porosity, natural gamma ray, formation density, density porosity, and compressional wave slowness logs. Formation density and formation porosity logs are actually generated together with

[1] The quantity typically recorded on an acoustic well log is acoustic wave slowness or travel time measured in units of micro-seconds per foot. Acoustic wave velocity is simply the inverse of acoustic wave slowness.

formation density being a linear transformation of formation porosity. An additional combination log was defined as the difference between the density porosity and neutron porosity logs and will be referenced herein as the "porosity difference log."

The five analog well logs were digitized by hand in a process that was inherently subjective; however, care was taken to maintain the shape of each log curve. Special attention was paid to local maxima and minima and to inflection points. The process yielded data that were obviously not uniformly distributed over the depth of each log curve. The log data formed the dataset for multivariate data analysis.

In order to bring the data together so that all the individual log curves could be considered together, the data were parameterized by depth. A Microsoft Excel macro was written to evenly discretize ("condition") the digitized well logs. Given a desired sampling rate (i.e., points per foot), the macro averaged data in intervals in which the sampling rate was too great and linearly interpolated in intervals in which the sampling rate was too small. The macro transformed the unevenly distributed data into evenly distributed, conditioned data of uniform, specified sample rate. Naturally, a higher sampling rate more accurately represented the raw log data. For the work conducted in the present study, a sampling rate of 2 points/ft was selected. Each of the five raw well log curves was conditioned in this manner. Figure 2.1 shows examples of the results of data conditioning.

The evenly distributed conditioned log data sets were then combined into one five-dimensional data set where each log accounts for one dimension. Just as an arbitrary point in three-dimensional space can be defined by its location along the x, y and z axes, so a point in n-dimensional space can be defined by its location along n different axes.

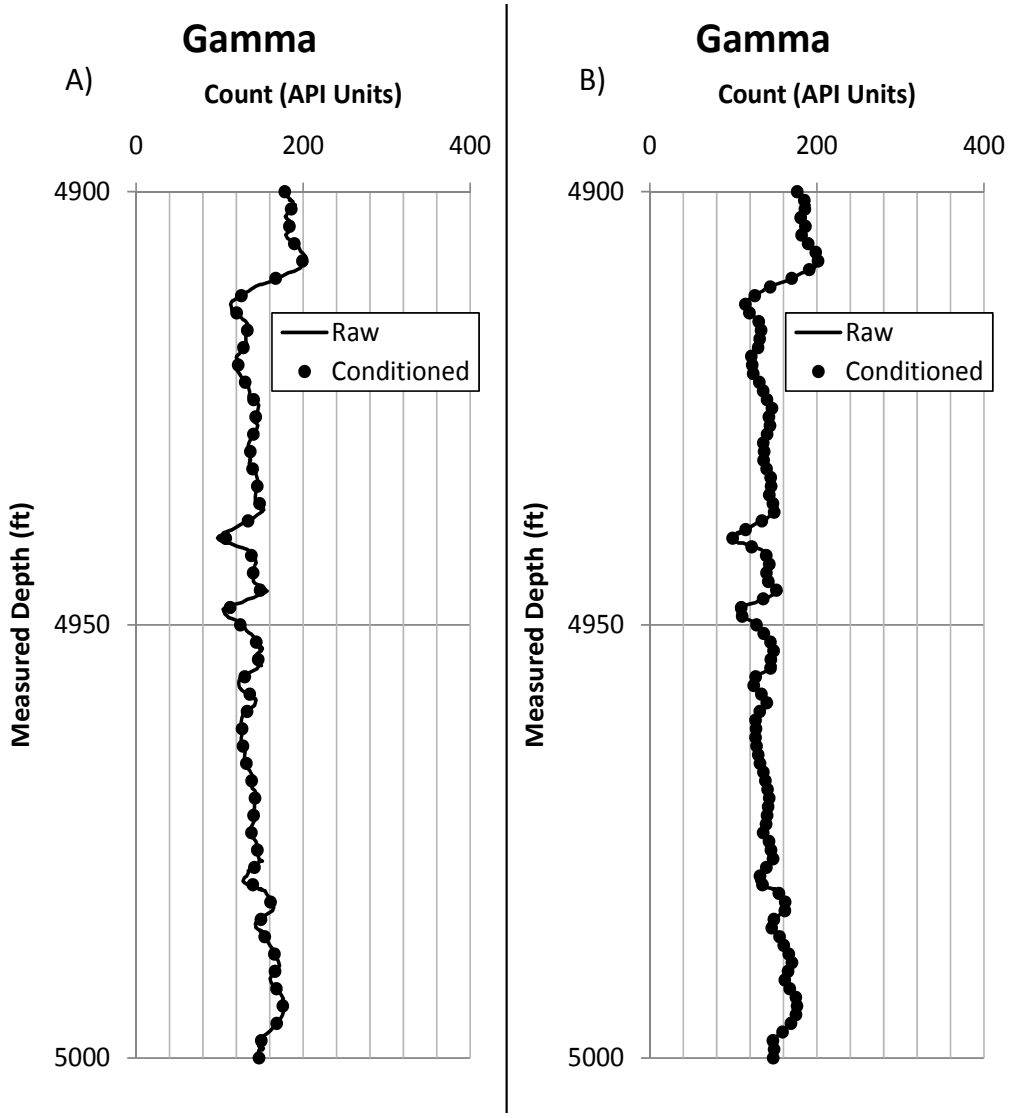

Figure 2.1. Results of data conditioning on a sample of log data. Conditioned data are shown superimposed on the raw log data. Conditioning is accomplished by averaging data in intervals in which sampling rate is greater than the specified rate and by linear interpolation in intervals in which sampling rate is less than the specified rate. A) Conditioned with a specified sampling rate of 0.5 points/ft. B) Conditioned with a specified sampling rate of 1.0 points/ft.

The five-dimensional data set described above, then, consists of a list of data points (*observations*) corresponding to depth. Each of those observations is defined by its location along the five log "axes" or variables: neutron porosity, natural gamma ray, formation density, compressional wave slowness and porosity difference. Synonymously, each observation is defined by a vector of the form $[X_1,\ldots X_i,\ldots X_5]$ where the individual X_i are the values of the five log variables.

The next step in the analysis of multivariate data was standardization of the data. Data standardization is important especially when dealing with data in variables of differing magnitude. The data under consideration differed widely from variable to variable. For example, the values of the density variable ranged from two to three grams per cubic centimeter; values of the compressional wave slowness variable ranged from 40 to 140 μsec/ft. Data standardization ensured that no one variable played an unduly large role in the data analyses which followed. Standardization was performed on each variable individually. The typical standardization method is called a Z transform and involves subtracting the mean and then dividing by the standard deviation; the Z transform was applied to the conditioned well log data. The resultant data set contained variables which all had zero mean and standard deviation of one. Data standardization allowed data of differing units and magnitudes to be compared equally.

A principal components analysis (PCA) was then performed on the standardized well log data. Principal components analysis is a multivariate data analysis method which can be used to reduce the dimensionality of a data set and gain greater understanding of the structure of a data set. A discussion of the theory and application of PCA can be found in Appendix A. The literature contains accounts of using PCA in

conjunction with other multivariate data analysis techniques. Moline and Bahr (1995), Lim, Kang and Kim (1997) and Gonçalves (1998) all used principal components analysis to reduce data dimensionality in preparation for segmentation or clustering. Dunteman (1989) discusses PCA prior to regression analysis. In the present study, photoelectric cross sections obtained from mineralogic analysis (described below) were regressed over well log and principal components data in an attempt to define a photoelectric pseudo log as a function of other known log variables.

2.3.4 Photoelectric Cross Section

The mineralogic compositions of 19 drill cuttings samples from well RRG-3A were determined using X-ray diffraction spectroscopy. These mineralogic compositions were then used in computing the photoelectric cross sections of the cuttings. Photoelectric cross section is a statistical measure of the likelihood that photons of a given energy will excite an electron resulting in the ejection of that electron; photoelectric cross section has units of barns per electron. Photoelectric cross sections (P_e) were calculated as the sum of the photoelectric cross sections of the constituent elements weighted by the mass fractions of those elements in the samples (Ellis, 2003). Bulk rock elemental compositions were calculated based on mineralogic compositions obtained using XRD and on the molecular formulas of those minerals. Molecular formulas of some few minerals were not available in the literature. In those cases, the minerals were modeled as other similar minerals and the cross sections calculated as described previously. The mineral photoelectric cross section and details of how the cross sections were calculated are shown in Table 2.1.

Table 2.1. Photoelectric cross sections of minerals identified in drill cuttings.

Mineral	P_e (barns/electron)	Notes
Calcite	5.08	1
Chlorite	3.33	1,3
Chlorite/Smectite	5.26	2,4
Illite	2.40	1,5
K-feldspar	2.86	1,6
Muscovite	2.40	1
Plagioclase	1.76	2,7,
Pyrite	16.97	1
Quartz	1.81	2
Zeolite	1.53	1,8

1) Composition from Handbook of Mineralogy
2) Composition from Mineral Database
3) as Clinochlore
4) as Corrensite
5) as Muscovite
6) as Orthoclase
7) as Albite
8) as Analcime

2.3.5 Regression Analysis

Regression analysis was performed on the results of the principal components analysis and on raw well log data to evaluate relationships between log-obtained data and photoelectric cross sections calculated based on mineralogy. The objective of the regression analysis was to identify relationships between photoelectric cross section and log data so that, in the absence of an actual photoelectric log, photoelectric cross section could be calculated from other log data. The calculated photoelectric cross section could then be used in Williams and Anderson's model.

2.4 Results and Discussion

Principal components analysis was performed on the standardized data set. The results of the PCA are included in Table 2.2. The top row of the table indentifies the five principal components, identified as PC1 through PC5. The left-most column identifies each of the five variables in the analysis. The top portion of the table gives the "loadings" of each variable on each principal component. The loadings of all of the variables on a principal component define the principal component vectors in variable space. For example, the loading of formation density on principal component one is 0.569. The bottom portion of the table gives the amount of variance for which each principal component accounts. As is typical, principal components are listed in the order of greatest to least amount of variance for which they account (PC1 accounts for 59.0% of the total variance, PC2 accounts for 24.7%, etc.).

Original log data were rotated into the principal component space by projecting the well log data onto the principal component axes. The projection of a data point onto a particular principal component is known as the "score" of the data point on that principal component. The principal component scores of the data on each of the principal components were calculated as the dot products of the well log variable vectors and each of the principal component loading vectors. The rotation of the data from the original variable space into the principal component space is a lossless process meaning the operation can be performed in reverse and the original data can be obtained again.

There are various methods for identifying which of the principal components contribute significantly to the total data variance. In one such method, the variances of each of the principal components are shown on a scree chart (see Figure 2.2). The chart

Table 2.2. Results of principal components analysis. The top portion of the table shows the "loadings" of the five variables on each of the principal components. The bottom portion of the table shows the amount of variance for which each principal component accounts.

	PC1	PC2	PC3	PC4	PC5
Neutron Porosity	-0.492	0.352	-0.349	-0.547	0.461
Gamma Ray	-0.035	0.792	0.587	0.167	0
Formation Density	0.569	0.095	-0.177	0.289	0.744
Compressional Wave Slowness	-0.519	0.093	-0.373	0.764	0
Porosity Difference	0.404	0.481	-0.603	-0.078	-0.484
Variance	2.949	1.234	0.633	0.184	0
Percent of Total Variance	59.0	24.7	12.7	3.7	0
Cumulative % of Variance	59.0	83.7	96.3	100.0	100.0

gets its name from the general shape of the data which some have said looks like the scree pile at the base of a cliff. Sometimes, a scree chart can aid the analyst in deciding how many principal components should be retained based on the relative amount of variance attributed to each principal component. However, in the present case, there is no obvious distinction between those components that account for significant amounts of variance and those that do not. It is therefore difficult to decide how many principal components should be retained based on this graphical method.

Other methods for determining the minimum number of principal components have been proposed. Most of those methods are based on the amount of variance accounted for by the individual principal components. However, Miesch (1976) proposes that the decision as to how many principal components to retain should be made based on how well the selected principal components represent the original data. To aid in making this decision, Miesch defines a coefficient of determination, CD, which can be used to quantify how well the variable data are reproduced by the selected principal components.

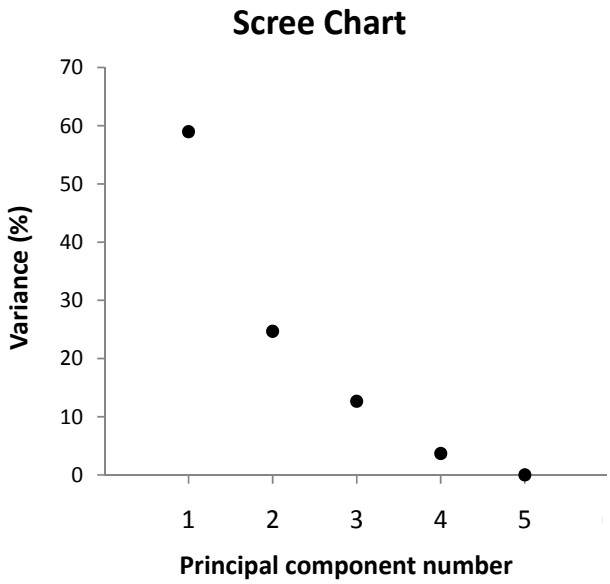

Figure 2.2. Scree chart of principal component variance. The scree chart provides little basis for declaring which of the components make so little contribution to the total variance that they can be ignored, even though the first three components account for 96% of the total variance.

Original variable data can be back-calculated from the principal component scores and the principal component vectors. When all of the principal component vectors are used in the back-calculation, the original variable data are obtained and the CD has its maximum value of one. When one or more principal component vectors are discarded, the back-calculated variable data are merely an approximation of the original data and the CD is less than one. The coefficient of determination of each variable can be calculated for each set of principal component vectors. Johnson et al. (2007) used this same approach and also included arrays of scatter plots of the original and back-calculated variable data. If original variable data are well-approximated by the principal component back-calculation, the data cloud of back-calculated data plotted over original data will fall along the 1-to-1 line. Figures 2.3 through 2.5 show the back-calculated data plotted against the original data when one, three and five principal components are retained.

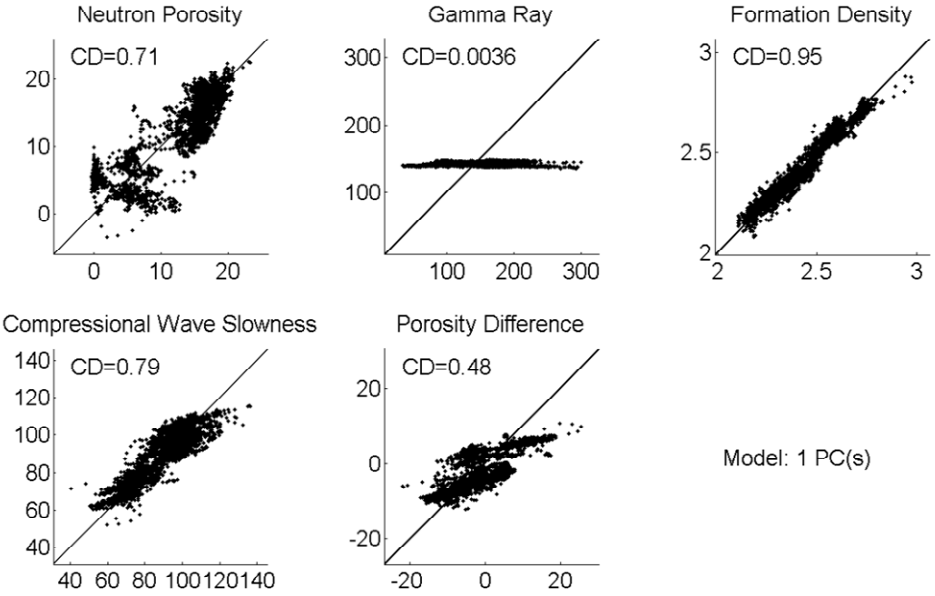

Figure 2.3. Results of PCA where only the first PC was retained. Back-calculated variable data (y axes) are plotted against original variable data (x axes) for each variable. The scatter plots and CDs indicate that the density data are well-approximated when only the first principal component is retained. The other variables are not well represented. This is especially true of the gamma variable.

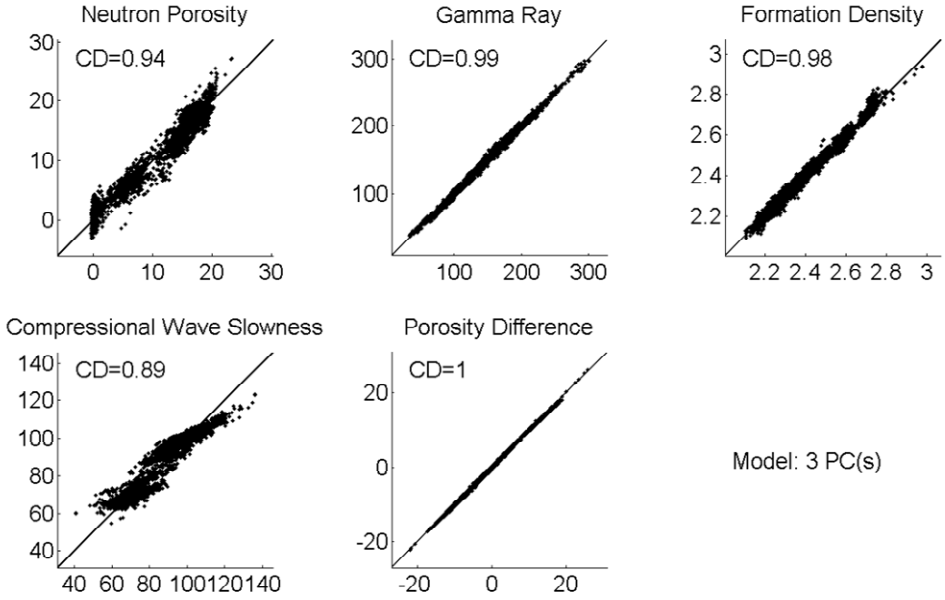

Figure 2.4. Results of PCA where the first three PCs were retained. All of the variables are well-approximated by the 3 PC model. The gamma, density, and porosity difference variable CDs are all approaching unity.

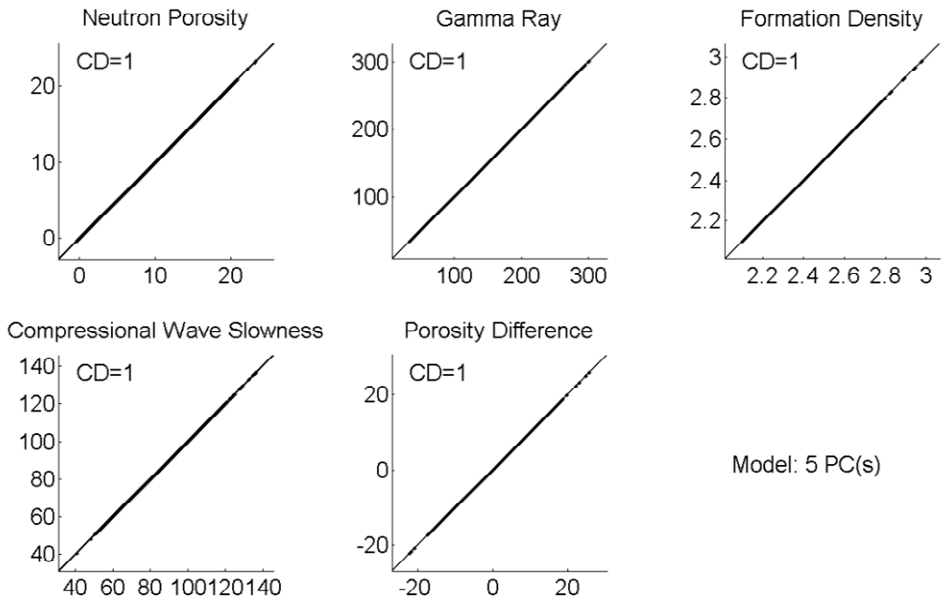

Figure 2.5. Results of PCA where all five PCs were retained. The scatter plots and CDs show that when the variable data are back-calculated from all of the principal components, the back-calculated data are identical to the original data. This is true by definition.

When all five principal components are retained (see Figure 2.5) the data falls on the 1-to-1 line and the computed CDs all have a value of one. This result shows that when the data are back-calculated using all of the principal components, the back-calculated data are precisely equal to the original data; this is true by definition.

Figure 2.4 shows that a principal component model comprised of only the first three principal components can be used to reproduce the original data relatively well. In each of the plots, the data fall near the 1-to-1 line. The CDs are also relatively high for each log response. This result shows that each of the five original variables is well modeled by the three-principal-components model. The appropriateness of a three-principal-components model is further verified by the fact that the first three principal components account for 96% of the total variance; the last two principal components can

be disregarded with only a minimal (4%) loss of total variance. A three-principal-component model consisting of the first three principal components was selected for further analysis and investigation, including regression of the photoelectric factor data obtained from mineralogic analysis of the well cuttings.

One great benefit of the reduction in dimensionality in the present case is that the reduced-dimensionality data can be plotted and explored graphically. A three-dimensional scatter plot of the principal component scores of the data gives some additional insight into the structure of the data (Figure 2.6). The colors of the individual data points were assigned based on a color gradient correlated with the depths at which the data were recorded. The data from the shallowest depths are shown in blue; data from the deepest depths are shown in red. The depths of the various geologic formations intersected by the well are also indicated

From Figure 2.6 it is evident that the data have an underlying structure that may have been undetectable in the original variable data. The data are generally grouped into two distinct clouds. In addition to being distinct based on their position in the Cartesian 3-space, the data are also distinct based on the depth (represented as color) at which the log data were observed. The data from the shallower portions (shown on the graph in blue and green) of the stratigraphic column appear in the group with a low PC1 score and high PC2 score (the shallow group). The data from the deeper portions of the column (shown in yellow and red) appear in the group with high PC1 scores and low PC2 scores (the deep group). The transition from the shallow group to the deep group appears to fall at approximately 5150 ft MD. This is near the bottom of the sedimentary Salt Lake Formation (see the color map and approximate lithologic column shown in Figure 2.6).

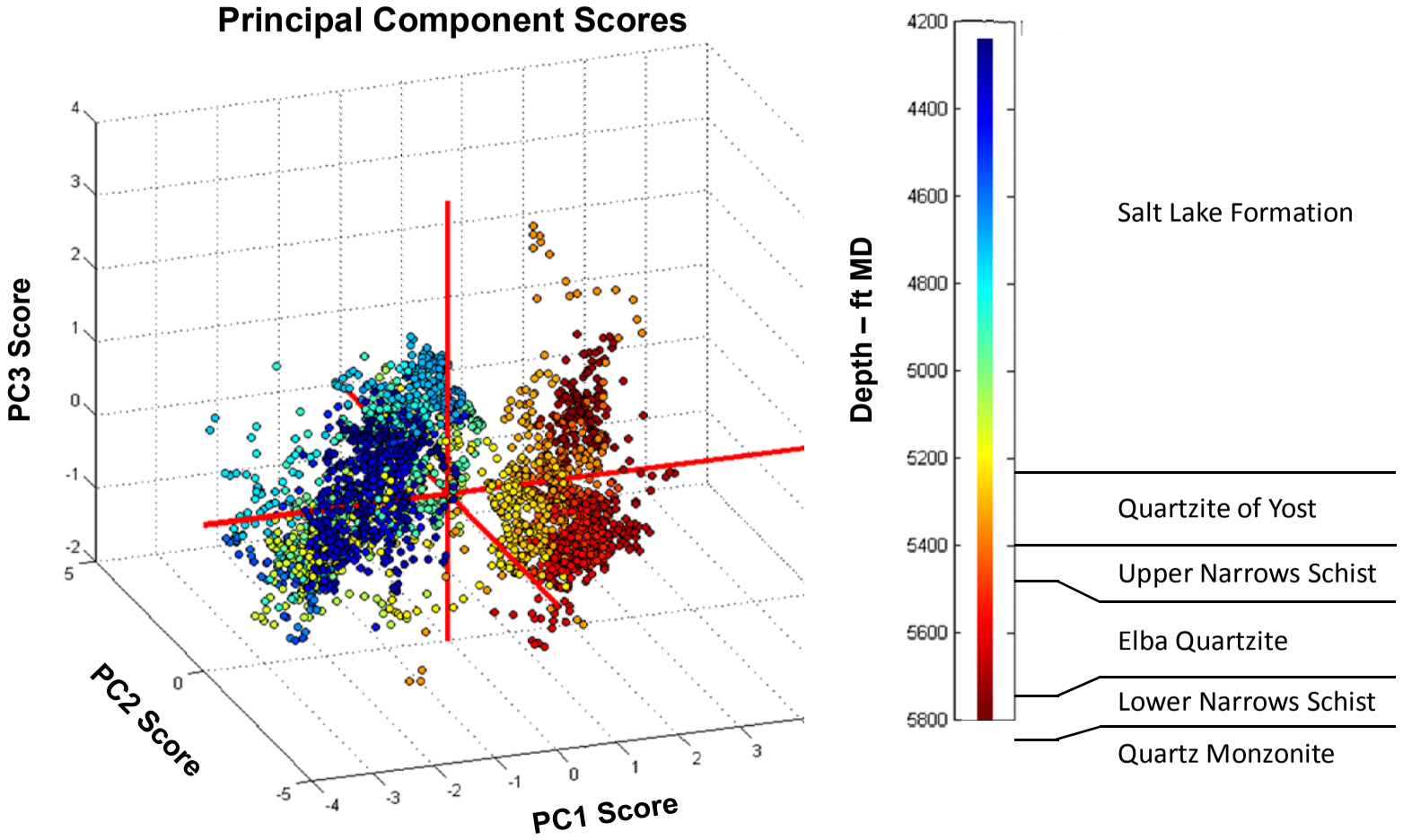

Figure 2.6. A three-dimensional scatter plot of principal component scores and an approximate lithologic column. The colors of individual data points correspond to depth: data recorded at shallower depths are shown in blue while data recorded at greater depths are shown in red.

The well intersects metamorphic units, beginning with the Quartzite of Yost, at approximately 5230 ft MD.

Regression analyses and analyses of variance were performed in order to identify relationships between log-derived data (either log data or principal component scores) and photoelectric cross section. The photoelectric cross sections of the 19 cuttings samples used in the regression analyses were determined based on their mineralogy as described previously (see Table 2.3).

As can be seen in Table 2.3, the exact depth of origin of cuttings samples is unknown; samples are identified as originating from within a range of 10 to 20 feet. The imprecise knowledge of the origin of the cuttings is a result of the method by which cuttings are obtained: cuttings come to the top of the wellbore along with the drilling mud, flowing up the well annulus. To compensate for this depth uncertainty, calculated photoelectric cross sections were assumed to represent the average bulk photoelectric cross section of rocks present in the given depth intervals. Well log data and principal component scores were also averaged within each of the depth intervals. Regression and analysis of variance were performed using the calculated average photoelectric cross sections and well log and principal component score data averaged within the same depth intervals.

Both linear and multiple-linear regression analyses were performed. Linear regression analyses were performed using each of the log variables and principal components as regressors. Multiple regression analyses were also performed using various combinations of log variables or principal components. Analyses of variance were performed for each regression and F statistics were calculated. The *F* statistic

Table 2.3. Photoelectric cross sections of the bulk cuttings samples.

Cuttings Sample	Photoelectric Cross Section (barns/electron)
4360 - 4380 ft	2.52
4440 - 4460 ft	2.32
4500 - 4510 ft	2.59
4640 - 4650 ft	2.28
4670 - 4680 ft	2.32
4710 - 4720 ft	2.29
4860 - 4880 ft	2.18
4980 - 5000 ft	3.07
5060 - 5080 ft	2.41
5100 - 5110 ft	2.76
5160 - 5180 ft	2.63
5260 - 5280 ft	2.62
5320 - 5340 ft	2.35
5400 - 5420 ft	2.13
5540 - 5550 ft	2.01
5580 - 5590 ft	1.95
5660 - 5670 ft	2.05
5710 - 5720 ft	1.88
5770 - 5780 ft	2.44

provides a measure of the statistical significance of the regression. Values of the *F* statistic are tabulated for specific degrees of freedom and confidence levels. If the *F* statistic of a regression analysis is found to be greater than the tabulated *F* value for the given degrees of freedom and confidence level, the regression is statistically significant. Table 2.4 lists the regressors in the various regression analyses and also provides the "goodness of fit" (R^2) and *F* values calculated for each regression analysis. The table

Table 2.4. Results of linear and multiple-linear regression analyses of photoelectric cross section over various regressors.

Regressor(s)	R^2	F	$F/F_{critical}$
Principal Component 1	0.342	8.85	1.99
Principal Component 2	0.013	0.23	0.05
Principal Component 3	0.025	0.44	0.10
Neutron Porosity	0.322	8.08	1.81
Gamma	0.040	0.70	0.16
Formation Density	0.360	9.58	2.15
Compressional Wave Slowness	0.200	4.24	0.95
Porosity Difference	0.161	3.25	0.73
Principal Component 1 Principal Component 2 Principal Component 3	0.398	3.31	1.00
Principal Component 1 Principal Component 2	0.374	4.78	1.32
Neutron Porosity Gamma Formation Density Compressional Wave Slowness Porosity Difference	0.473	2.33	0.77
Gamma Compressional Wave Slowness	0.280	3.11	0.86
Neutron Porosity Gamma Formation Density Compressional Wave Slowness	0.473	3.14	1.01

also gives the ratio of the *F* value to the critical *F* value for that specific regression analysis. Critical *F* values differ depending on the degrees of freedom and the significance level. The ratio of calculated *F* value to critical *F* value provides a basis for comparison between regression models which had differing degrees of freedom and therefore differing critical *F* values. Critical *F* values used here all assume a 95% confidence level.

The differences between the implications of the goodness of fit or R^2 value and the F value are subtle. The R^2 value is a measure of how well a data set is fit by a regression analysis; R^2 is a measure of the scatter of a data set relative to a regression line. The F statistic, however, is a measure of the functional dependence of one variable on another. Higher F values indicate a higher likelihood of functional dependence. The difference between R^2 and F can be seen in Table 2.4 where the highest F value (F = 9.58) is associated with a relatively low R^2 value; conversely, the highest R^2 value (R^2 = 0.473) is associated with a relatively low F value.

In this study, the selection of the regression model used in further analysis was based on a comparison of the $F/F_{critical}$ ratios. Based on that metric, regression over formation density (R^2 = 0.360; F = 9.58) was selected as the best regression model. The regression model is

$$P_e = -0.174\rho + 2.364 \tag{2.3}$$

where P_e is photoelectric cross section and ρ is standardized formation density. Figure 2.7 is a scatter chart of the photoelectric cross section over standardized formation density data. The linear regression line is also shown superimposed over the scatter data.

The linear regression model allowed the creation of a photoelectric pseudo log which in turn allowed for the calculation of mean interatomic distance and the use of Williams and Anderson's model to predict the thermal conductivity of rocks in the Raft River well RRG-3A. As outlined in Williams and Anderson (1990) and originally documented by Ellis (1987), photoelectric cross section was used to determine an

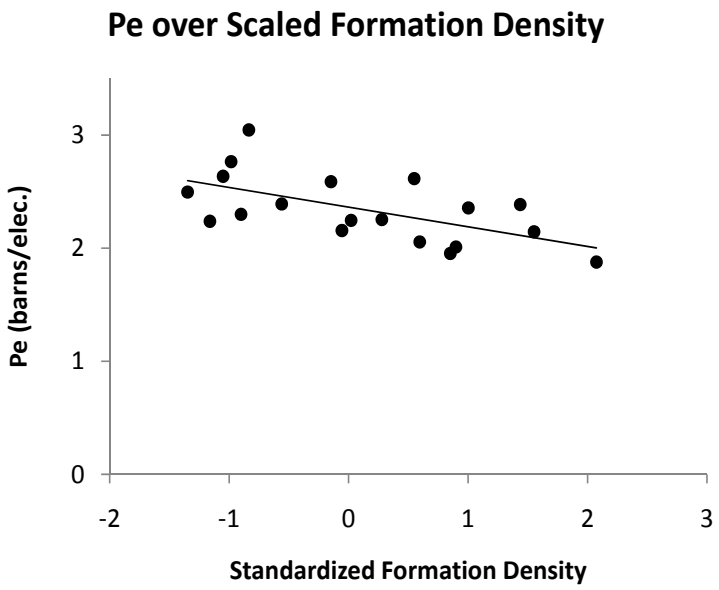

Figure 2.7. Regression of photoelectric cross section over standardized formation density.

"effective atomic number" Z_{meas} according to

$$Z_{meas} = 10P_e^{0.2778} \tag{2.4}$$

Mean atomic mass was then calculated as described by Williams (1989) as

$$\bar{M} = \frac{(Z_{meas} + 26.0)}{1.88} \tag{2.5}$$

Mean interatomic distance was calculated according to

$$a = \left(\frac{\bar{M}}{\rho}\right)^{1/3} \tag{2.6}$$

Finally, the model of Williams and Anderson (eq 2.1) was used to calculate thermal conductivity using compressional wave slowness and formation density logs and also using the shear wave slowness and photoelectric pseudo logs. The creation of the

continuous photoelectric and shear wave slowness pseudo logs allowed thermal conductivity to be calculated on a continuous basis through the depth of the logged interval of the well. The calculated thermal conductivity pseudo log over the bottom section of the logged interval is shown in Figure 2.8.

To provide a basis for evaluating the accuracy of the model results, it was desirable to measure the thermal conductivity of actual core samples from Raft River well RRG-3. Very few competent rock samples were available from well RRG-3 for thermal conductivity measurement. The scarcity of testable samples and the difficulty and expense associated with laboratory measurements of thermal conductivity provided the impetus for using methods such as statistical analysis and the Williams and Anderson model to approximate thermal conductivity. One section of drill core covering the interval of approximately 5270 to 5272 ft MD from well RRG-3 leg C (RRG-3C) was obtained. Several 1.5-in horizontal plugs were taken from the core and various tests, including two tests of thermal conductivity, were conducted. Tests of thermal conductivity were conducted by TerraTek, a Schlumberger company, in 2010. Rock samples were saturated with a 0.4% sodium chloride brine solution and tests were conducted under representative confining and pore pressures of 2120 psi and 100 psi, respectively, and at varying temperatures. The results of the thermal conductivity measurements on two samples – EGM1-1, which originated from 5270.1 ft MD, and EGM2-5, which originated from 5272.15 ft MD – are provided in Tables 2.5 and 2.6.

Williams and Anderson's semiempirical model is based on the theory of phonon conduction and on regression of laboratory-obtained rock properties. Tests by Williams and Anderson were conducted at 298 K; the results of those tests and their model are

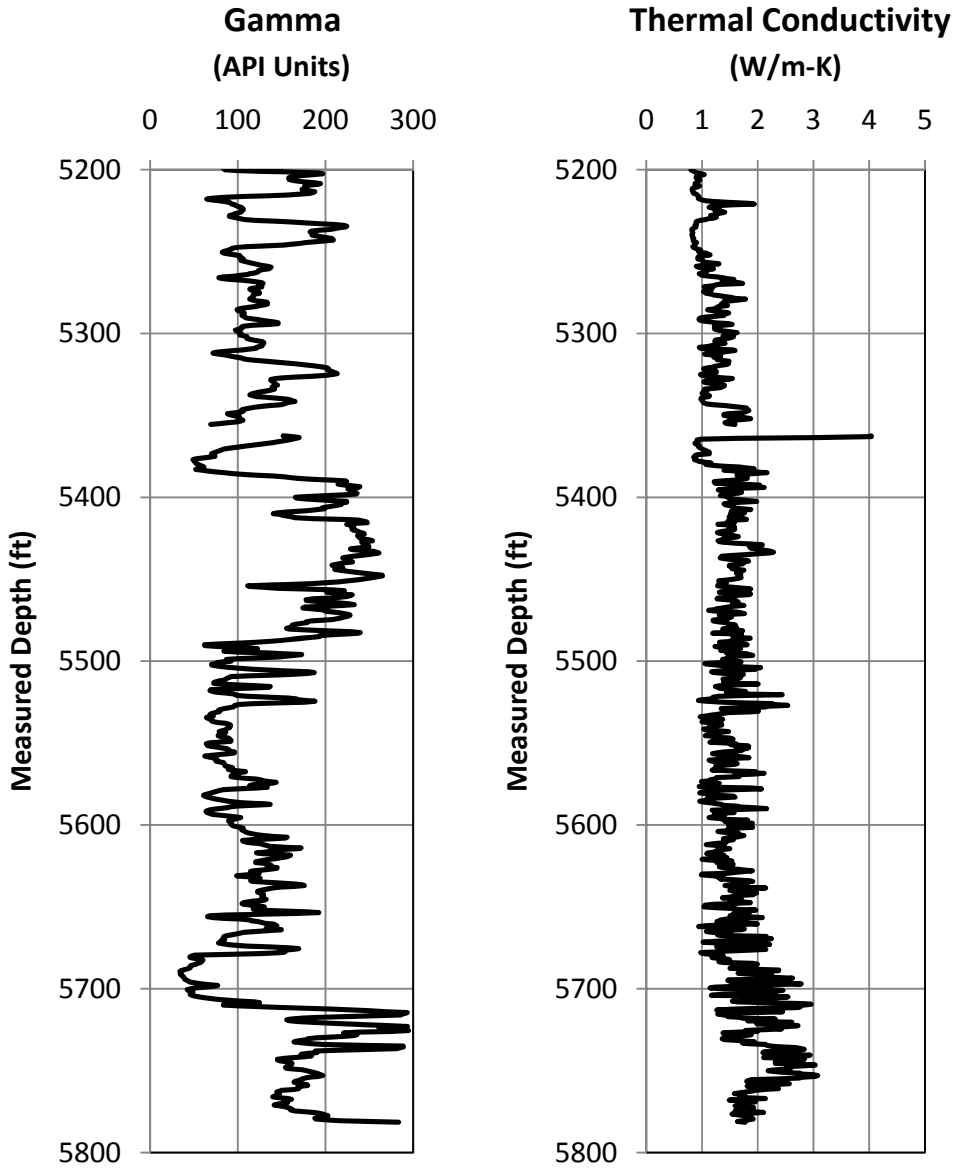

Figure 2.8. Thermal conductivity pseudo log calculated from formation density and compressional wave slowness logs and from the photoelectric and shear wave slowness pseudo logs. The natural gamma ray log is shown for reference

Table 2.5. Measurements of thermal conductivity of sample EGM1-1.

Temperatures (°C)	Thermal Conductivity (W/m·K)
34.0	1.775
68.0	1.850
138.0	1.929
Average over temperatures	1.815

Table 2.6. Measurements of thermal conductivity of sample EGM2-5.

Temperatures (°C)	Thermal Conductivity (W/m·K)
33.4	1.210
69.6	1.307
133.5	1.315
Average over temperatures	1.277

therefore specific to that temperature. The model predictions for the two samples are therefore compared with the lowest-temperature thermal conductivity measurements. Those measurements of thermal conductivity were taken at 34.0 °C (307.2 K) and 33.4 °C (306.6 K) for samples EGM1-1 and EGM2-5, respectively. Table 2.7 gives the thermal conductivity predicted by the Williams and Anderson model and the thermal conductivity from laboratory experiments. The table also shows the error relative to the laboratory-obtained thermal conductivities.

Measurements of thermal conductivity of core samples from other parts of the Raft River geothermal reservoir were taken in experiments conducted by Peterson et al. (1982). These measurements are reproduced Table 2.8 for the sake of comparison.

Table 2.7. Thermal conductivities predicted by the Williams and Anderson model and from laboratory-obtained data.

Sample Number	Laboratory Thermal Conductivity (W/m·K)	Thermal Conductivity from model of Williams and Anderson (W/m·K)	Error Relative to Laboratory-obtained Thermal Conductivity (%)
EGM1-1	1.775	1.289	27.4
EGM2-5	1.210	1.192	1.5

Table 2.8. Thermal conductivity of samples from the Raft River reservoir. Data reproduced from Peterson et al. (1982).

Well	Depth (m)	Rock Type	Temperature (°C)	Thermal Conductivity (W/m·K)
RRG-1	1372	Devitrified Tuff	22	2.05
			98	1.98
			155	1.99
RRG-2	1286	Graywacke	26	2.39
			89	2.21
			105	2.20
			150	2.19
RRG-3C	1519	Sandy Devitrified Tuff	26	2.37
			85	2.29
			140	2.30
RRG-4B	1415	Silty Devitrified Tuff	26	2.45
			85	2.27
			125	2.24

The thermal conductivity pseudo log (Figure 2.8) indicates that the ranges of conductivity values predicted by Williams and Anderson's model is relatively small: approximately 2 W/m·K; recognizing the similarly small range in values reported by TerraTek, the thermal conductivity values for sample EGM1-1 predicted by the model and measured in the lab are significantly different.

Comparing model-predicted values from RRG-3A with laboratory-obtained data from RRG-3C was not ideal but was necessitated by the limited availability of data and samples: log data were available from leg A while core samples were available from leg C. The logs and core being sourced from the two different legs clearly contributes to the discrepancy in the values though other possible sources of error may also play a role.

Anisotropy may contribute to the large error in the results from sample EGM1-1. As discussed previously, the model-predicted thermal conductivity is the vertical thermal conductivity. However, the TerraTek thermal conductivity measurements were on core plugs which ran perpendicular to the bore hole. The laboratory-measured thermal conductivity is therefore a horizontal thermal conductivity. Pribnow and Sass (1995) noted some possible affects of anisotropy which were particularly evident in gneisses.

Other possible sources of discrepancy between the results of the two methods include error due to calculation of shear wave slowness using Brocher's regression equation. In their original paper, Williams and Anderson note that their model is extremely sensitive to both compressional and shear wave velocities and their ratio. Even a small error in shear wave slowness calculated from Brocher's regression equation might have a significant impact on the quality of the result. Pribnow and Sass (1995) point out that features such as microcracks, to which sonic velocities are sensitive, will result in inaccuracies in results predicted by Williams and Anderson's model.

There is also some question as to the accuracy of the laboratory-obtained thermal conductivity values. Typically, thermal conductivity decreases with increasing temperature. In the data reported by the laboratory, thermal conductivity is seen to

increase very slightly with increasing temperature. This behavior calls into question the accuracy of the experimental data.

2.4.1 Sensitivity Analysis

In light of the small variability in thermal conductivity values and the relatively large discrepancy between methods, analyses of sensitivity were performed. Analyses of sensitivity of power and cumulative energy production to thermal conductivity were performed. Tester and Smith (1977) describe a method of estimating power production as a function of rock and water properties, fractured reservoir geometry, and water flow rate. According to Tester and Smith, power can be calculated according to

$$P(t) = \eta \dot{m}_w C_w (T - T_{min}) \mathrm{erf}\left(\sqrt{\frac{(\lambda_r \rho_r C_r)}{t}} \frac{\pi R^2}{\dot{m}_w C_w} \right) \tag{2.7}$$

where *P(t)* is power production in Joules per second, η is a fraction of the total recoverable power, $\dot{m}_w$ is the flow rate of water in kilograms per second, λ_r is the rock thermal conductivity in watts per meter per Kelvin and ρ_r is rock density in kilograms per cubic meter. T_{min} refers to the temperature of the circulating water at injection and T is the temperature of the reservoir, both in degrees Celsius. Water and rock heat capacities in Joules per kilogram per Kelvin are given by C_w and C_r, respectively. The model assumes single radial (penny-shaped) fracture of radius, R, in meters. Time, t, has units of seconds.

Power production curves (as functions of time) relative to initial power production were calculated (Figure 2.9). The plot shows that an enhanced geothermal system created in a reservoir with a rock thermal conductivity of 3.5 W/m·K will produce

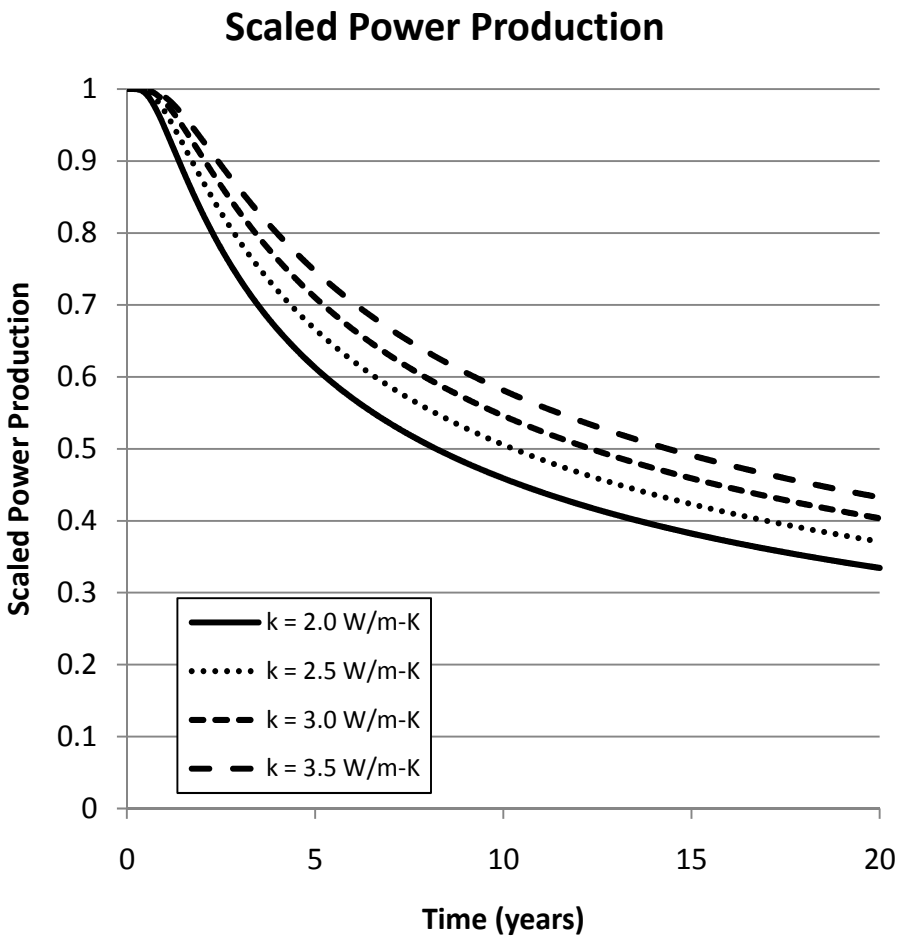

Figure 2.9. Scaled power production. Power production was calculated according to eq 2.7 as outlined by Tester and Smith. Power production curves were scaled by initial power production.

power at a rate approximately 29% greater than the same system in a reservoir with a rock thermal conductivity of 2.0 W/m·K. Cumulative energy production curves were also produced (Figure 2.10). In this case, plots of cumulative energy production were scaled by the total 20-year cumulative energy production of a system in a reservoir with a rock thermal conductivity of 2.0 W/m·K. The plot shows that approximately 20% more energy will be produced by a system in a reservoir with a rock thermal conductivity of 3.5 W/m·K than in a comparable system in a reservoir with a rock thermal conductivity

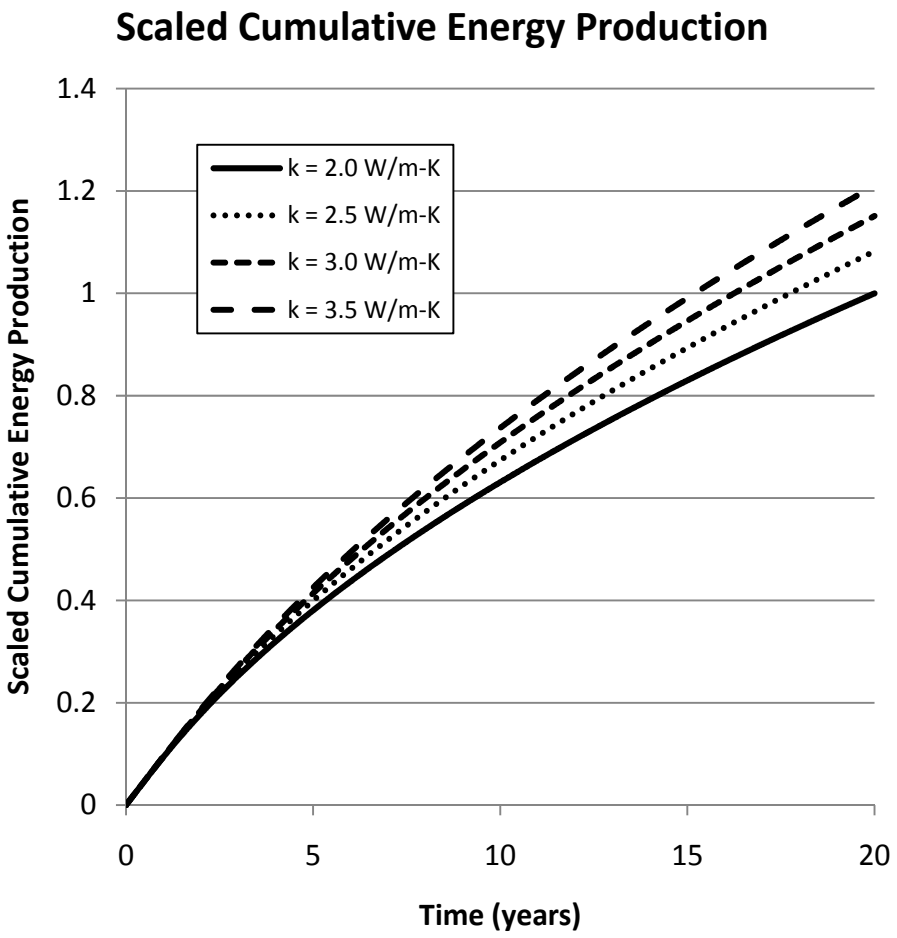

Figure 2.10. Scaled cumulative energy production. Cumulative energy production curves were calculated using the power production data from eq 2.7. All data were scaled by the total 20-year cumulative energy production of a system operating in a reservoir with rock thermal conductivity of 2.0 W/m·K

of 2.0 W/m·K. The power production plot (Figure 2.9) also indicates that power production is largely insensitive to rock thermal conductivity when only short (i.e., less than six months) production time periods are considered.

2.5 Conclusions

While the Williams and Anderson model does not yield consistently good results in the samples that were tested in the laboratory, it does have the attractive benefit of

being able to predict thermal conductivity based on well logs, which are commonly available. The model also adds value by generating a thermal conductivity pseudo log that predicts thermal conductivity continuously. While it may only provide estimates of thermal conductivity, those calculations can be quite valuable when testable samples are scarce or laboratory measurements are prohibitively expensive.

2.6 Notes

Two other multivariate analysis methods were implemented to investigate well logs from wells in the Raft River geothermal reservoir. Discriminant function analysis was used in an attempt to correlate mean atomic mass with well log data. In this case, the discriminant function was used in a manner similar to principal components. However, the limitations of the method, including the requirement of some understanding of data structure a priori, and significant problems with the data set (the method was applied to well RRG-2 in which the gamma ray log signal was saturated through much of the well leading to gaping holes in the data) prevented any conclusions from being reached.

Cluster analysis was also applied to log data. Well logs used in the cluster analysis were first conditioned and standardized as described previously. A principal component analysis was conducted and the principal component 1 (PC1) pseudo log was calculated. Based on the PC1 pseudo log, a segmentation algorithm was applied as a first pass at data reduction. Then a cluster analysis algorithm was applied to the segmented data. The cluster analysis yielded large intervals of logged well which were found to be similar based on their log values. The method has been used in similar applications (Gonçalves, 1998; Tavakoli and Amini, 2006; Crampin, 2008). The clusters that result from cluster analysis only gain physical meaning when they are correlated with

independently-obtained data. For example, in order to define the thermal conductivity of a cluster of observations, the thermal conductivity of at least one observation within the cluster must be known. Since all observation within a cluster have similar properties, the known thermal conductivity of one observation can be ascribed to all other observations within the cluster. No further work was done in correlating physical properties such as thermal conductivity with the cluster analysis findings.

Appendix A provides a brief discussion of the theory of discriminant function analysis and cluster analysis along with references for further information.

3. STABILITY OF PROPPANTS UNDER GEOTHERMAL CONDITIONS

3.1 Introduction

Traditional geothermal systems are limited to reservoirs where high temperatures, water, and high permeability or conductive faults or fractures are all found. In more recent years, development of engineered geothermal systems (EGS) has been proposed in areas of high heat flow but low permeability and/or insufficient water saturation. EGS have the potential to greatly increase geothermal energy production and expand production into areas previously thought to lack recoverable geothermal resources.

Engineered geothermal systems are created by hydraulic fracturing, a practice that has been employed in the oil and gas industry since the late 1940s. Hydraulic fracturing is accomplished by pumping generally large volumes of highly pressurized water (or other water-based fluid) into a rock formation with the goal of creating a new fracture network or expanding or re-opening an existing network. While hydraulic fracturing has been practiced in the oil and gas industry for decades with great success, application of hydraulic fracturing methods in geothermal systems has been much more limited and has met with only limited success.

Hydraulic fractures in oil and gas reservoirs are almost always “propped” open in order to maintain acceptably high fracture permeability when the injection of high-pressure fracturing fluid is complete and fracture pressures return to background levels.

Granular materials such as sand or other engineered products, broadly defined as "proppant," are pumped into hydraulic fractures to hold them open.

Various kinds of proppants have been successfully used in oil and gas reservoirs. Some research on proppant performance in geothermal conditions has also been published. Stoddard et al. (2011) published findings of experiments on propped fracture permeability at elevated temperature; however, the tests were all relatively short (on the order of hours). Weaver et al. (2006) performed studies of fluid flowing through proppant packs and suggest that diagenesis plays a role in conductivity decline. Freeman et al. (2009) performed crush tests of water-saturated proppant at elevated temperatures and found that crush fractions were increased by water saturation. Maurer Engineering (1980, 1981) performed a significant study of proppants under geothermal conditions, which included long-term confined flow-tests at temperatures up to 500 °F. However, even the long-term tests lasted only 50 h. Knox and Weaver (1989) state that dissolution of sintered bauxite proppant may occur because formation fluids are not likely to be in equilibrium with bauxite.

Engineered geothermal systems may be expected to be in operation for 20 to 30 years. The long-term compatibility of specific proppant types to geothermal conditions must be understood since ill-suited proppant may dissolve leading to weakening or act as nucleation sites for precipitation of dissolved solids. In either case, fracture conductivity could be negatively impacted. The present study has been conducted to evaluate the effects of simulated geothermal conditions on proppant.

Three types of commercially-available proppant were tested under simulated geothermal conditions. The various proppants – 30/60[2] sintered bauxite, 20/40 resin-coated bauxite and 40/70 quartz sand – were exposed to several water types at elevated temperatures (up to 230 °C) for extended time periods up to 11 weeks. Mixtures of proppant and crushed granite were also tested. Granitic formations are proposed as prime targets for EGS development; particles of crushed granite were mixed with proppant grains for use in tests of chemical stability to more closely simulate expected in situ conditions in potential EGSs.

Before and after testing in the simulated geothermal conditions, proppant grains were analyzed. Proppant grains were imaged using scanning electron microscopy (SEM). Proppant composition was analyzed using energy dispersive x-ray spectroscopy (EDS) to attempt to locate areas of alteration of chemistry due to dissolution or precipitation. Textural changes related to exposure to simulated geothermal conditions have been observed in SEM micrographs.

Proppant grains used in tests of long-term chemical compatibility were also tested for their crushability. The crushability and compliance of used proppant were compared to the crushability and compliance of fresh proppant to determine if the proppant was weakened by long-term exposure to geothermal conditions.

[2] The size of proppant grains are given as the sieve numbers which bracket the proppant grains. For example, grains of a 30/60 proppant all pass through a #30 sieve (larger particles are screened out by the #30 sieve) but do not pass through the #60 sieve. Practically speaking, some very small percentage of grains may be smaller than the #60 sieve or larger than the #30 sieve. Particle size distributions and mean particle size are provided in data tables for each proppant type.

3.2 Experimental Methods

Two rounds of separate but related experiments were conducted on three different types of proppant. The first round of experiments was designed to test the chemical stability of the proppants when exposed to simulated geothermal conditions. The second round of experiments was designed to examine the strength of proppants both before and after exposure to the simulated geothermal conditions.

3.2.1 Materials

Tests of chemical stability of proppant were conducted on three proppant types in the presence of granite and three different water types. Crush tests were conducted on "fresh" and "used" samples of two of the three proppant types. Throughout this discussion of proppant testing, *fresh* refers to proppant as obtained from the manufacturer; *used* refers to proppant after exposure to simulated geothermal conditions in the tests of chemical stability.

3.2.1.1 Proppant

Three different proppant types – 30/60 sintered bauxite, 20/40 resin-coated bauxite and 40/70 quartz sand – were tested for chemical stability under simulated geothermal conditions. Tests of strength and compliance were conducted on fresh and used samples of both 30/60 sintered bauxite proppant and 20/40 resin-coated bauxite proppant. The properties of the three proppants tested in the study are discussed below.

3.2.1.1.1 30/60 sintered bauxite. Sintered bauxite proppant has several characteristics that make it an ideal material to be used in deep oil and gas wells, including its strength, deformability and resistance to corrosion (Atteberry, 1979). In

addition it is thermally stable. Proppant technical data provided by the manufacturer is included in Tables 3.1 through 3.3 and Figure 3.1. The 30/60 proppant used has a bulk density of 130 lb/ft^3 and mean particle diameter of 0.501 mm. Table 3.3 contains closure stress and permeability data. Closure stress is the in situ stress (pounds per square inch) that is exerted by a rock formation acting to close a fracture.

SEM images of fresh 30/60 sintered bauxite proppant show the surface textures. Figure 3.2A indicates that there are at least two different proppant surface textures. The surface of the grain on the left appears smoother and darker in the image, while the surface of the grain on the right appears rougher and is punctuated by surface craters. Figures 3.2B and 3.2C are close-ups of the two proppant grain surfaces. EDS analysis

Table 3.1. 30/60 sintered bauxite proppant general data provided by manufacturer.

Specific Gravity	3.63
Bulk Density	130 lb/ft^3
Crush at 12,500 psi	1.9%
Absolute Volume	0.033 gal/lb$_m$
Mean Particle Diameter	0.501 mm

Table 3.2. 30/60 sintered bauxite proppant sieve data provided by manufacturer.

Sieve No.	Mesh Size (mm)	Retained (%)
30	0.59	3
40	0.42	77
50	0.30	18
60	0.25	2

Table 3.3. 30/60 sintered bauxite proppant permeability data provided by manufacturer.

Closure Stress (psi)	Permeability (darcy)
6000	169
8000	137
10,000	120
12,000	103
14,000	86

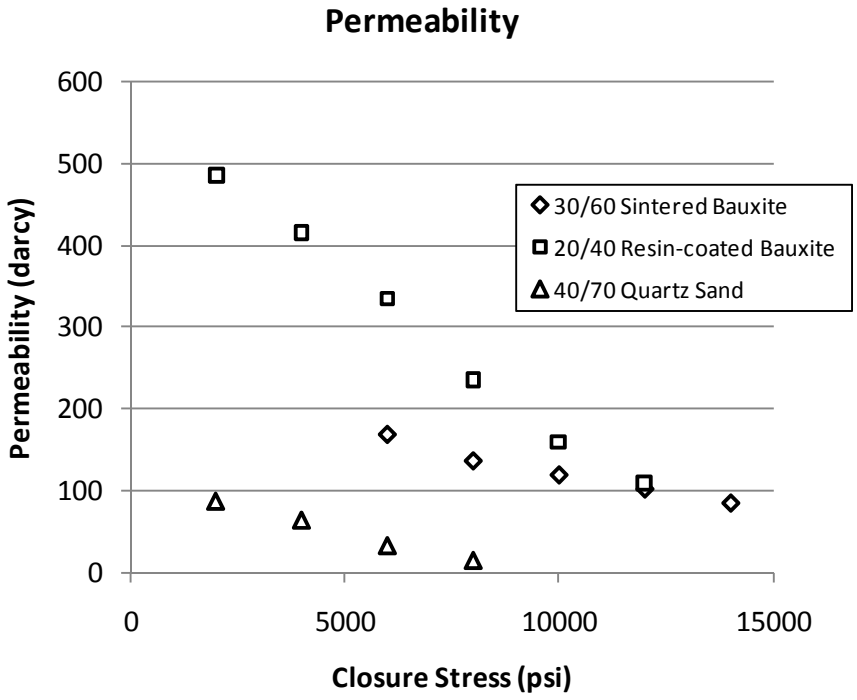

Figure 3.1. Absolute permeability of three proppants as a function of closure stress. Bauxite proppant is generally stronger than quartz sand proppant and therefore has greater resistance to crushing as seen by the rate at which permeability declines as closure stress increases. Data provided by proppant manufacturers.

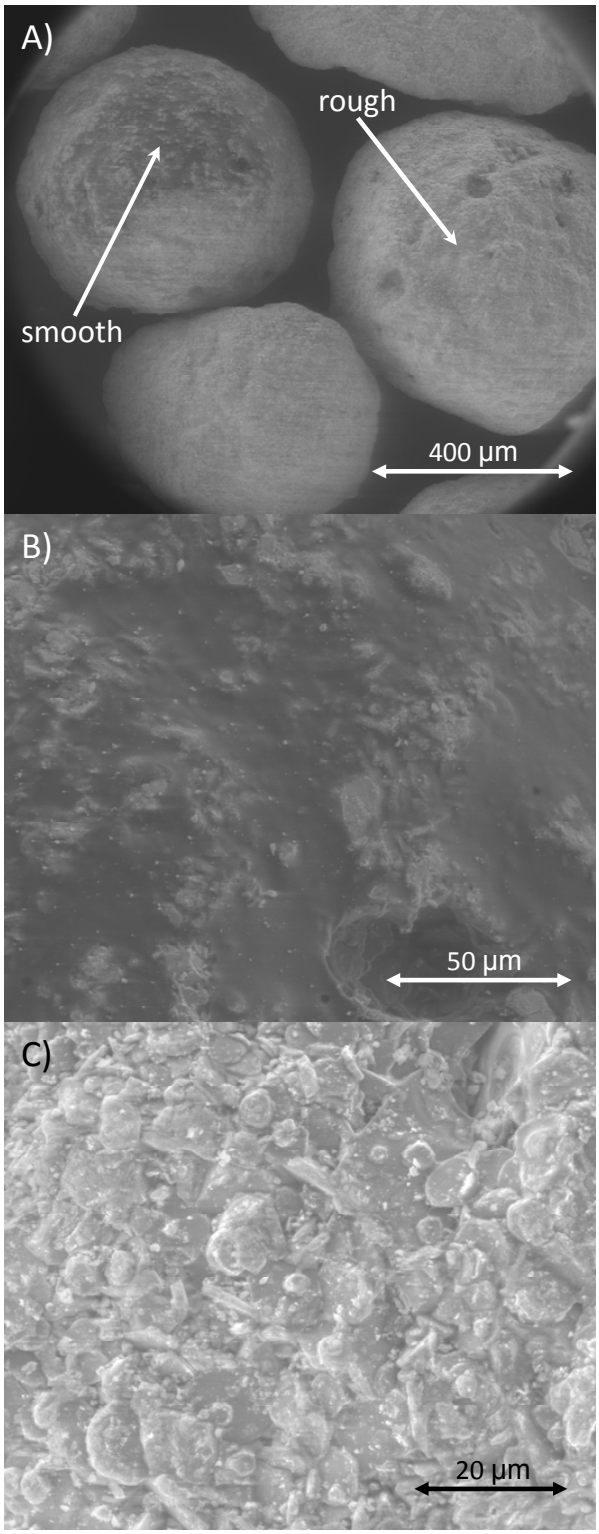

Figure 3.2. 30/60 sintered bauxite proppant SEM images. A) Two different surface textures are observed. EDS analysis indicates that the two surfaces also have different compositions (see Table 3.4). B) Close-up of smooth proppant grain surface. C) Close-up of rough proppant grain surface.

(Table 3.4) reveals that the chemistry in addition to the texture of the two grains are unique. Both proppant grains are fresh as provided by the manufacturer. Differences in texture and surface composition may be due to manufacturing process itself.

3.2.1.1.2 20/40 resin-coated bauxite. In they are not held in place by frictional forces, proppant grains can be washed out of hydraulic fractures and into the wellbore, especially in high flow-rate applications. Proppant flow-back can result in suboptimum conductivity. Additionally, proppant grains in the reservoir fluids may cause damage to pumps and other equipment. Resin-coated proppants have been designed to reduce the risk of proppant flow-back. Proppant grains that have been coated with an un-cured resin form a permeable solid pack in fractures under reservoir conditions when the resin cures. The resin and formation of the solid permeable pack serve to prevent proppant wash out. Proppant technical data as provided by the manufacturer is provided in Tables 3.5 through Table 3.7 and Figure 3.1. The 20/40 resin-coated proppant used in the present tests has a bulk density of 117 lb/ft^3 and a mean particle diameter of 0.71 mm.

Table 3.4. Composition of surfaces of two sintered bauxite proppant grains from EDS analyses of areas shown in Figure 3.2B and Figure 3.2C.

Element	Composition (wt%)	
	Figure 3.2B	Figure 3.2C
O	50	38.3
Al	28.9	39.5
Fe	21.1	22.2

Table 3.5. 20/40 resin-coated bauxite proppant general data provided by manufacturer.

Specific Gravity	3.2
Bulk Density	117 lb/ft3
Crush at 12,500 psi	4.0%
Absolute Volume	0.0374 gal/lb
Mean Particle Diameter	0.71 mm

Table 3.6. 20/40 resin-coated bauxite proppant sieve data provided by manufacturer.

Sieve No.	Mesh Size (mm)	Retained (%)
20	0.84	8
30	0.59	82
40	0.42	10
>40	0.42	Trace

Table 3.7. 20/40 resin-coated bauxite proppant permeability data provided by manufacturer.

Closure Stress (psi)	Permeability (darcy)
2000	485
4000	415
6000	335
8000	235
10,000	160
12,000	110

Figures 3.3A through 3.3C are photomicrographs of the proppant surface obtained using SEM. The EDS analysis of the composition of the area shown in Figure 3.3B is shown in Table 3.8.

From the photomicrographs in Figure 3.3, it is clear that the resin-coated proppant is not a homogenous solid and is, in fact, composed of varying mineral phases having different chemical compositions and textures. Figure 3.3C shows corundum crystals overlain by a different, iron-containing aluminosilicate mineral.

3.2.1.1.3 40/70 quartz sand. Sand proppant is substantially less expensive than bauxite proppants; however, sand proppants are significantly weaker than either of the bauxite proppants discussed above and are therefore subject to crushing in high closure-stress environments. Technical data of a generic 40/70 quartz sand proppant, as provided by a quartz sand proppant manufacturer, are given in Tables 3.9 through 3.11 and Figure 3.1. Bulk density of a generic 40/70 quartz sand proppant may be expected to be approximately 91 lb/ft^3; Mean particle size may be approximately 0.3 mm.

SEM images show the quartz sand proppant surface (Figures 3.4A and 3.4B). Results of EDS analysis provide the composition reported in Table 3.12.

3.2.1.2 Granite

Many potential EGS reservoirs are found in granitic rocks. In order to more closely simulate expected geothermal conditions, tests were conducted in the presence of crushed granite particles. In addition to the effects of water on proppant, it will also be important to know what if any interaction may occur between proppant materials and the host rock. In the present study, Little Cottonwood (Utah) granite was used. The granite

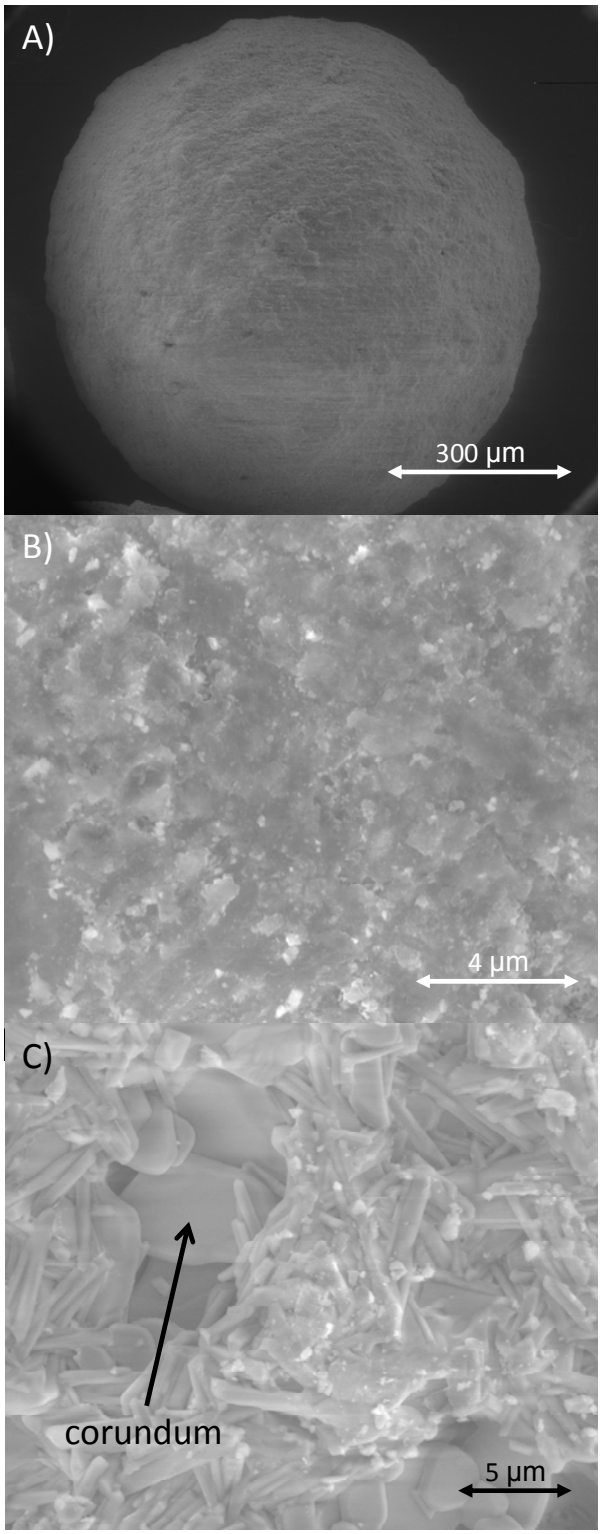

Figure 3.3. Photomicrographs of resin-coated bauxite proppant surfaces. A) Resin-coated bauxite proppant grain. B) Close-up of surface of proppant. C) Close-up on surface of proppant showing corundum crystals overlain by a different iron-containing aluminosilicate mineral.

Table 3.8. Composition of surface of 20/40 resin-coated bauxite proppant from EDS analysis.

Element	Composition (wt%)
O	43.1
Fe	15.1
Al	32.9
Si	8.8

Table 3.9. Generic 40/70 quartz sand proppant general data.

Specific Gravity	2.63
Bulk Density	91.1 lb/ft^3
Sphericity	0.7
Roundness	0.6

Table 3.10. Generic 40/70 quartz sand proppant sieve data.

Sieve No.	Mesh Size (mm)	Retained (%)
40	0.42	0.8
45	0.35	14.7
50	0.30	49.4
60	0.25	26.6
70	0.210	7.6
80	0.177	0.8

Table 3.11. Generic 40/70 quartz sand proppant permeability data.

Closure Stress (psi)	Permeability (darcy)
2000	88
4000	65
6000	34
8000	16

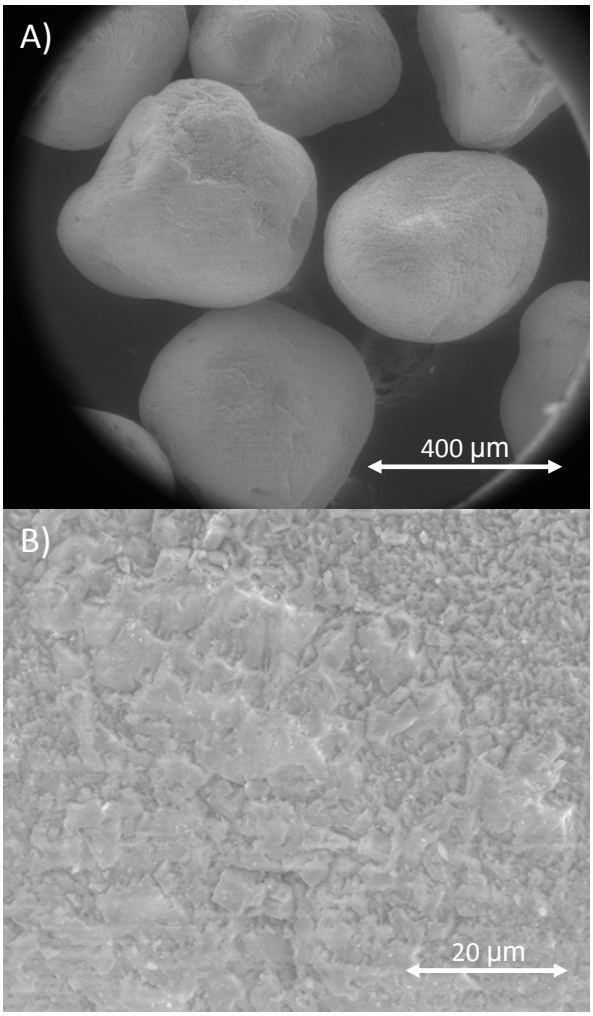

Figure 3.4. A) 40/70 quartz sand proppant SEM image. B) Close-up of surface of quartz sand proppant.

Table 3.12. Composition of surface of 40/70 quartz sand proppant from EDS analysis.

Element	Composition (wt%)
O	56
Si	44

was crushed to sieve size 30/65. Granite mineralogy obtained by X-ray diffraction analysis is contained in Table 3.13.

3.2.1.3 Water

Three different types of water were used over the course of the experiments. In the first experiments, deionized (DI) water was used. Deionized water is chemically active and is not a good analog for geothermal waters, which are expected to be saturated with various dissolved solids. Use of deionized water created an environment that is chemically more aggressive than would be expected to be found in a geothermal reservoir. Steam condensate, however, is often reinjected into the reservoir and is appropriately simulated by DI water.

In an effort to more closely simulate in situ conditions later experiments used Milli-Q[3] water spiked with tetraethyl orthosilicate (TEOS). TEOS reacts with water in a hydrolysis reaction to yield SiO_2 (silica) and ethanol. TEOS was added to water in an effort to create a solution with SiO_2 concentrated to near the quartz saturation limit at test temperatures. Silica concentration was determined by inductively coupled plasma mass

[3] Milli-Q water refers to highly-purified water produced by a Millipore Corporation purification system or similar purification system. Milli-Q water is more pure than deionized water.

Table 3.13. Mineralogic composition of Little Cottonwood stock granite.

Mineral	Composition (wt%)
Chlorite	7.0
Biotite	4.4
Quartz	23.7
Plagioclase	45.7
K-feldspar	19.2

spectrometry (ICP-MS) analysis to be 327 mg/kg. Aliquots from the prepared silica-spiked water were used in two of the tests of chemical stability of proppant.

In the latest experiments, geothermal brine from Raft River, Idaho, well RRG-1 was used. Two samples of water were provided by U.S. Geothermal, Inc., the operator of the Raft River geothermal plant. The first sample was collected before September, 2010; the second sample was collected on November 2, 2010. The first sample was used in Trial A and the second sample was used in all remaining trials. Results of the elemental analysis of the geothermal waters performed by Thermochem, Inc. are given in Table 3.14.

3.2.2 Tests of Chemical Stability

Experiments were designed to test the chemical stability of the three proppant types described above under simulated geothermal conditions. Tests were conducted in which proppant was exposed to water at elevated temperatures for extended periods of time up to 11 weeks. Most tests were conducted in the presence of crushed granite to

Table 3.14. Composition of DI water, silica-spiked Milli-Q water and geothermal brine from Raft River, Idaho, well RRG-1.

Element	Concentration (mg/kg)			
	DI Water	Silica-spiked Milli-Q Water	Raft River Geothermal Brine	
			Collected before Sept. 2010	Collected 11/2/2010
Na	<0.1	0.8	520	547
Mg	2	0.02	0.124	0.108
K	0.1	<0.002	34.2	36.5
Ca	5.9	0.29	55.2	59
Fe	<0.01	<0.002	<0.05	<0.05
SiO_2	1.5	327	121	129
Cl	6.2	<0.02	897	942
B	<0.1	1.2	0.205	0.213
Sulfate	Not Analyzed	Not Analyzed	56.8	58.3

create an environment similar to that expected to exist in potential EGS reservoirs. Key findings were expected to be dissolution and/or precipitation of solids.

3.2.2.1 Trials 1 through 5

Tests were conducted on 30/60 sintered bauxite proppant in the presence of the three different water types. Some trials used mixtures of proppant and crushed granite to more closely simulate conditions in candidate EGS reservoirs.

3.2.2.1.1 Apparatus. The first round of experiments (Trials 1 through 5) were conducted in stainless steel, fixed-bed autoclave reactors constructed of 1-in. tubing and end caps. The reactors were equipped with a pressure gauge and tubing sealed with valves. Figure 3.5 is a schematic drawing of the reactor vessels. The reactor temperature was measured using a thermocouple (inserted into the reactor through a Swagelok fitting

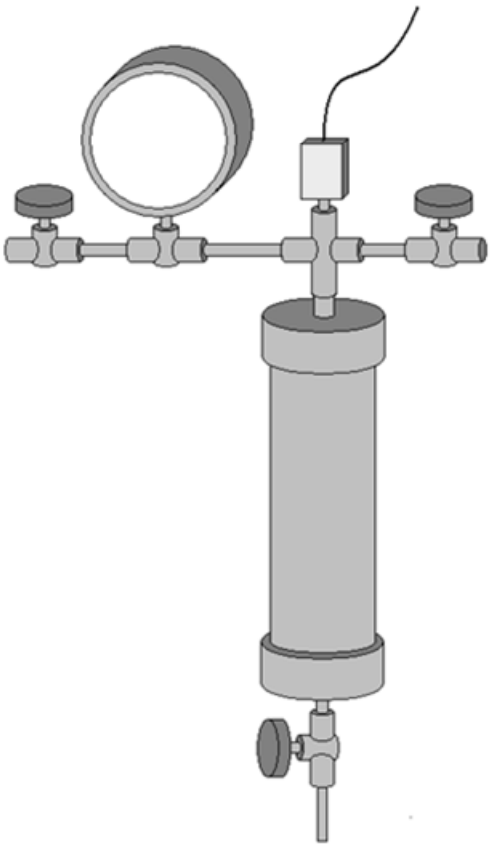

Figure 3.5. Schematic drawing of stainless steel fixed-bed autoclave reactor. The reactors were constructed of one-inch stainless steel tubing and end caps. Temperature was measured and controlled using a thermocouple inserted through a fitting at the top of the reactor and heat tape (not show) wrapped around the reactor.

at the top of the reactor) and maintained at the set temperature using computer control and heat tape wrapped around the outside of the reactor.

3.2.2.1.2 Method. Solids – proppant or proppant/granite mixtures – were loaded into the reactor vessels. Water was then slowly added to allow the water to fill the pore spaces. Water was added until the liquid level was slightly above the solid level ensuring that all solid grains were submersed. The reactors were then sealed with the thermocouple in place. Heat tape was wrapped around the reactors. Silicon tape was then wrapped around the reactor and heat tape to hold the heat tape in place and provide

some insulation. The reactors were then heated to the set temperature using the heat tape and held at the set temperature for up to 11 weeks. Each of Trials 1 through 5 was conducted at 200 °C. Table 3.15 contains the details of each trial.

At the end of each trial, the solids and liquids were separated for analysis. In the earliest experiments (Trials 1 and 2), the reactors were allowed to cool over night before they were opened. The extended cooling time gave rise to concerns that dissolved solids might be re-precipitating.

To eliminate the concern of possible re-precipitation, the apparatus was modified slightly for Trials 3 through 5. An additional valve was added at the bottom of the reactor to allow fluids to be extracted. A length of coiled tubing was attached to the outlet of the bottom valve and the tubing coil was placed in a water bath. At the end of the experiments, the bottom valve was opened and the condensed vapor was collected and then diluted to prevent re-precipitation.

Significant leakage of water was noted in some trials, especially in the case of Trial 4 in which the reactor was completely dry at the end of the experimental run. At

Table 3.15. Experiment details of Trials 1 through 5.

Trial	Solids	Liquid	Duration
1	sintered bauxite	Deionized water	~ 1 month
2	sintered bauxite	Deionized water	~ 2 months
3	sintered bauxite and crushed granite	Deionized water	10 weeks
4	sintered bauxite and crushed granite	Deionized water spiked with silica	11 weeks
5	sintered bauxite and crushed granite	Deionized water spiked with silica	11 weeks

least some leakage is suspected in each of the trials conducted in the stainless steel fixed bed reactors. Effects of water leakage will be discussed later.

3.2.2.2 Trials A through I

Trials A through I used an improved, leak-free apparatus. Experiments were all conducted at 230 °C in the presence of geothermal water from Raft River geothermal well RRG-1.

3.2.2.2.1 Apparatus. To prevent leakage of water in further experiments, the apparatus was significantly altered. In Trials A through I, sealed quartz-glass ampoules similar to those described by Adams at al. (1986) served as the reaction vessels. Figure 3.6 is a schematic drawing of the ampoules.

Because of the relatively high vapor pressure of water at test temperatures and the relatively low tensile strength of the quartz-glass ampoules, the ampoules were placed inside pressure vessels designed for use at elevated temperature and pressure. The pressure vessels selected for use in the experiments were manufactured by Autoclave Engineers, a division of Snap-tite, Inc. The Autoclave Engineers equipment was selected because a leak-free seal had to be maintained at elevated temperature and pressure for extended periods of time. The first Autoclave Engineers vessel was constructed from a 10-in coned and threaded nipple (one-in outside diameter)

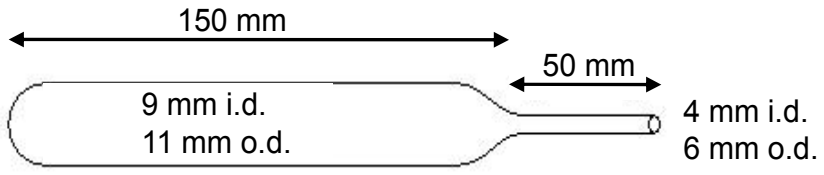

Figure 3.6. Schematic drawing of quartz-glass ampoules.

and end caps (Figure 3.7). The end caps are stamped for maximum allowable working pressure of 20,000 psi at room temperature. The tubing is rated at up to 15,000 psi at 100 °F.

The second AE vessel is a single-ended Kuentzel closure vessel (Figure 3.8). The vessel was manufactured and certified by Autoclave Engineers and is stamped with a maximum allowable working pressure of 11,000 psi at 300 °F. The vessel has a one-inch inside diameter and inner length of eight inches with a total volume of 103 mL. Appendix B contains a technical drawing of the reactor.

The system was designed so that three ampoules could fit in the Kuntzel closure vessel and an additional one ampoule could fit in the smaller vessel. This allowed up to four trials to be conducted simultaneously.

3.2.2.2.2 Method. Solids – proppant or proppant and granite – were carefully measured out on an analytical scale. In the trials in which proppant and granite were used, the solids were mixed by hand to obtain an approximately even distribution of granite and proppant to maximize proppant-granite contact thus allowing for possible interactions to occur during the trials. The solids were then loaded into the ampoules. A small amount of water was then added to the ampoules using a syringe and tubing.

Figure 3.7. Pressure vessel constructed of Autoclave Engineers coned and threaded nipple and end caps.

Figure 3.8. Autoclave Engineers Kuntzel closure pressure vessel.

Water was added slowly, displacing air in the pore spaces between solid grains. While enough water was added to completely cover the solids, sufficient free volume was also maintained to allow for the thermal expansion of the water during the trials.

The ampoules were then sparged with argon gas for approximately one-half hour. The sparging was conducted to de-aerate the ampoules to prevent oxidization reactions that might occur in the presence of oxygen. Such oxidization reactions were considered unrepresentative of reactions expected to take place deep within a geothermal reservoir.

After sparging, the ampoules were hermetically sealed using an oxy-combustion methane flame. The sealed ampoules were then weighed. Figure 3.9 shows the sealed quartz-glass ampoules filled with proppant, granite and water.

The sealed ampoules were loaded into the two Autoclave Engineers pressure vessels. A small amount of tap water was added to the pressure vessels. The water was added to balance the pressure that would be observed in the ampoules during the experiments. The threads, sealing surfaces and bearing surfaces were coated with Jet-Lube, a copper thread-seal and anti-seize compound, to improve the seal quality and prevent mated parts from seizing together during the experiments. A torque wrench was used to apply the manufacturer-recommended torque to the caps and plugs of the vessels. The vessels were placed inside an oven and the oven temperature was set. Trials A through I were all conducted at 230 °C and used geothermal water from Raft River well RRG-1. Table 3.16 gives the details of the individual trials.

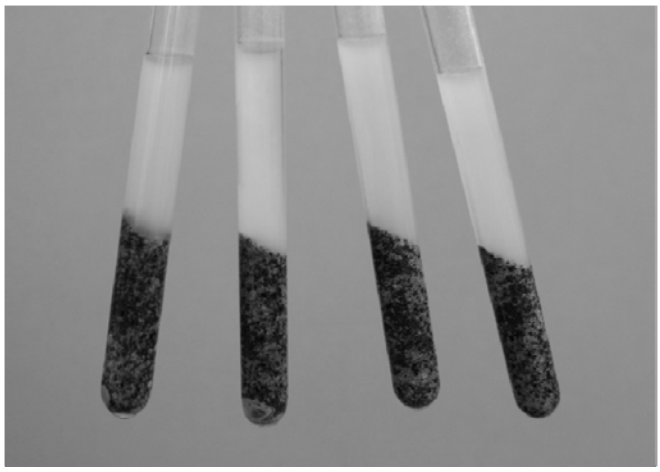

Figure 3.9. Sealed ampoules. Proppant and granite were added to the ampoules. Water was then slowly added allowing it to flow into pore spaces. The ampoules were then sparged with argon gas and hermetically sealed.

Table 3.16. Experiment details. Trials A through I.

Trial	Solids	Duration	Notes
A	sintered bauxite	5 weeks	
B	sintered bauxite and crushed granite	4 weeks	Solids rinsed with DI water after experiment.
C	sintered bauxite and crushed granite	4 weeks	
D	quartz sand and crushed granite	4 weeks	Solids rinsed with DI water after experiment.
E	quartz sand and crushed granite	4 weeks	
F	resin-coated bauxite and crushed granite	4 weeks	Ampoule prepared approximately two months before the experiment. Solids rinsed with DI water after experiment.
G	resin-coated bauxite and crushed granite	4 weeks	Ampoule prepared approximately two months before experiment.
H	resin-coated bauxite and crushed granite	4 weeks	Solids rinsed with DI water after experiment.
I	resin-coated bauxite and crushed granite	4 weeks	

Following the cooking period, the pressure vessels were removed from the oven and allowed to cool slowly over approximately three hours. The vessels were then opened and the ampoules removed. The ampoules were weighed to verify that no leakage had occurred. The ampoules were opened by scoring and breaking their necks. Water was extracted using a syringe and tubing and placed in a test tube. A 1-mL aliquot was then taken and diluted 10-to-1 with deionized or Milli-Q water. In some cases (see Table 3.16) the solids were then rinsed with deionized water to flush away any dissolved solids that might have otherwise precipitated at room temperature or as the solids dried. The solids were then oven dried.

3.2.2.3 Analytical Methods

Solids and liquids were analyzed to determine the effects of exposure to geothermal conditions on proppants. In particular, analyses were performed in order to identify evidence of dissolution of proppant and/or precipitation or crystallization of dissolved solids.

3.2.2.3.1 Solids. Solids were analyzed using SEM and EDS. SEM photomicrographs were examined for evidence of textural changes such as dissolution textures or precipitation of dissolved solids or crystal growth. EDS spectra were used to obtain the chemical composition of proppant and granite grain surfaces. The chemical compositions as well as SEM photomicrographs were used to infer mineral identities.

3.2.2.3.2 Water chemistry. Chemical analyses of samples from early experiments (Trials 1 through 5 and Trial A) were performed using inductively-coupled plasma mass spectroscopy (ICP-MS). However, the method failed to accurately determine the concentration of anions. Chemical analyses of samples from later experiments (Trials A through I) were performed by Thermochem, Inc. The results of these water chemistry analyses were used to make inferences about which elements or mineral species had dissolved during the experiments. Silica concentrations were used in geothermometry methods as a check of validity.

3.2.3 Crush Tests

Crush tests were designed to evaluate the strength of fresh and used proppant. Only two of the three proppants – 30/60 sintered bauxite and 20/40 resin-coated bauxite – were crush tested. Tests were conducted using a triaxial load frame.

3.2.3.1 Experimental Methods

The International Organization for Standardization (ISO) has published a specification for tests of proppant strength (ISO 13503-2:2006) that replaces earlier specifications published by the American Petroleum Institute. Due to the small amounts of used proppant available for the tests it was impossible to adhere completely to the ISO specification. However, the method of testing used in the present study does follow the basic methodology laid out by the ISO. Because the ISO standard was not followed, results of crush tests included herein should not be compared with tests conducted according to the ISO standard. However, the tests conducted in the present work were all conducted using the same procedure and apparatus. The tests are therefore internally consistent and results of these tests may be compared with one another.

3.2.3.1.1 Apparatus. A crush test cell similar to that specified by the ISO was designed and constructed. The test cell is composed of five parts: a base plug and tube, which form the test cell, a rod or piston, which applies the crushing force and two carbide inserts, which serve as hardened faces. Carbide is extremely hard and was used for the contact surfaces to prevent proppant embedment. The test cell was designed so that the proppant pack would be crushed between the two carbide inserts. The base plug, tube and rod were constructed of annealed tool steel. Figures 3.10 and 3.11 are a drawing and photograph of the test cell. Technical drawings may be found in Appendix B.

3.2.3.1.2 Method. The test cell was assembled by placing the larger carbide insert in the bottom of the test cell tube and screwing the base plug into place. The base plug holds the carbide insert in place and was hand tightened. Proppant samples were weighed and placed in the crush test cell. The second carbide insert was then placed in

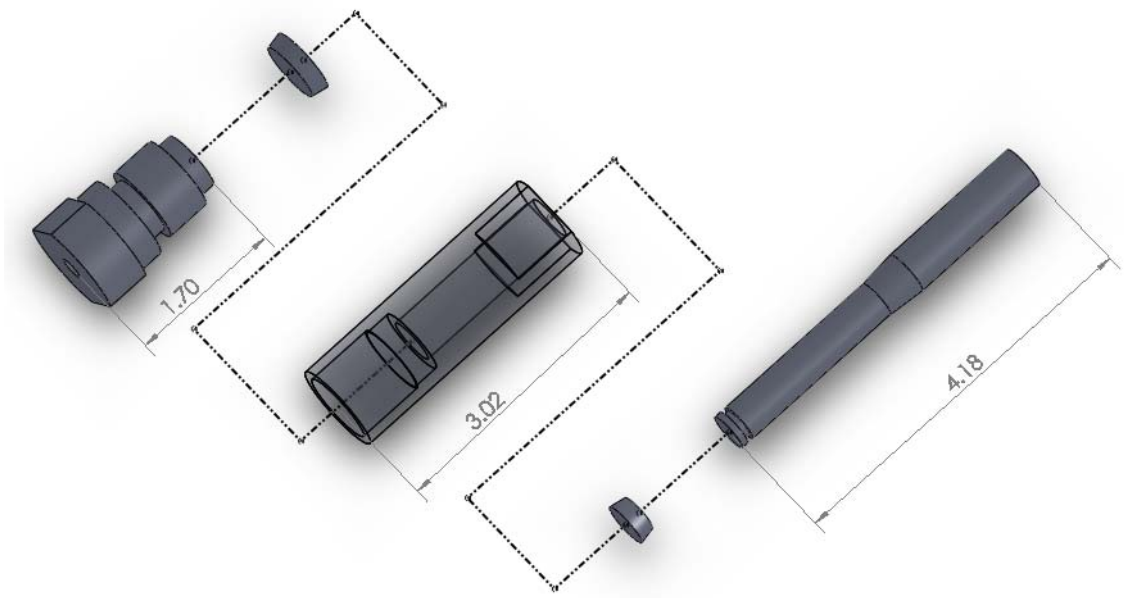

Figure 3.10. Exploded view of proppant crush test cell. The base plug screws into the tube and holds the lower carbide insert in place. Crushing force applied by the load frame is transmitted to the proppant pack via the rod and upper carbide insert. Size measurements, in inches, are provided for scale reference.

the test cell on top of the proppant pack. The rod was then put in place in the test cell on top of the upper carbide insert. Linear variable differential transformers (LVDTs) were then fitted onto the test cell. The thickness of the proppant pack was then measured. The whole assembly was then loaded into a TerraTek triaxial load frame. While the frame is capable of conducting triaxial tests using a confining fluid, the proppant experiments called for uniaxial loading only. The load frame is capable of applying axial load of up to 100,000 lb_f.

The triaxial machine is computer-controlled and a test program was written to ensure that tests were conducted consistently. Load and LVDT position were recorded once per second. Stress (calculated from the load) and strain (calculated from the LVDTs and proppant pack thickness) were also recorded once per second. Samples were loaded

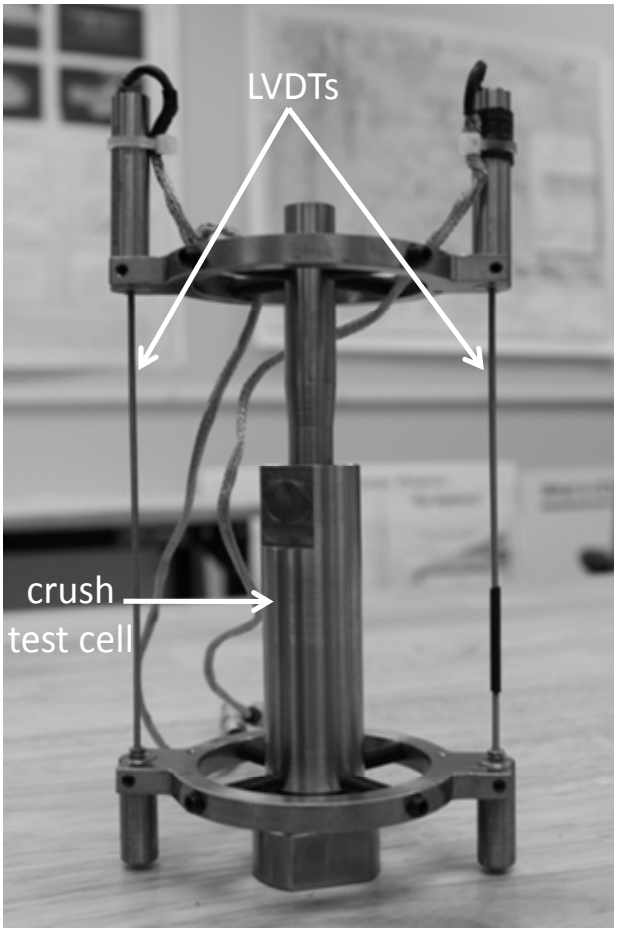

Figure 3.11. Proppant crush test cell. The test cell is constructed of annealed tool steel. Carbide inserts are used as the loading faces. This image shows the test cell. Two linear variable displacement transformers (the narrow shafts on either side of the test cell) are also pictured. The linear variable displacement transformers (LVDTs) are used to measure the deformation of the proppant pack.

to 200 psi under computer control and the position of the load piston was held constant while the LVDT and load signals stabilized as the proppant pack compressed. The LVDT signals were zeroed at their current positions and the test then proceeded under computer control. This procedure was followed to ensure the triaxial machine load cylinder was in contact with the crush test cell. By so doing a uniform datum was established that permitted comparison of results of the individual tests.

The crush tests consisted of two loading cycles. In the first cycle, the stress was steadily increased to 15,000 psi at a constant rate of 2,000 psi/min. When the maximum stress of 15,000 psi was reached, the stress was then steadily decreased at a rate of 2,000 psi/min until the cell was unloaded. The second loading cycle immediately followed and the stress was again steadily increased to 15,000 psi where it was held constant for two minutes. At the end of the 2-min hold time, the stress was steadily decreased at a rate of 2,000 psi/min. When the test cell was unloaded, the proppant was removed and collected for later analysis. The testing program is similar to that specified by the ISO, which calls for only one load cycle at a rate of 2,000 psi/min. A maximum stress is not specified though suggestions are given for various proppant types. The 2-min hold at maximum stress is also specified by the ISO.

3.2.3.2 Analytical Methods

The resistance of proppant to crushing was determined by analyzing the data collected during the test (stress, strain and time) and by a sieve analysis of the proppant after crushing. Several metrics of proppant crushability were used as a means of comparison between proppant types and between used and fresh samples. These metrics included Young's moduli of the first and second loading cycles, creep rate and fines generation, each of which will be defined and discussed presently.

3.2.3.2.1 Moduli and creep. Real-time data collected during the crush tests were analyzed and three metrics were derived for proppant strength comparison. Young's modulus from the first and second loading cycles were calculated and represent the first and second metrics for comparison. Young's modulus, E, is defined as

$$E = \frac{\sigma}{\varepsilon} \tag{3.1}$$

where σ is the axial stress and ε is the axial strain. Young's modulus can be found as the slope of the linear portion of a stress-strain curve. Specifically, the loading Young's moduli (as opposed to unloading moduli) were calculated. The third metric for comparison is creep. Creep is the axial strain that is measured while a constant stress is applied to a solid. In the proppant crush experiments, creep was measured during the two-minute hold at the maximum stress. When creep strain is plotted over the log of time, the creep is linear. The creep rate is defined as the slope of the strain over time line on the semilog plot, measuring time from the moment the load was held constant.

3.2.3.2.2 Sieve. The crushed proppant was sieved using the smallest mesh size specified for the particular proppant. For example, crushed 30/60 proppant was sieved through a number 60 sieve. Fines were defined as any particles that passed through the sieve. The mass of fines generated during the crush test was then divided by the total mass of the sample. The result is defined herein as the crush fraction. The crush fraction provided the fourth metric for comparison of proppant strength between samples.

3.2.3.2.3 Statistics. Several duplicates of fresh proppant were crush tested and analyzed by sieving and using the four metrics just defined. Results of crush tests on samples of fresh and used proppant of the two proppant types (sintered bauxite and resin-coated bauxite) were compared and statistical tests of significance were performed. The individual samples of used proppant were small enough to preclude duplicate tests of each sample.

3.3 Results

The present work combined two distinct but closely related experiments. The first round of experiments dealt with the chemical stability of proppants under geothermal conditions. The second round of experiments assessed the effects of exposure to geothermal conditions on proppant crushability. Because the experiments are distinct from one another and to improve clarity, the results of the two experiments will be discussed separately.

3.3.1 Results of Tests of Chemical Stability

The results of the tests of chemical stability were significantly affected by the apparatus in which the particular trials were conducted. Because the two sets of results are so different, they will be considered separately.

The first series of trials were conducted in stainless steel packed bed batch reactors that, in several cases, failed to seal completely. Slow leakage of water led to super-saturation of dissolved solids that then precipitated on solid surfaces. These early experiments provided some of the most interesting results and highlight the effects of super-saturation of dissolved species. Conditions of super-saturation could result from boiling within a geothermal reservoir or from significant cooling.

The second series of trials were conducted in a different apparatus that had been designed to be leak-free even at elevated temperatures and pressures. Reactants were hermetically sealed in quartz-glass ampoules. The hermetic seal prevented any water loss.

3.3.1.1 Trials 1 Through 5

Early experiments (Trials 1 through 5) were conducted in stainless steel packed bed batch reactors. In several of the trials, water is known to have leaked from the reactors; however, it was impossible to quantify how much water had escaped. In some cases, leakage was obvious; When the Trial 4 reactor was opened, for example, it was completely dry.

3.3.1.1.1 Water loss. Super-saturation of solids dissolved in reactor fluids due to water leakage led to precipitation of amorphous silica and crystal growth of new mineral phases. Leakage in Trial 4 was so significant that the inside of the reactor was completely dry at the end of the trial. Cursory examination of the remaining solids from Trial 4 seemed to indicate little change had occurred, possibly because water escaped so quickly that there was no time for significant dissolution or precipitation to occur. Trial 4 has therefore been classified as a failed experiment and will not be discussed further.

3.3.1.1.2 Precipitation. An amorphous aluminosilicate coating was observed on the surfaces of proppant and granite grains from Trials 2, 3 and 5. The coating is ubiquitous and of varying composition and morphology, ranging from smooth, approaching glass-like (Figure 3.12) to rough, having a cauliflower-like texture (Figure 3.13). In several cases, grains of proppant and granite became cemented together and in at least two instances, solids became strongly cemented to the walls of the reactor. Aggressive attempts to mechanically remove the solids from the walls of the reactors were largely unsuccessful. The amorphous coating was observed to be the cement binding proppant and granite grains together (Figure 3.14) and is also suspected to be the cement that bound solids to the walls of the reactors.

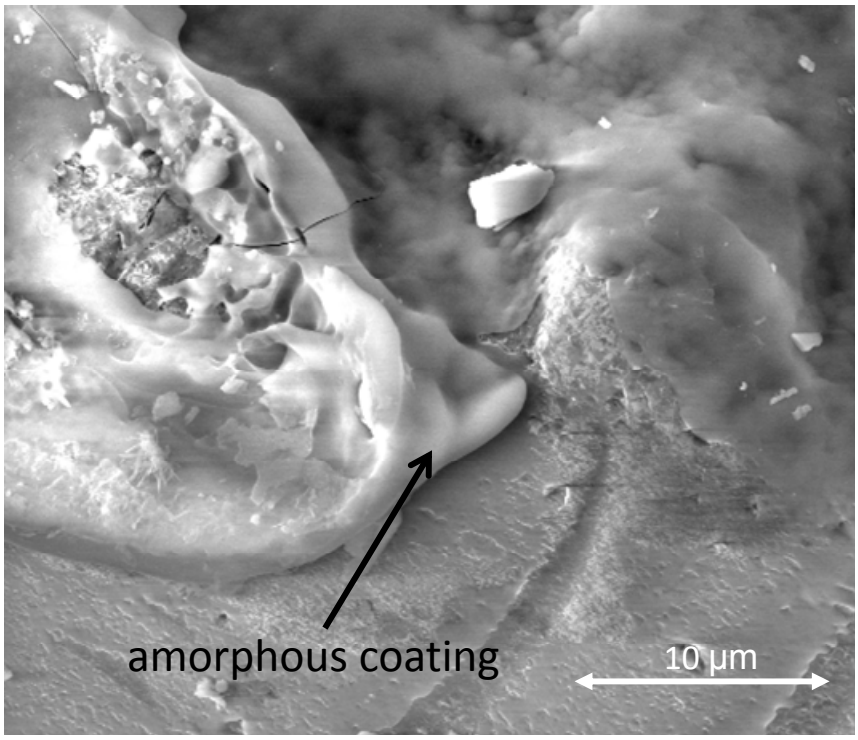

Figure 3.12. Smooth amorphous coating on granite particle from Trial 3.

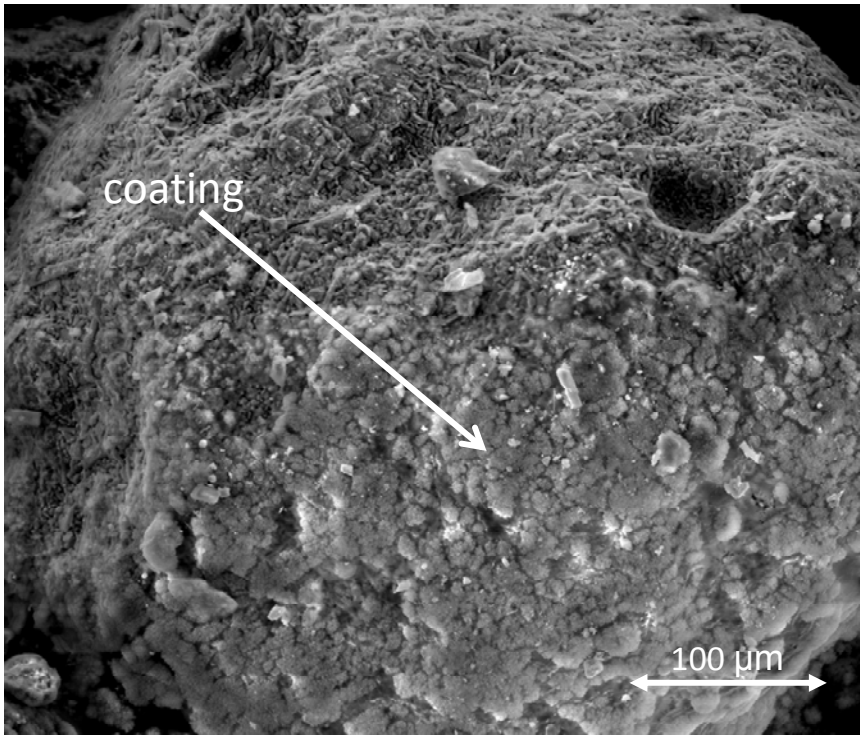

Figure 3.13. Coating with rough texture.

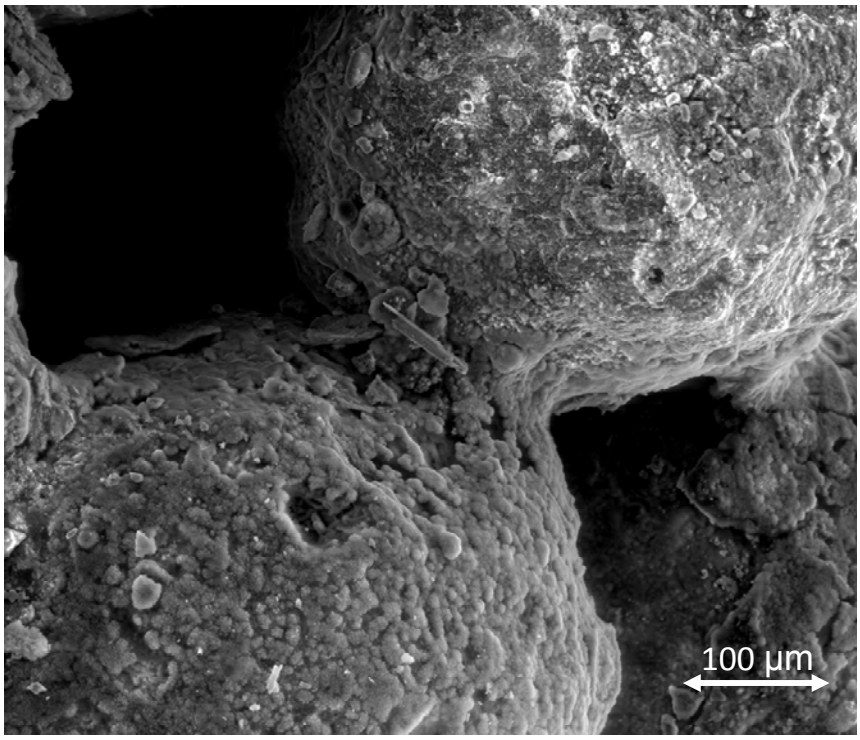

Figure 3.14. Amorphous cement binding two sintered bauxite proppant grains together.

3.3.1.1.3 Crystal growth. In addition to the precipitation of the amorphous silica coating, crystal growth was also observed on the surfaces of proppant and granite grains from Trials 3 and 5. Attempts were made to identify the new mineral phases based on their compositions and morphologies. Vermiculite (?), opal CT (?), wairakite (?), and erionite (Figures 3.15 through 3.17) crystal growth have all been tentatively identified on solid surfaces.

3.3.1.1.4 Clay minerals. Aggregates of grey clay minerals were observed in Trial 1 near the bottom of the reactor (Figure 3.18). X-ray diffraction analysis of a sample of the clay indicates the presence of chlorite and traces of illite. Similar grey clay minerals were observed in Trial 2 but were dispersed throughout the proppant pack.

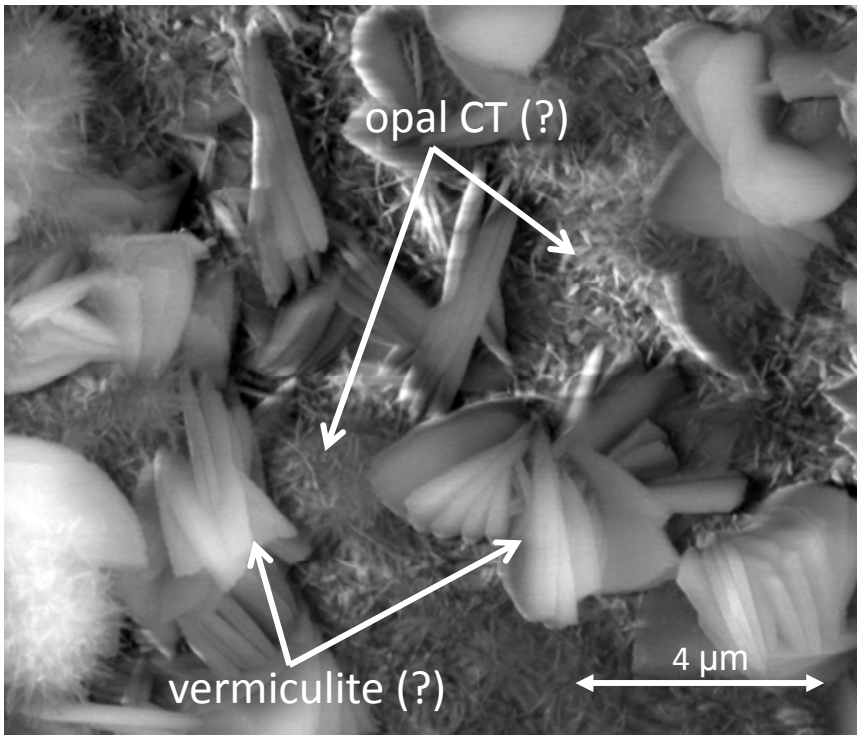

Figure 3.15. Books of vermiculite(?) and fine needles of opal CT(?) from Trial 3

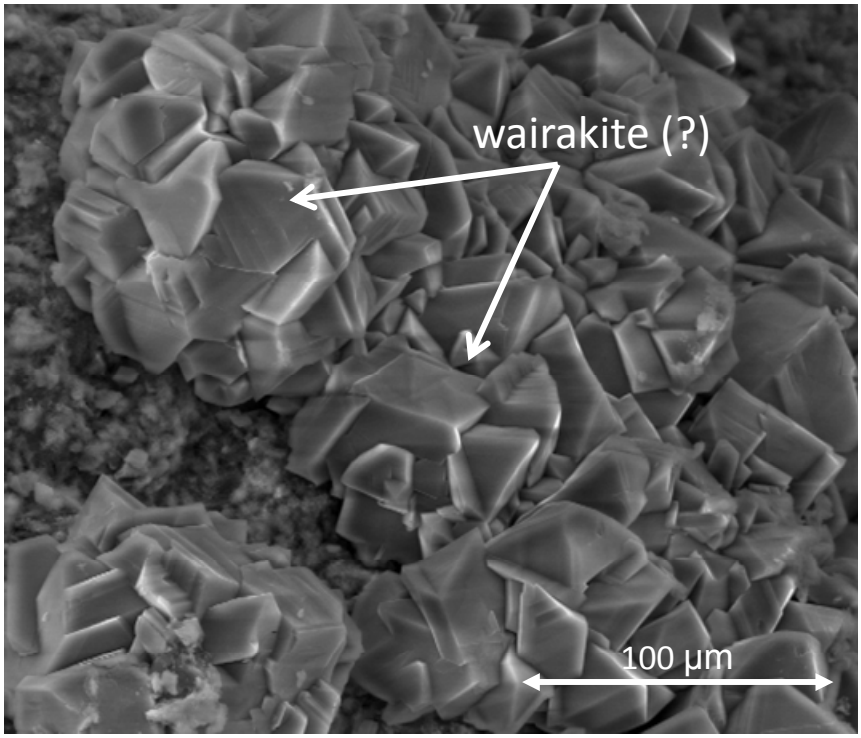

Figure 3.16. Wairakite(?) crystal growth on surface of sintered bauxite proppant from Trial 3

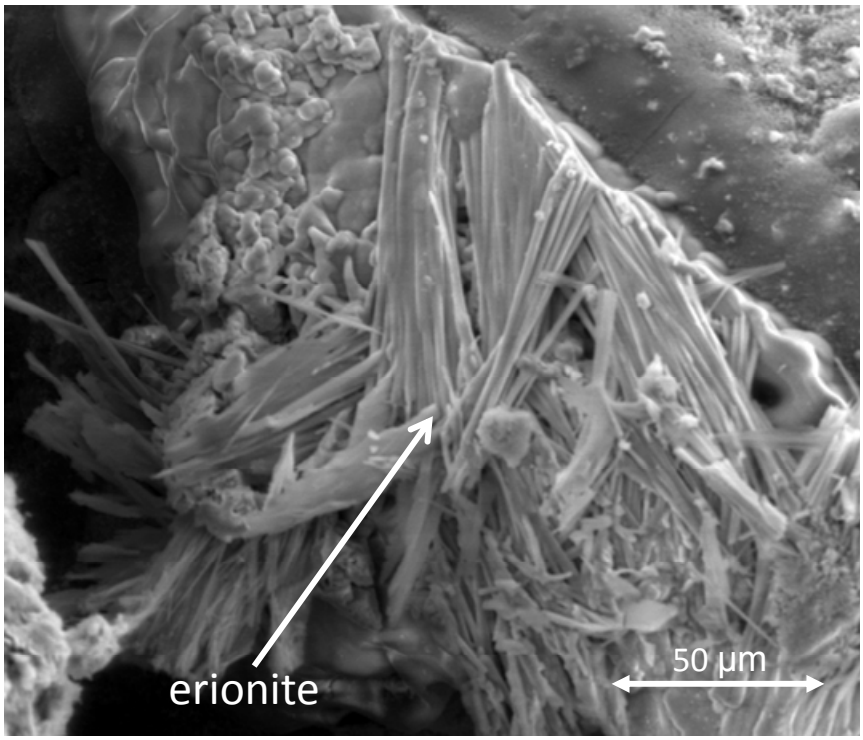

Figure 3.17. Acicular erionite crystals from Trial 5

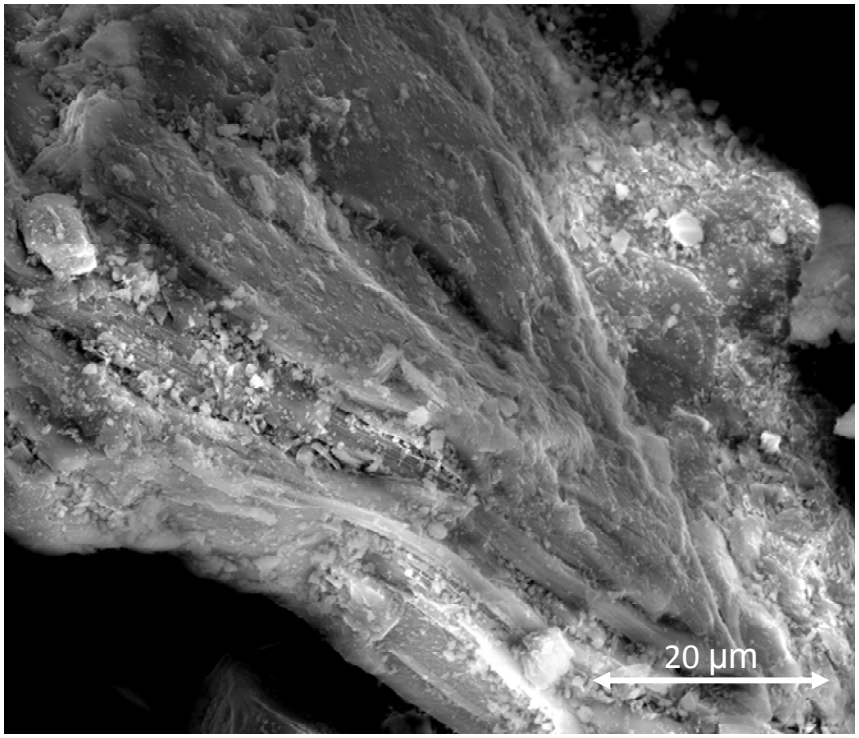

Figure 3.18. Sheet silicate, probably chlorite, from Trial 1.

3.3.1.1.5 Dissolution. Only limited evidence of dissolution (in the form of dissolution textures) was found in the SEM images of the proppant from Trial 1 (Figure 3.19). However, further evidence of dissolution is seen in the abundance of precipitates and crystals that formed in the experiments. This is especially true for Trials 1 and 2 that were conducted using deionized water; the only source of dissolved solids from which precipitates could form was the solids originally loaded into the reactors. That dissolution textures were not more frequently observed may be due to the large amount of precipitation and recrystalization that would have frequently covered any such textures.

3.3.1.2 Trials A Through I

Trials A through I were conducted in hermetically sealed glass ampoules. No water escaped during the experiments leading to results quite different than were obtained from earlier experiments conducted in the fixed bed reactors that leaked.

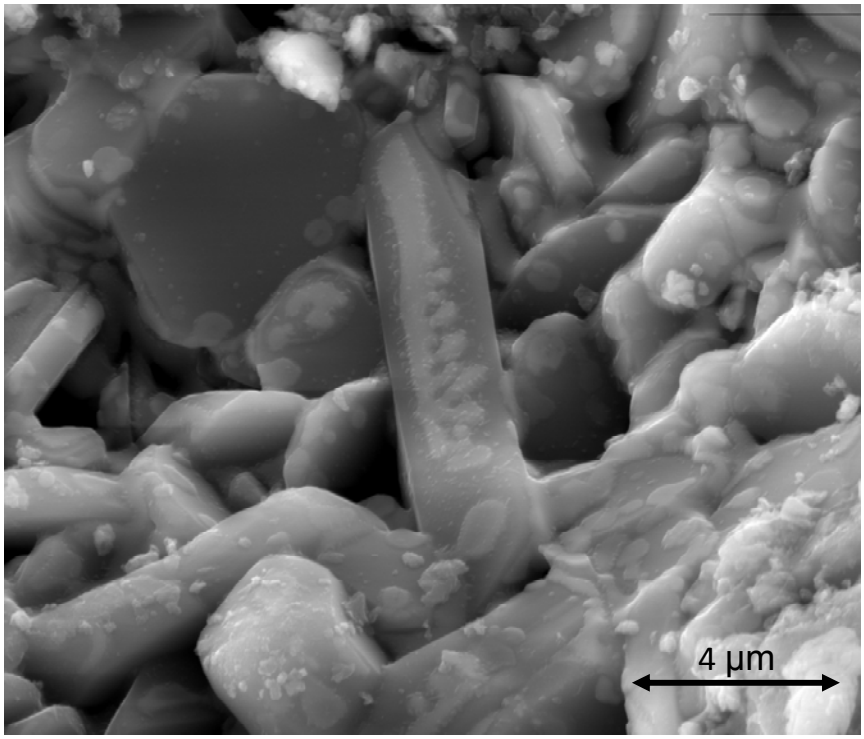

Figure 3.19. Dissolution texture on sintered bauxite proppant from Trial 1

3.3.1.2.1 Dissolution. Photomicrographs of sintered bauxite proppant from Trial B indicate that dissolution occurred (Figure 3.20). Similar dissolution textures were also observed on bauxite proppant surfaces from Trials A and C (Figure 3.21). Evidence of dissolution of quartz sand proppant was not as obvious as it was in the case of the sintered bauxite proppant; however, some possible dissolution textures were observed (Figure 3.22).

The dissolution textures that were commonly observed on the surfaces of sintered bauxite proppant (Figure 3.20) were not observed on the surfaces of resin-coated bauxite grains. A side-by-side comparison of fresh and used resin-coated bauxite proppant (Figure 3.23) shows that very little textural change occurred. Further, a side-by-side comparison of used resin-coated and sintered bauxite proppants (Figure 3.24) on approximately the same scale highlights the absence of dissolution textures on resin-coated proppant grains.

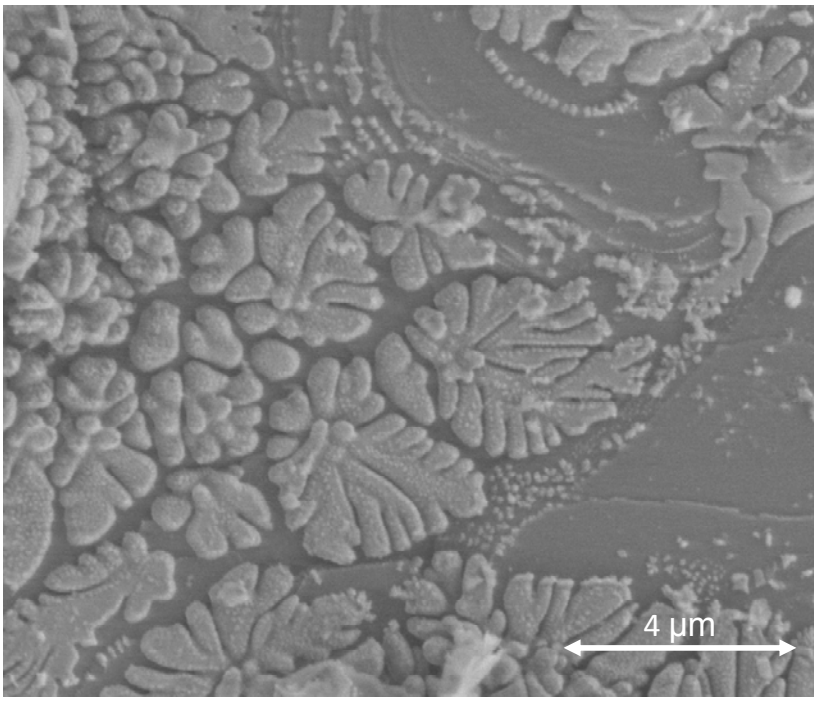

Figure 3.20. Dissolution texture on sintered bauxite proppant from Trial B.

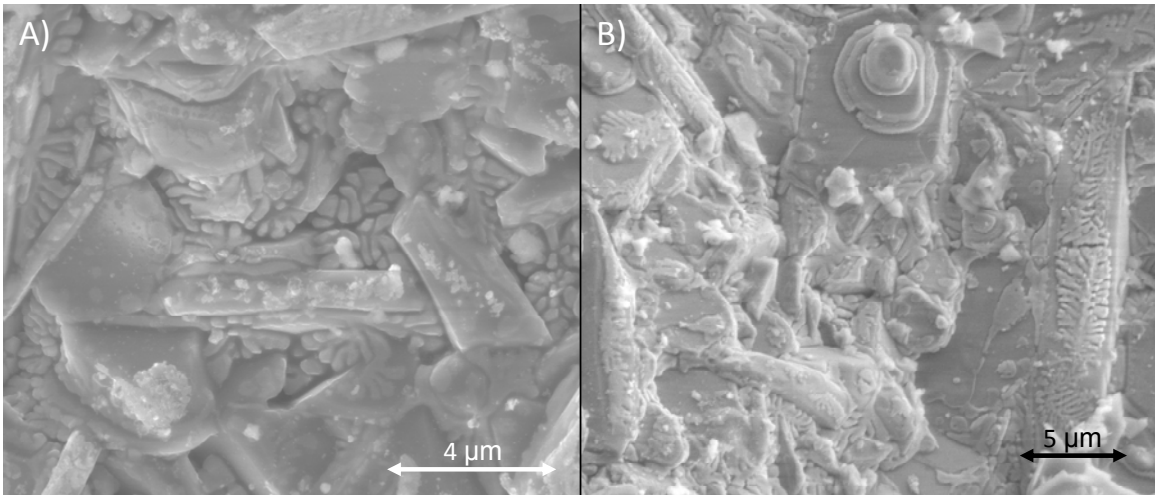

Figure 3.21. Dissolution textures were also observed on proppant surfaces from Trials A (left) and C (right).

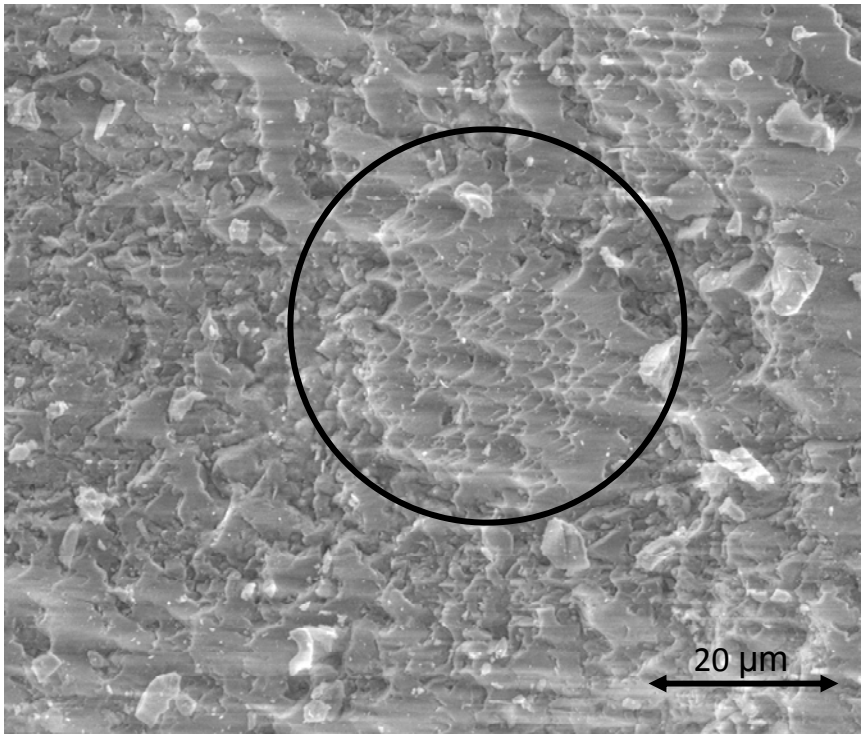

Figure 3.22. Possible dissolution textures on quartz sand proppant surface.

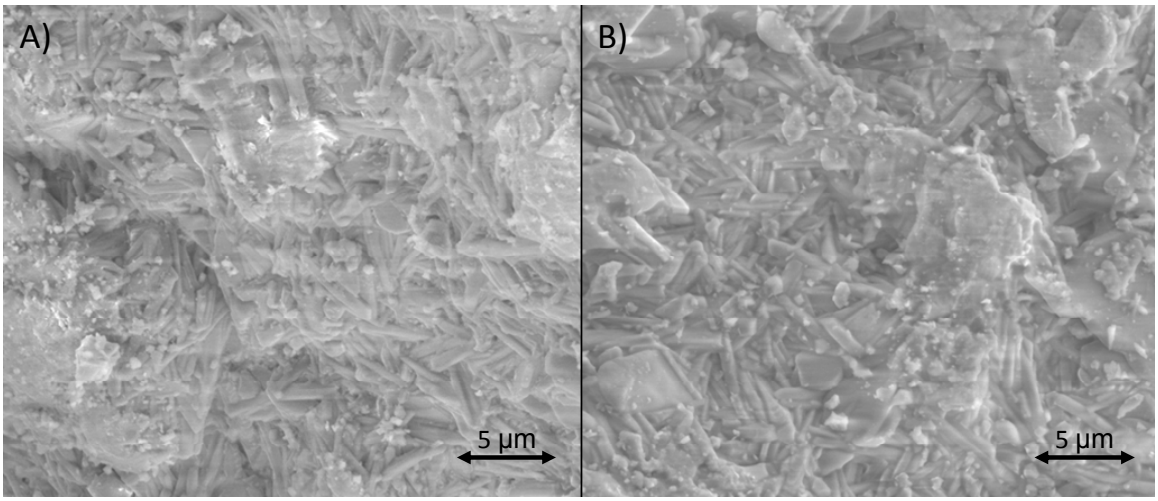

Figure 3.23. Comparison of fresh (A) and used (B) resin-coated bauxite proppant. The proppant surface appears to be unchanged from its fresh state.

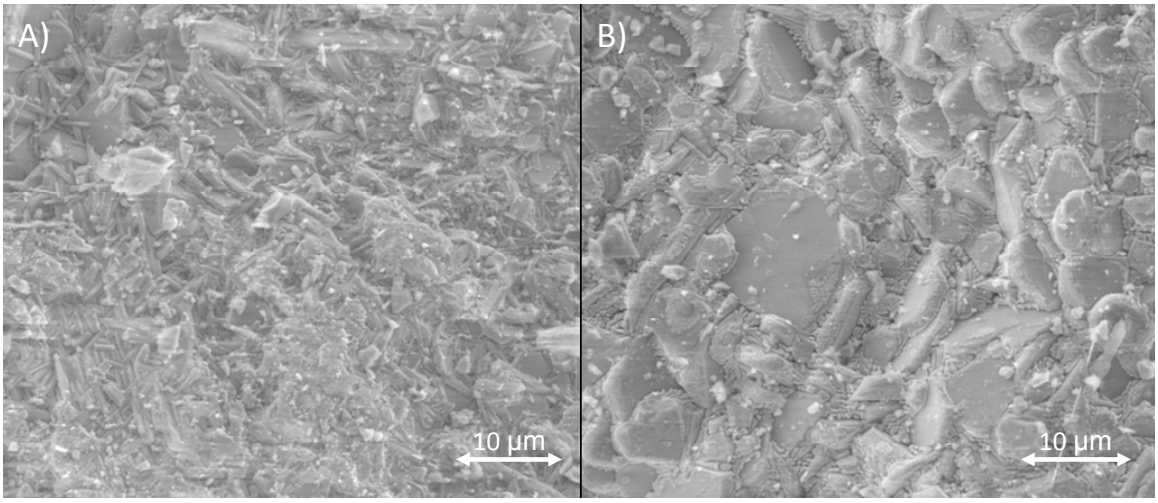

Figure 3.24. Comparison of resin-coated proppant (A) and sintered bauxite proppant (B). The dissolution textures that were characteristic of the used sintered bauxite proppant were not observed in resin-coated proppant.

While the abundance of dissolution textures common to sintered bauxite proppant were not observed in resin-coated proppant, there was some other evidence of possible alteration observed on resin-coated proppant surfaces where entire crystals seem to have been displaced (Figure 3.25). Additionally, evidence of zeolite (?) crystal growth was observed in samples from Ampoule H (Figure 2.36).

Practical considerations dictated that only a very small fraction of the total proppant surface area could actually be imaged using SEM. The small sample size precludes stating that the resin-coated proppant is unaffected by exposure to geothermal conditions. Instead, all that can be said is that no obvious signs of dissolution were observed.

3.3.1.2.2 Water chemistry. Water extracted from the ampoules of Trials A through I was sent to Thermochem, Inc. for analysis. Water composition data are given in Table 3.17. The results of the water analyses clearly indicate that dissolution of a silica phase

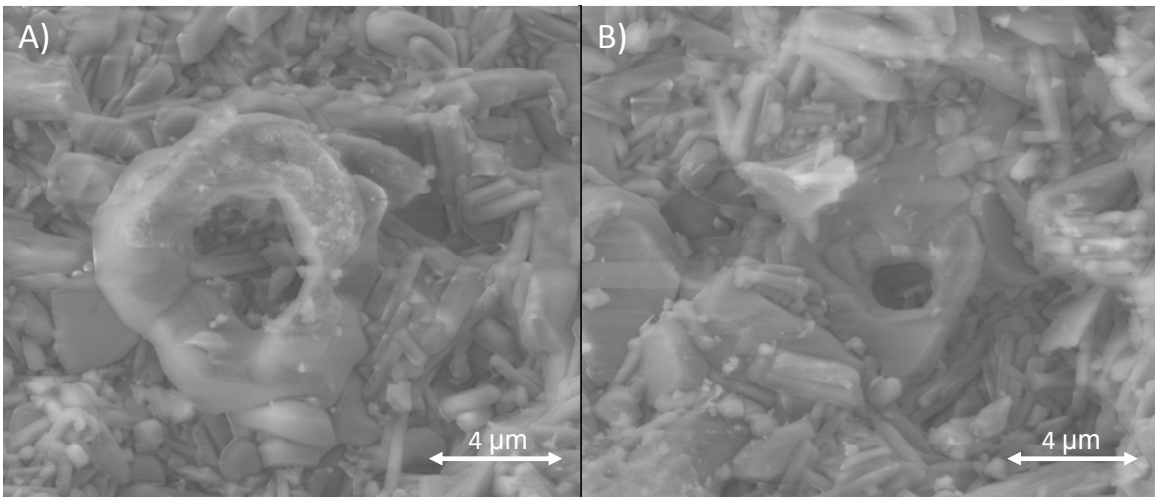

Figure 3.25. Possible evidence of alteration due to simulated geothermal conditions where crystals appear to have been displaced.

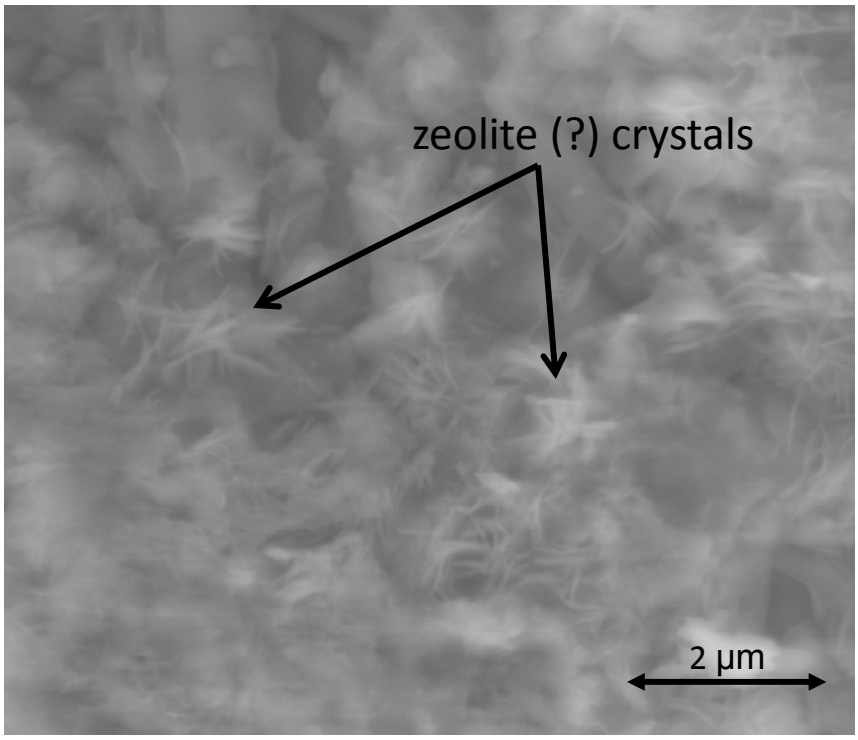

Figure 3.26. Zeolite (?) crystal growth on resin-coated proppant surface.

occurred in Trials A through C (sintered bauxite proppant and granite), Trials D and E (quartz sand proppant and granite) and Trials F through I (resin-coated bauxite proppant and granite) though further analysis shows that the source of silica may have been the glass ampoules rather than the proppant or granite grains (see *Discussion* section). Water analyses also indicate that some dissolution of calcium-containing plagioclase (anorthite) in the crushed granite occurred. Elevated sulfate concentration levels were also observed.

3.3.2 Results of Crush Tests

Crush tests were conducted in order to quantify the degree to which proppants were weakened by exposure to geothermal fluid at elevated temperature. Fresh and used proppants were tested and four metrics were identified as points for comparison between fresh and used proppants.

Table 3.17. Water chemistry of Raft River geothermal brine and water extracted from Trials A through I. Experiments were all conducted using geothermal water and at 230 °C.

		Trial									RRG-1 Water
		A	B	C	D	E	F	G	H	I	
		Sintered bauxite	Sintered bauxite and crushed granite		Quartz sand and crushed granite		Resin-coated bauxite and crushed granite				–
		5 weeks	4 weeks				4 weeks[a]		4 weeks		–
Dissolved Species – mg/kg	Na	558	519	503	653	536	540	546	571	577	547
	K	40.2	38.2	42	44.7	35.8	38.6	39.1	39.2	40.4	36.5
	Ca	46	181	130	125	103	110	121	119	94.1	59
	Cl	867	933	929	1110	912	942	960	985	976	942
	SiO_2	674	545	649	825	678	629	695	617	709	129
	Sulfate	75.7	99.1	75.9	87.2	72.8	77.0	78.9	82.6	48.0	58.3

a) Ampoules sealed approximately two months before experiment

3.3.2.1 Data Reduction

The first three metrics used in comparing proppants – Young's modulus from load cycle one, Young's modulus from load cycle two, and creep rate – were extracted from data collected during the crush tests. Figures 3.27 and 3.28 show data from one crush test performed on sintered bauxite proppant and are included to demonstrate how the modulus and creep are extracted from the pertinent plots.

In addition to the three metrics derived from the data obtained during the crush tests, the crushed samples were sieved. The ratio of the mass of fines generated during crushing to the mass of the total sample is defined as the crush fraction and provides the fourth metric for comparison of used proppant to fresh proppant.

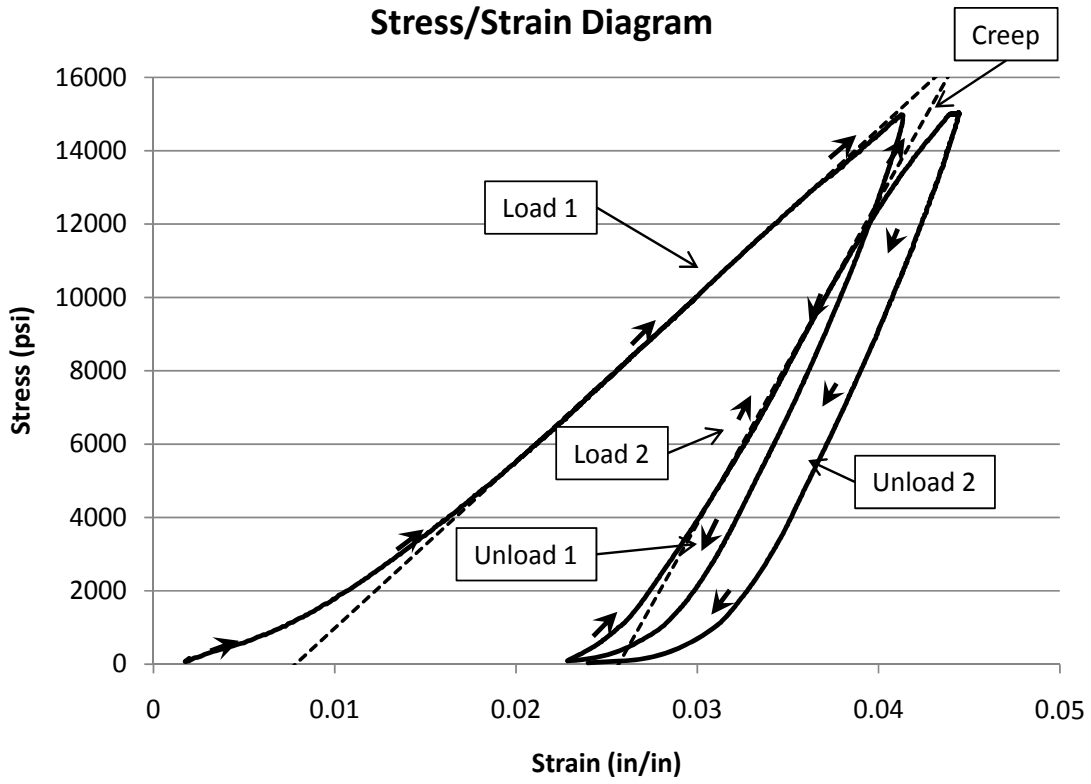

Figure 3.27. Stress-strain diagram with linear-section tangent lines. Proppant samples were loaded and unloaded twice. The slopes of the tangent lines represent Young's moduli for the two loading cycles. Young's moduli from the first and second loading cycles provide the first two metrics for comparing proppants.

3.3.2.2 Proppant Compliance

Crush tests were conducted on fresh samples of sintered bauxite and resin-coated bauxite proppants. Six 2.0-g samples of fresh sintered bauxite and eight 2.0-g samples of fresh resin-coated bauxite were crushed to establish baseline data for the fresh proppant. Table 3.18 shows the average values of the four metrics for both proppant types. Additionally, six 1.50-g samples of fresh resin-coated proppant were also crush tested. This was done because during the course of the crush tests, a strong dependence of modulus and creep on sample size was observed. Samples of used resin-coated proppant were small (less than 2 g); Crush tests of 1.50-g samples of fresh resin-coated proppant

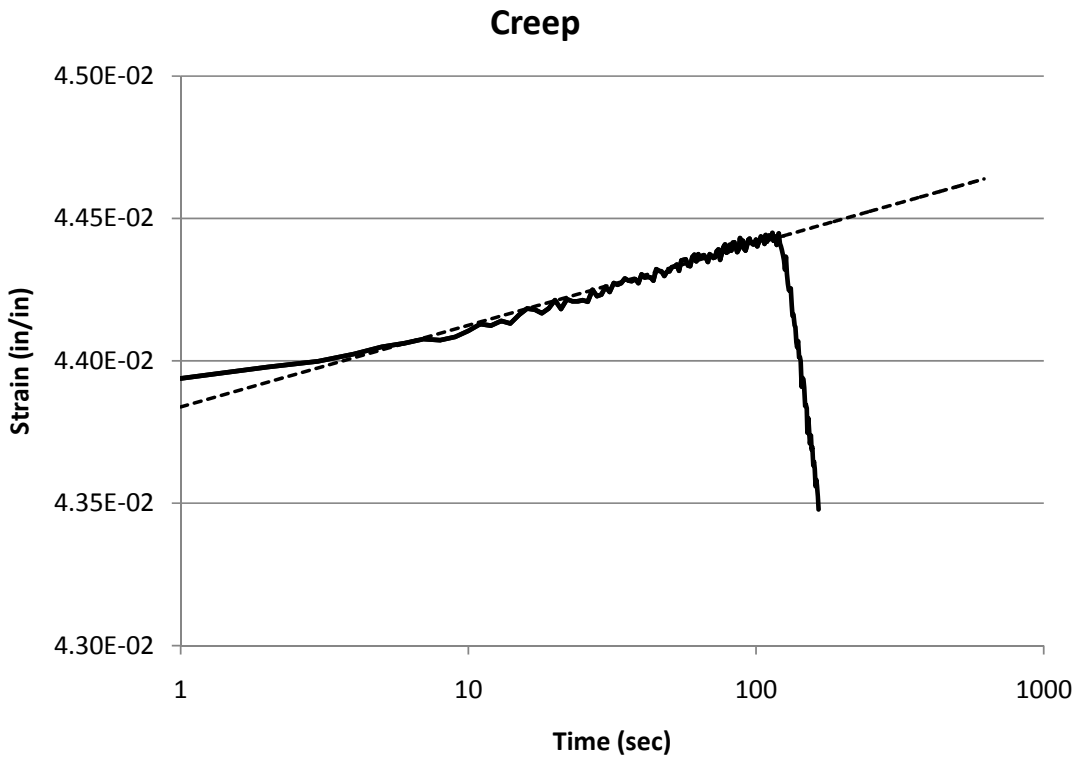

Figure 3.28. Strain over time. Stress was held at a constant value while strain was recorded over time, measured in seconds from the moment load was held constant. The creep is taken as the slope of the strain over the log of hold time and is the third metric used for comparing proppants.

Table 3.18. Results of crush tests on samples of fresh sintered bauxite and resin-coated bauxite with confidence intervals at the 95% confidence level.

	Load 1 Modulus ($\cdot 10^3$ psi)	Load 2 Modulus ($\cdot 10^3$ psi)	Creep Rate ($\cdot 10^{-5}$ 1/ln sec)	Crush Fraction ($\cdot 10^{-3}$ g/g)
Sintered Bauxite (2.0 g)	440 ± 39	892 ± 26	14.9 ± 2.3	13.8 ± 7.4
Resin-coated Bauxite (2.0 g)	377 ± 13	905 ± 19	43.0 ± 4.6	93.9 ± 7.4
Resin-coated Bauxite (1.50 g)	342 ± 12	748 ± 16	46.5 ± 9.7	104 ± 10

were conducted to provide a baseline for comparison of the small samples of used resin-coated proppant.

Crush tests were performed on used proppant samples taken from each of the ampoules A through I. The values of moduli, creep rate and crush fraction were calculated and are listed in Table 3.19. A computer control problem arose during the test of proppant from ampoule B. Fines and crushed proppant grains were removed by sieving and by hand and the uncrushed portion of the sample was re-tested. In addition, a small portion of un-tested proppant from ampoule B remained after the first unsuccessful crush test. That small second sample was also tested. To provide a basis for comparison, samples of fresh sintered bauxite proppant of equal size were also tested. A discussion of the results of those additional tests is included in the *Discussion* section.

Ampoules D and E contained mixtures of quartz sand proppant, a low strength proppant, and granite. Due to the anticipated difficulty in separating the proppant grains from the granite and considering that quartz sand proppant is not expected to perform well in high closure-stress environments, the decision was made to not crush test the quartz sand proppant.

3.4 Discussion

Proppants were submitted to two types of tests designed to evaluate their suitability for use in engineered geothermal systems. The first experiments were designed to test the chemical compatibility of proppants with simulated geothermal conditions. Chemical compatibility is discussed in terms of formation of crystals and other precipitates, resistance to dissolution and water chemistry. The second round of experiments was designed to test the compliance of the proppant and compare the

Table 3.19. Moduli, creep rate and crush fraction were calculated for each sample of used proppant.

Trial	Load 1 Modulus ($\cdot 10^3$ psi)	Load 2 Modulus ($\cdot 10^3$ psi)	Creep Rate ($\cdot 10^{-5}$ 1/ln sec)	Crush Fraction ($\cdot 10^{-3}$ g/g)
A	395	871	15.4	10.3
B	–	–	–	–
B (re-test)	394	754	15.7	11.8
B (Sample 2)	279	497	22.6	14.3
C	428	916	13.0	7.1
F	358	741	37.9	126
G	365	785	41.5	92.5
H	363	744	38.6	76.7
I	342	711	51.8	87.3

A computer control problem arose during the test of proppant from ampoule B rendering the data unusable. Fines and crushed grains were removed by hand and the sample was re-tested. Additionally, a small sample (Sample 2) of proppant not used in the initial test or in the re-test was crush tested.

crushability of proppant used in the tests of chemical stability to the crushability of fresh proppant. Statistical tests of significance were performed.

3.4.1 Tests of Chemical Stability

The results of the tests of chemical stability of proppants under geothermal conditions were strongly affected by the type of apparatus used. The apparatus used in the earliest experiments (Trials 1 through 5) are believed to have leaked. In most cases, some water still remained in the reactors at the end of the experiments; however, in one case (Trial 4), the reactor was completely dry. While it was not possible to record the extent of leakage in the other trials, each of the other reactors (Trials 1, 2, 3 and 5) is believed to have leaked to some degree. The slow leakage of water over time led to oversaturation of dissolved species – as water vapor escaped the reactors, the liquid

volume of water remaining in the reactors decreased and the concentrations of the dissolved species increased. This oversaturation of dissolved species led to significant and sometimes spectacular crystal growth.

Later experiments (Trials A through I) were conducted in leak-free quartz-glass ampoules. In these experiments, there was no oversaturation of dissolved species associated with water loss, and no crystal growth or precipitation was observed, with the noted exception of the apparent growth of crystals of a zeolite mineral in Trial H. Evidence of dissolution of sintered bauxite proppant was widespread and easily observed in SEM photomicrographs.

Dissolution of quartz sand proppant, if it occurred, was not easily observed, though some possible evidence of dissolution was noted. In any case, dissolution of quartz sand is predicted because while the RRG-1 geothermal water contained approximately 130 mg/kg dissolved silica, the present experiments were conducted at 230 °C, at which temperature quartz solubility is much higher (approximately 380 mg/kg).

In contrast to sintered bauxite, resin-coated bauxite proppant appeared to be largely unaffected by exposure to simulated geothermal conditions. None of the dissolution textures that were so characteristic of sintered bauxite surfaces were observed on resin-coated bauxite surfaces. Only a few examples of possible alteration were observed and noted previously. Despite these few exceptions, it appears that the resin coating is largely impervious to attack by hot geothermal water and serves to protect the proppant particles. This benefit is in addition to the tendency of resin-coated proppants to form a solid permeable pack that serves to reduce proppant flow-back.

While the occurrence of dissolution is overtly obvious from the SEM photomicrographs of sintered bauxite proppant, it was difficult to quantify. Water analyses gave some additional information about the amount of dissolution that occurred and the identity of the species that were involved. The water chemistry indicates that minerals containing calcium, silica and sulfates dissolved during the reactions. Sodium and chloride concentrations in the water remained unchanged from levels observed in the geothermal water before the experiments.

Three silica geothermometers were applied to the results of the chemical analyses as a check of validity. Geothermometry uses concentrations of dissolved solids (the geothermometers listed here use SiO_2 concentration exclusively, but other geothermometers use other species concentrations) to estimate the temperature at which the solids dissolved. Table 3.20 gives the equations used to calculate the three geothermometers and Figure 3.29 shows the concentration curves resulting from the three geothermometers. Table 3.21 gives the laboratory-determined silica concentrations. In comparison, the silica concentrations at 230 °C predicted by the quartz (eq 3.2), amorphous silica (eq 3.3) and chalcedony (eq 3.4) geothermometers are 377.9 mg/kg, 1167.2 mg/kg and 435 mg/kg, respectively. In Figure 3.30, the laboratory-obtained data are plotted on top of the silica concentration curves of the geothermometers.

The quartz geothermometer (eq 3.2) was also applied to the Raft River well RRG-1 water. Based on the measured silica concentration in the water (averaged over three analyses), reservoir temperature was calculated to be 153 °C. The quartz geothermometer was chosen over the chalcedony and amorphous silica geothermometers because quartz is expected to be the dominant silica phase in the reservoir.

Table 3.20. Equations defining the geothermometers referenced in Table 3.21.

Quartz[a]	$T = -42.198 + 0.28831[SiO_2] - 3.6686 \cdot 10^{-4}[SiO_2]^2 + 3.1664 \cdot 10^{-7}[SiO_2]^3 + 77.034 \log[SiO_2]$	(3.2)
Amorphous Silica[b]	$T = \left[\frac{731}{(4.52 - \log[SiO_2])}\right] - 273$	(3.3)
Chalcedony[b]	$T = \left[\frac{1032}{(4.69 - \log[SiO_2])}\right] - 273$	(3.4)

T = temperature (°C)
[SiO2] = silica concentration (mg/kg)

a) Fournier and Potter (1982)
b) Fournier (1981)

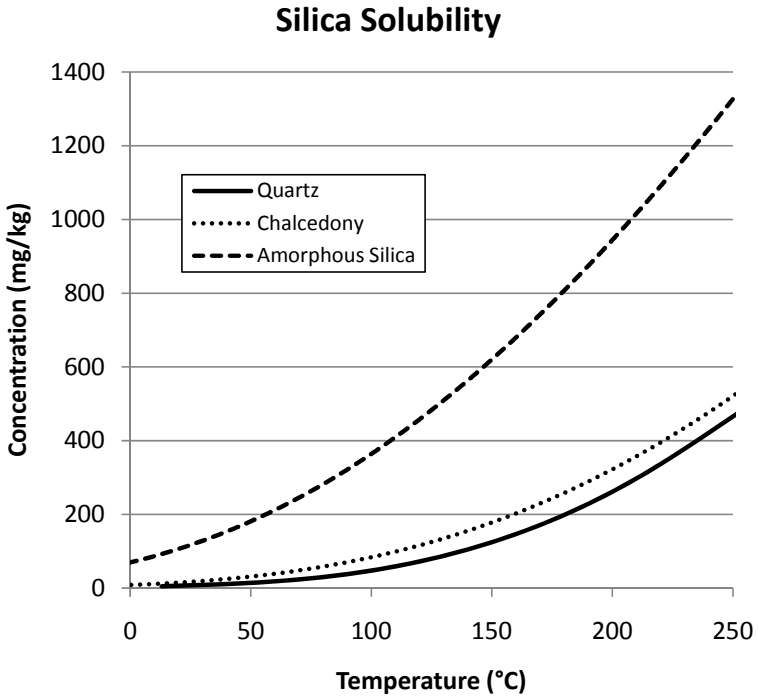

Figure 3.29. Silica solubility as a function of temperature. Solubility curves are calculated according to eqs 3.2 through 3.4 which define three different silica geothermometers.

Table 3.21. Silica concentration reported by Thermochem, Inc.

Trial	Measured SiO_2 (mg/kg)
A	674
B	545
C	649
D	825
E	678
F	629
G	695
H	617
I	709

The geothermometer calculations indicate that the silica concentration levels observed in the trials were higher than would be suggested by chemical equilibrium with quartz and lower than would be suggested by equilibrium with amorphous silica. The ampoules used in the experiments were made from silica glass. It seems likely from the chemical analyses and geothermometry that dissolved silica in the water samples may have been sourced from the ampoules themselves rather than from the proppant or granite in the ampoules. In any event, the validity of using silica concentration as a measure of dissolution of granite or proppant at the test conditions is called into question by the finding.

3.4.1.1 Other Findings

The leakage of water and super-saturation of dissolved species leading to precipitation and crystal growth that occurred in Trials 1 through 5 were viewed initially as problems and were addressed in later experiments (Trials A through I) through

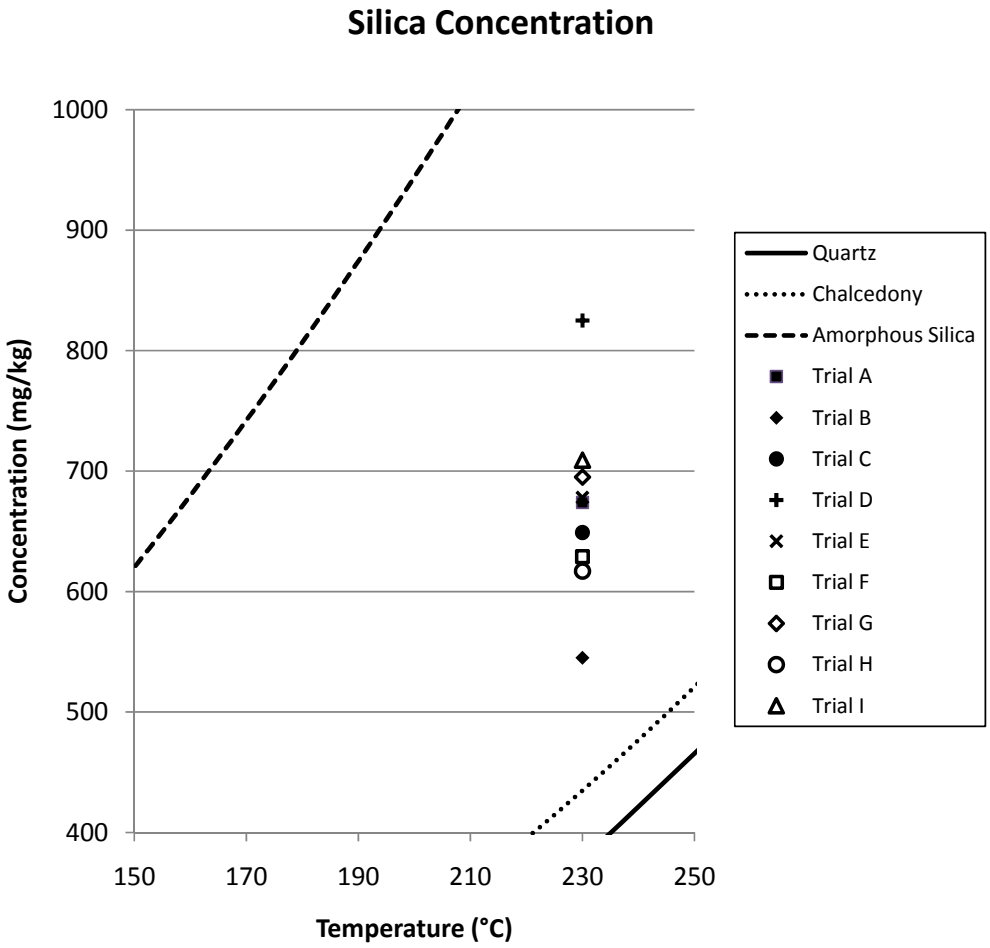

Figure 3.30. Laboratory-obtained silica concentrations from each of the trials are plotted on top of the silica geothermometry curves (from eqs 3.2 through 3.4). The measured silica concentrations fall below the concentration predicted by the amorphous silica geothermometer and above the quartz geothermometer. Figure 3.29 shows the same concentration curves over greater temperature and concentration ranges.

modifications to the apparatus. Nevertheless, the results of those early experiments provide insight into other important processes that may occur in geothermal wells.

Several different minerals including wairakite (?), vermiculite (?), erionite, and a clay mineral consisting mostly of chlorite have been tentatively identified. An amorphous silica coating was commonly observed in the solids from the various reactors. This coating ranged from glass-like to rough, served to coat large portions of proppant

and granite grains and acted as a cement binding grains to one another and in some cases to the walls of the reactors. Direct evidence of dissolution (i.e., dissolution textures) was observed only to limited extent. However, it is taken as a conclusion that some dissolution must have occurred to allow the amount and variety of crystal growth observed in reactor solids.

When water vapor escaped, oversaturation of dissolved solids resulted in crystal growth and precipitation of amorphous solids. This is similar to what might be observed in portions of a geothermal system characterized by boiling of geothermal fluids. Crystal growth and precipitation similar to that observed in these experiments would have the potential to plug pore spaces in a fracture, thus reducing conductivity. These results highlight the importance of reservoir management to avoid pressure drawdown leading to boiling, super-saturation and precipitation and crystal growth. Similar results might be obtained if saturated fluids were allowed to cool significantly.

3.4.2 Crush Tests

Crush tests were performed on fresh and used proppant to quantify the degree to which the proppant was weakened, if any, by long-term exposure to geothermal conditions. Proppant compliance and crushability were quantified in four ways: the moduli of each of the two loading cycles, the creep rate, and the crush fraction. Tests of fresh proppants were conducted in order to create a baseline against which used proppant results were compared. These baseline tests also allowed comparison between the two types of fresh proppant. Results of those baseline tests are included in Table 3.22. Statistical *t* tests were also performed to gauge the difference between proppant types.

Table 3.22. Comparison of sintered bauxite and resin-coated bauxite proppants.

Metric	Sintered Bauxite (2.0-g sample)	Resin-coated Bauxite (2.0-g sample)	t
Load 1 Modulus ($\cdot 10^3$ psi)	440 ± 39	377 ± 13	4.3
Load 2 Modulus ($\cdot 10^3$ psi)	892 ± 26	905 ± 19	-0.98
Creep Rate ($\cdot 10^{-5}$ 1/ln sec)	14.9 ± 2.3	43 ± 4.6	-12
Crush Fraction ($\cdot 10^{-3}$ g/g)	13.8 ± 7.4	93.9 ± 7.4	-18

For the degrees of freedom and at the 95% confidence level used, *t* values greater than 2.18 or less than -2.18 indicate a difference in the means that is statistically significant.

The *t* tests show that, based on measurements of the load 1 modulus, creep and crush fraction, the two proppant types are distinguishable and statistically significant differences exist between the two. Figure 3.31 gives the average stress-strain curves for the 2.0-g samples of the two proppant types. It is clear from the graph and from the results of statistical tests that the two proppant types differ in crushability. However, the two proppant types were of different mean particle size (see Tables 3.1 and 3.5) and that difference likely played a larger role in the crushability difference than any other factor.

If the proppant resistance to crushing had been significantly reduced by exposure to geothermal conditions, the reduction would have manifested itself by a decrease in the moduli, an increase in the creep or an increase in the crush fraction relative to the fresh proppant values.

When the proppant from Trial B was being tested, a problem with computer control of the test led to stresses above specification being applied to the sample. The

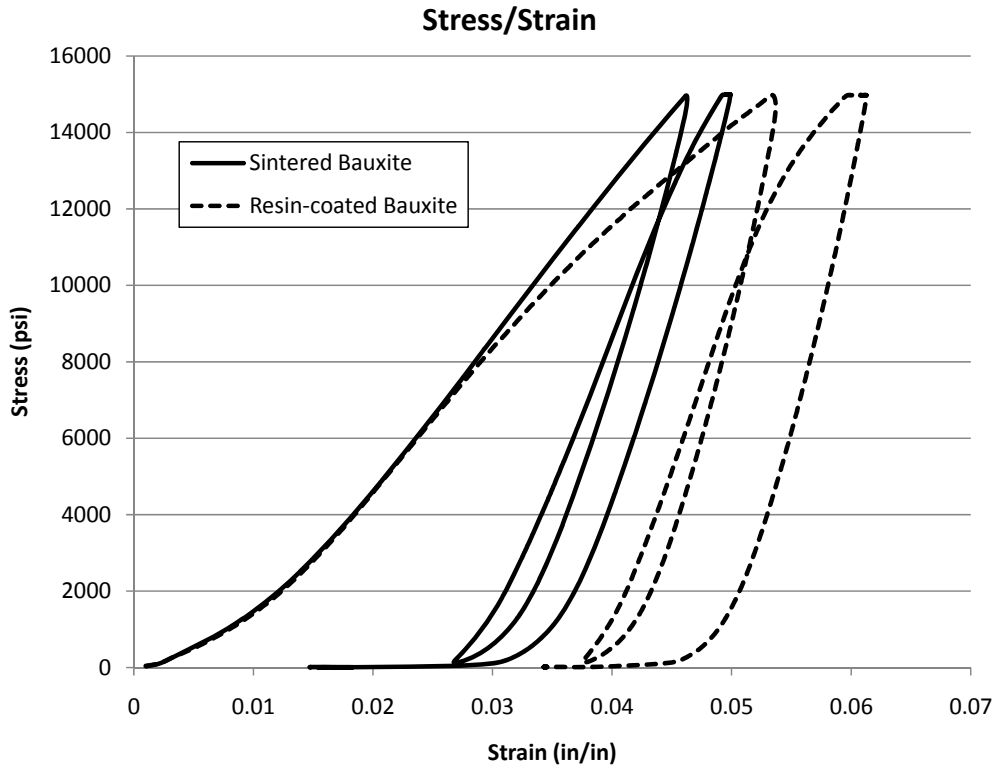

Figure 3.31. Average stress-strain curves.

test data were excluded from further analysis. In an effort to recover some data from the sample, a smaller second sample of proppant from Trial B was crush tested. Although the test went according to the specification, the test results were significantly different. The moduli for both the first and second loading cycles were significantly lower when the smaller sample was tested than when the larger samples of the same proppant type (fresh or used) were tested. The creep for the smaller sample, however, was greater than creep for larger samples. These differences are likely the result of compaction or other effects that vary with sample height in the crush test cell.

A second effort to recover data from Trial B was made. The crushed sample from the first test was sieved and broken proppant grains were removed by hand working under a microscope. The proppant grains that were apparently unbroken were subject to

yet another crush test. It is possible that proppant breakage in the first test occurred non-normally (i.e., grains of a certain size or shape may have broken preferentially). In any case, the proppant grains that were broken during the first test and subsequently removed may not be representative of the whole sample. The selective removal of broken grains and fines from the crushed sample was necessary since they would certainly have had an effect on the results of the second test, but that selective removal also calls into question validity of the second test.

A significant difference between compliance of fresh samples of sintered bauxite and resin-coated bauxite proppants was observed. Unfortunately, the two proppant types had differing mean particle sizes. When a load is applied to an unconsolidated sample such a proppant pack, the load is transmitted between particles where the particles touch. Larger particles result in a pack that has less contact surface area between particles and therefore higher stress concentrations. The difference in strength noted between the two proppant types is likely a function of particle size more than proppant composition or coating. It is therefore impossible to draw any conclusions on the effect of proppant resin-coating on crush resistance.

Statistical *t* tests of significance were applied to the crush test data. The small amount of used proppant from each trial that was available for crush testing prevented duplicate tests from being run and precluded calculations of the mean and standard deviation of the four metrics of the used proppant samples. To make statistical tests possible, the standard deviations calculated from the duplicate tests of fresh proppants were applied to the results of tests conducted on single samples of used proppant. Tables 3.23 through 3.26 present the results of crush tests along with calculated *t* values.

Table 3.23. Results of crush tests on sintered bauxite proppant (2.0-g sample size).

Trial	Load 1 Modulus ($\cdot 10^3$ psi)	Load 2 Modulus ($\cdot 10^3$ psi)	Creep Rate ($\cdot 10^{-5}$ 1/ln sec)	Crush Fraction ($\cdot 10^{-3}$ g/g)
Sintered Bauxite (average)	440 ± 39	892 ± 26	14.9 ± 2.3	13.8 ± 7.4
A	395	871	15.4	10.3
C	428	916	13.0	7.09

Table 3.24. Results of t tests of statistical significance on findings from crush tests on sintered bauxite proppant (2.0-g sample size).

Trial	Load 1 Modulus	Load 2 Modulus	Creep Rate	Crush Fraction
	t values			
A	1.1	0.77	-0.22	0.46
C	0.29	-0.87	0.79	0.87

Table 3.25. Results of crush tests on resin-coated bauxite proppant (1.50-g sample size).

Trial	Load 1 Modulus ($\cdot 10^3$ psi)	Load 2 Modulus ($\cdot 10^3$ psi)	Creep Rate ($\cdot 10^{-5}$ 1/ln sec)	Crush Fraction ($\cdot 10^{-3}$ g/g)
Resin-coated Bauxite (average)	342 ± 12	748 ± 16	46.5 ± 9.7	104 ± 10
F	358	741	37.9	126
G	365	785	41.5	92.5
H	363	744	38.6	76.7
I	342	711	51.8	87.3

Table 3.26. Results of t tests of statistical significance on findings from crush tests on resin-coated bauxite proppant (1.50-g sample size).

Trial	Load 1 Modulus	Load 2 Modulus	Creep Rate	Crush Fraction
	t values			
F	-1.3	0.40	0.87	-2.1
G	-1.9	-2.2	0.51	1.1
H	-1.7	0.24	0.80	2.7
I	0.034	2.2	-0.53	1.7

Tables 3.23 and 3.24 pertain to tests conducted on sintered bauxite proppant. In Table 3.23, the results of tests on Trials A and C are compared with the mean results of tests on fresh sintered bauxite proppant. Table 3.24 gives calculated values of the *t* statistic; *t* values greater than 2.57 or less than -2.57 indicate a result that is statistically different from the mean of a particular metric of the fresh proppant. The calculations of *t* were based on 5 degrees of freedom and a 95% confidence level

Table 3.25 and 3.26 pertain to tests conducted on resin-coated bauxite proppant. Table 3.25 compares the results of tests on proppant from Trials F through I with the mean results of tests on fresh resin-coated bauxite proppant. Table 3.26 gives the values of the *t* statistic. As before, values greater than 2.57 or less than -2.57 indicate a statistically significant difference from the mean of a particular metric of the fresh proppant.

The *t* tests of the data show that in all but one instance, the resistance to crushing of used proppant was not affected in a statistically significant way by long-term exposure to the simulated geothermal conditions. The lone exception is the crush fraction of Trial H proppant; the value of the *t* statistic of the crush fraction indicates that the used proppant is different from the fresh proppant. However, when viewed in the larger

context, this result is more likely to be an outlier than an important result. Moduli, creep rate and crush fraction of the three other samples (Trials F, G and I) of used resin-coated proppant and moduli and creep rate of the sample from Trial H all indicate that no statistically significant different in proppant compliance resulted from the long-term exposure to geothermal conditions.

3.5 Conclusions

Tests of chemical compatibility of proppants under simulated geothermal conditions revealed that sintered bauxite was susceptible to substantial dissolution. Dissolution textures were commonly observed on surfaces of sintered bauxite proppant from trials conducted in sealed ampoules. Trials that were conducted in the leaky reactors were characterized by precipitation and crystal growth on sintered bauxite surfaces. The precipitation and crystal growth were due to water loss during the experiments. While dissolution textures were not commonly observed on samples from the leaky reactors, this is probably because they were obscured by precipitates and other crystal growth.

Probable dissolution textures were observed on quartz sand proppant surfaces though they were not nearly as obvious and wide-spread as dissolution textures on sintered bauxite proppant surfaces. Resin-coated bauxite proppant appeared to be largely unaffected by exposure to hot geothermal fluid. In addition, zeolite crystal growth was observed in samples from Ampoule H. Only a small percentage of proppant surface area was actually imaged using SEM. The small sample size precludes broad statements about the amount of dissolution which occurred. All that can be said is that dissolution of resin-coated bauxite proppant was not observed to any significant extent.

Analyses of water chemistry indicate that some dissolution of a calcium-containing mineral or minerals (likely anorthite present in granite) occurred. The water also contains elevated silica concentrations. The silica could have been sourced from quartz sand proppant grains, quartz in the granite, and/or from the quartz-glass ampoules themselves. Geothermometry suggests that the ampoules are the likely source of dissolved silica.

Crush tests of fresh proppant samples indicate a statistically significant difference in compliance between sintered-bauxite proppant and resin-coated bauxite proppant. This difference, however, is likely due more to the difference in proppant mean particle size than to any other single factor including proppant composition or surface coating.

Crush tests on the used proppant samples show that, even in the case of sintered bauxite, which underwent dissolution during chemical stability tests, proppant compliance was not significantly affected. Quartz sand proppant was not crush tested.

Resin-coated proppant is a candidate for deployment in engineered geothermal systems. It is well suited to the application since:

- its resin coating serves to bind proppant grains together in a permeable pack, thus reducing the risk of proppant flow-back, an important feature in proposed geothermal fractures that can be expected to see high fluid flow rates during production,
- its resin coating acts as a protective layer, which appears to be impervious to attack from hot geothermal fluid, and
- resin-coated proppant does not experience any significant weakening due to exposure to geothermal conditions.

3.6 Suggestions for Future Work

The current study of chemical stability of proppants under geothermal conditions consisted entirely of batch experiments. Under batch conditions, dissolution of proppants may have been limited by chemical equilibrium in addition to reaction kinetics. Similar long-term experiments could be conducted in a flow-through loop. Such an apparatus would be similar to that described by Ngothai et al. (2009) and would allow sampling of water and water replacement during the course of an experiment. Tracking water composition over time would give an indication of dissolution kinetics and would allow approximations of saturation concentrations of dissolved species.

Future experiments should be conducted using various proppant types of the same mean particle size. Similarity in size would allow direct comparison of proppant crushability across proppant types, allowing conclusions to be made about the effects of proppant composition or coating.

4. SUMMARY AND CONCLUSIONS

Hydraulic fracturing has been practiced in oil and gas reservoirs since the late 1940s. More recently, hydraulic fracturing has been applied to geothermal systems. It is necessary to create large, complex fracture networks in geothermal reservoirs which lack sufficient permeability and/or water saturation and recharge. These fracture networks may be created by forming new fractures in the host rock or by re-opening existing fractures. While hydraulic fracturing of oil and gas reservoirs is a well-developed technology, fracturing crystalline basement rocks for the formation of engineered geothermal systems (EGS) is a less well-developed technology and there are a number of issues which are unique to the EGS concept. For example, in addition to hydraulic fracturing, thermal fracturing due to the alteration of in situ stress states may also occur. Well RRG-9 at the Raft River geothermal site is scheduled to be thermally and hydraulically fractured – permeability is low and the well is not connected to a recharge network.

As cold water is injected into a hot reservoir, a cooled region will evolve outward from the well along fluid flow paths and into the virgin reservoir. The growth of the cooled region will be governed by thermophysical properties of the reservoir rocks including density, heat capacity and thermal conductivity. The temperature change and coefficient of thermal expansion will govern the alteration of the in situ stress state within the cooled region. The evolution of the cooled region may lead to the formation of

thermal fractures due to thermal contraction of the rock as temperatures decrease. In order to forecast the development of the cooled region and thermal fractures and ultimately to forecast thermal energy production, the thermal conductivity of the reservoir must be known. A method for obtaining thermal conductivity from well log data and drill cuttings was developed.

Well log and drill cuttings data were used with Williams and Anderson's model to predict the thermal conductivity of well RRG-3A at Raft River, Idaho. Well log and drill cuttings data were analyzed using principal components analysis, regression analysis and analysis of variance. The relationships obtained from these analyses were used in applying the Williams and Anderson model. To assess the accuracy of the model prediction, the thermal conductivity of two core samples from RRG-3C was determined in the laboratory. The lab-determined conductivities did not match the model-derived conductivities particularly well. The difference in the data sources (legs A and C) clearly contributes to the discrepancies. Rock anisotropy, inaccuracies in acoustic wave velocity data, experimental error or inappropriateness of the model for the specific rock type may also contribute to the discrepancies. The method used is, however, a good first approximation of thermal conductivity and can be used to create a thermal conductivity log. The same method can be applied to RRG-9 to predict thermal conductivity prior the planned thermal and hydraulic fracturing campaigns.

Thermal conductivity is also an important parameter in predicting geothermal well energy production. Sensitivity analyses were performed that indicate that a reservoir of rock of thermal conductivity of 3.5 W/m·K may be expected to produce 20% more energy than a similar reservoir of rock of thermal conductivity of only 2.0 W/m·K over a

20-year of production period. The sensitivity analyses also reemphasize the importance having reliable thermal property data.

Thermal conductivity is an important parameter because it defines the way temperature gradients form and the rate at which thermal energy moves through a reservoir. Hydraulic conductivity within a fracture is also important because it controls the rates at which water can be circulated through the reservoir and heat energy can be extracted. Both properties play a role in heat energy production from a geothermal well. In hydraulically fractured petroleum wells, proppant is almost always used to maintain hydraulic conductivity. However, it cannot simply be assumed that proppant will perform well under geothermal conditions. Proppant may dissolve or participate in chemical reactions with the geothermal brine or host rock. Proppant compatibility with geothermal conditions must be understood since any reduction in hydraulic conductivity may also lead to reduction in thermal energy production. Studies of proppant compatibility with conditions relevant to the Raft River geothermal site have been conducted.

Proppant stability under geothermal conditions was evaluated using a series of experiments in which three types of proppant were exposed to hot geothermal brine for extended periods of time. Additionally, two of those proppants were further tested by mechanical loading to identify and quantify any degradation in resistance to crushing which may have resulted from exposure to simulated geothermal conditions. These tests indicate that sintered bauxite proppant was subject to dissolution under geothermal conditions. Quartz sand proppant also showed some evidence of dissolution. Resin-coated bauxite proppant, however, was found to be largely resistant to dissolution

perhaps due to its resin coating. The two bauxite proppants were subjected to crush tests and in neither case was proppant resistance to crushing found to be materially affected by exposure to hot geothermal brine.

APPENDIX A

MULTIVARAITE DATA ANALYSIS

A.1 Discriminant Function Analysis

Discriminant function analysis (DFA) is a method of multivariate data analysis which seeks to reduce the dimensionality of multivariate data and is frequently employed in sorting applications. Since it is impossible to visualize high-dimensional data, this general discussion will be limited to data in two dimensions which can easily be graphed in two-dimensional Cartesian space though the same methods can be applied to n-dimensional data. Figure A.1 is a scatter plot of example of bivariate (i.e., two-dimensional) data. Two groups of data (A and B) representing two different populations are shown.

From the scatter plot, it is clear that the two groups are different from each other; Group A tends to have high Y values and low X values while group B tends to have low Y values and high X values. However, a closer look at the histograms (Figure A.2) shows that it is not possible to distinguish group A from group B by considering either X or Y variables alone. On the scatter diagram, however, it is easy to make the distinction when X and Y variables are considered simultaneously. Discriminant function analysis yields a linear combination of the variables (the discriminant function) which simultaneously maximizes the variance between two groups of data while minimizing the variance

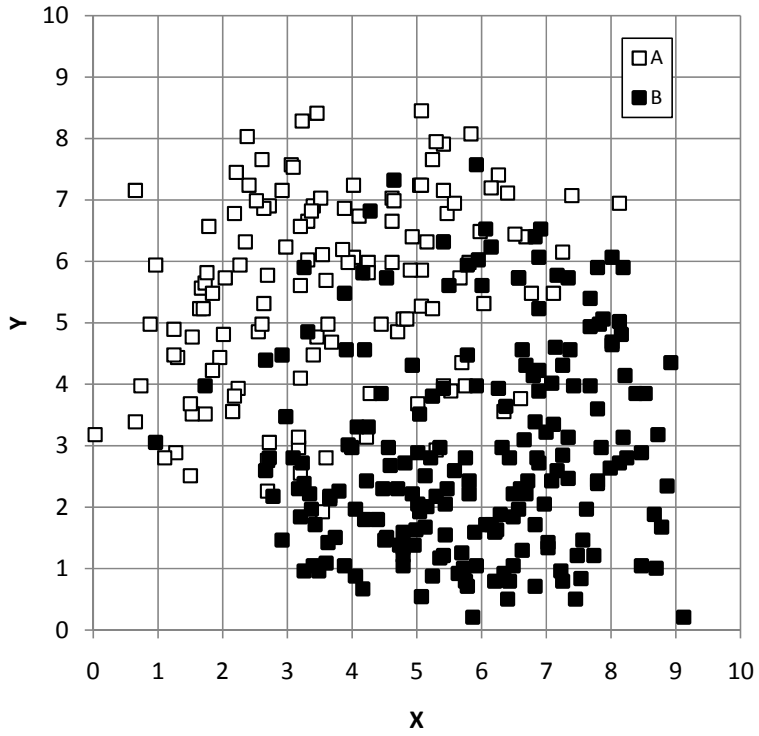

Figure A.1. A scatter plot of sample data of two groups. It is clear that the two groups are different from each other.

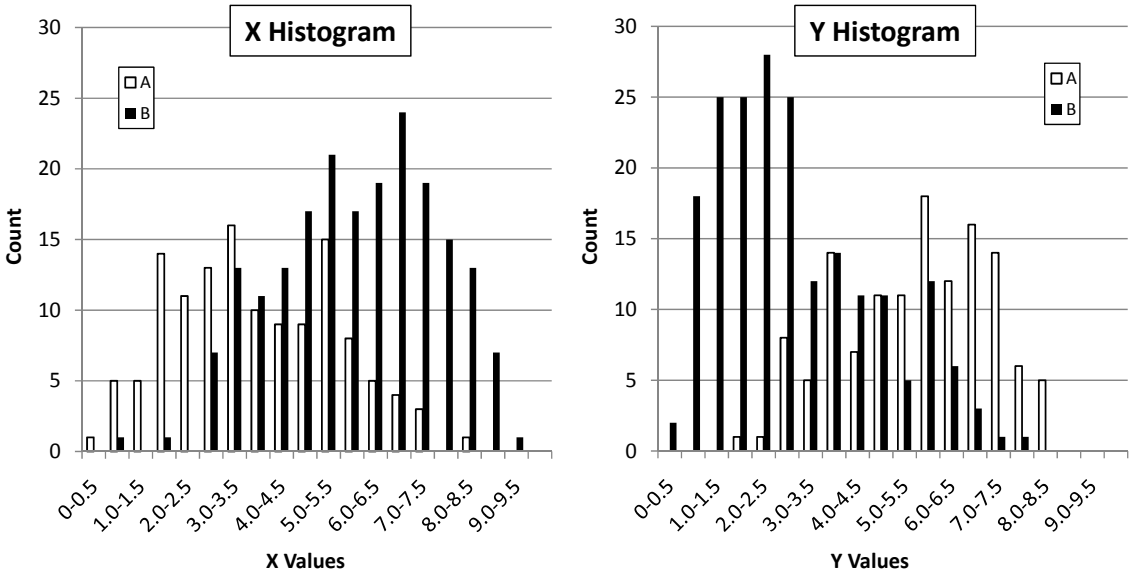

Figure A.2. X and Y histograms of the bivariate data shown in Figure A.1. The histograms show that the two groups of data are not well sorted by either the X or Y variable. It is clear from Figure A.1 that the two groups of data are different from one another but neither variable X not variable Y can be used to distinguish between the two groups.

between individual observations within each group. Davis (2002) provides a complete though succinct and readable discussion of DFA.

Discriminant function analysis is one of a family of methods which can be used to reduce the dimensionality of multivariate data. The projections of the multivariate data onto the discriminant function axis are the discriminant scores of the data. The discriminant scores are a univariate representation of the multivariate data. Figure A.3 is a histogram of discriminant scores of the original bivariate data. Although some of the total variance is necessarily lost due to the reduction of dimensionality, discriminant function analysis is designed to maintain the largest amount of between-group variance possible.

The histogram in Figure A.3 indicates that the two groups are effectively sorted by the discriminant score while neither the *X* variable nor the *Y* variable alone effectively distinguished between the two groups. Discriminant function analysis is most commonly applied to sorting problems. If the *X* and *Y* values of an unknown sample (i.e., it is not known whether the sample comes from group A or group B) are known, the discriminant function can be used to determine the group to which the unknown sample likely belongs. While the overlap between the two groups will lead to some misclassifications, the degree of overlap of the discriminant scores is certainly less than that of either *X* or *Y* variables. Davis (2002) also discusses statistical tests of significance that can be applied to discriminant function analysis and classification.

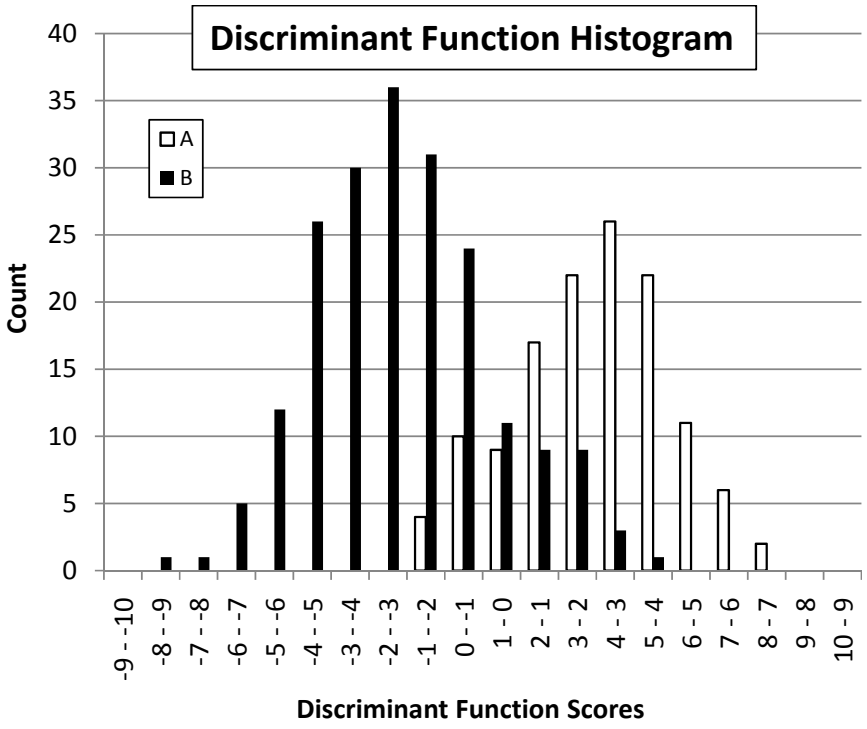

Figure A.3. Histogram of discriminant scores. Discriminant function analysis has transformed the bivariate data, for which neither of the two measured variables were effective in distinguishing between groups A and B, into univariate data – the discriminant score – which does effectively distinguish between the two groups.

A.2 Principal Components Analysis

Principal components analysis is another multivariate data analysis technique that is designed to reduce the dimensionality of a data set. The goal of principal components analysis is to reduce n-dimensional data (data consisting of n variables) to data in some $c < n$ variables (the principal components) while maintaining the largest amount of total variance possible. PCA is similar to discriminant function analysis in several ways with the added benefit that a priori knowledge of the data structure is not necessary (i.e., it is not necessary to select two groups of data upon which the analysis will be based). Additionally, PCA gives more flexibility in choosing the number of components and the amount of variance that is to be retained.

While principal components analysis applies to high-dimensional data, the two-dimensional data plotted in Figure A.4 will serve to demonstrate to the relevant concepts. A variance-covariance matrix for the sample data is shown in Table A.1.

The total variance of the data is the sum of the variances of the individual variables which appear on the diagonal of the variance-covariance matrix. The total variance for this data set is 6.826. The percent of total variance accounted for by each of the two variables is determined by dividing the variance of each variable by the total

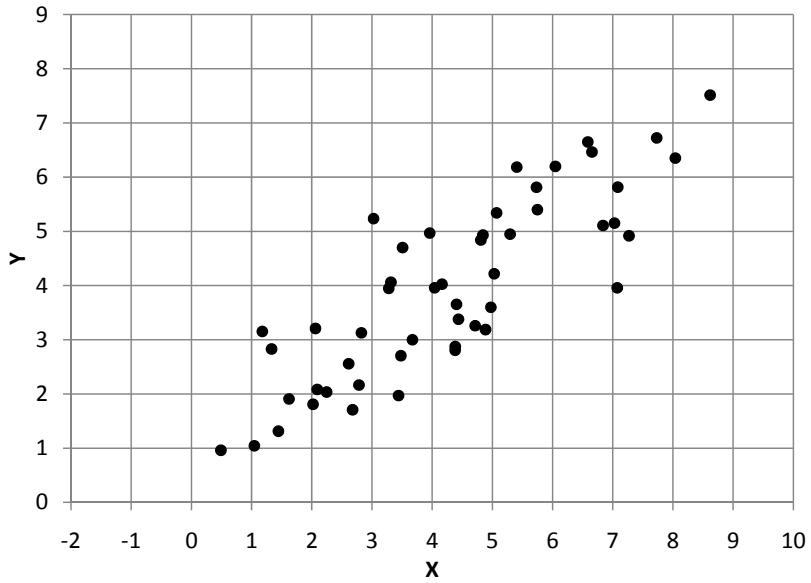

Figure A.4. A scatter plot of fictitious two-dimensional data. This two-dimensional data will serve to demonstrate the basic concepts behind principal components analysis, which can easily be applied to data in n variables.

Table A.1. Variance-covariance matrix of the data plotted in Figure A.4.

	X	Y
X	4.081	2.820
Y	2.820	2.745

variance. Variable *X* accounts for 60% of the total variance while variable *Y* accounts for the remaining 40% of the total variance. This result indicates that both variables are important in defining the data set and neither variable can be disregarded without significant loss of variance.

The covariance of the two variables is given in the off-diagonal elements of the variance-covariance matrix and is a measure of the relationship between the two variables. A better indication of the significance of the relationship between variables is the correlation matrix. A correlation coefficient of 1 indicates a perfect linear relationship between variables. A correlation coefficient of 0 indicates that no linear correlation exists. The correlation matrix for the data is given in Table A.2. The large correlation coefficient indicates that there is indeed a linear correlation between the two variables *X* and *Y*, a conclusion which could have been reached by even a cursory observation of the scatter plot in Figure A.4.

In the present example, principal components analysis will be used to reduce the dimensionality from two variables *X* and *Y* to one principal component. The first step in PCA is the eigen decomposition of the variance-covariance matrix. Because the correlation matrix is always symmetrical, the decomposition can be handled relatively easily by one of several different algorithms. Table A.3 shows the results of the principal

Table A.2. Correlation matrix of the data plotted in Figure 8.

	X	Y
X	1	0.843
Y	0.843	1

Table A.3. Results of principal components analysis conducted on the example data.

	PC1	PC2
X	0.784	-0.620
Y	0.620	0.784
λ	6.311	0.515
% variance	92.5	7.5

components analysis. The principal components are the eigenvectors of the variance-covariance matrix and are linear combinations of the original variables. The elements of the principal component vectors (columns in the top half of Table A.3) are the "loadings" of the individual original variables on the principal components. The eigenvalue, λ, pertaining to a particular eigenvector (principal component) is the amount of variance for which the particular principal component accounts. Because the eigenvalues represent the amount of variance for which the principal components each account, by definition the sum of the eigenvalues is equal to the total variance in the data set. If the eigenvalues in Table A.3 are summed, the result is 6.826 which, as stated before in reference to the variance-covariance matrix, is the total variance of the data. The last line of Table A.3 is the percent of total variance accounted for by the specific principal component. Typically, the principal components are ordered according to their respective eigenvalues, from greatest to least. The first principal component then accounts for the largest percentage of the total variance with each successive component accounting for less variance than the component preceding.

Figure A.5 shows a scatter plot of the example data from Figure A.4 with the principal components superimposed. The principal components are defined by the

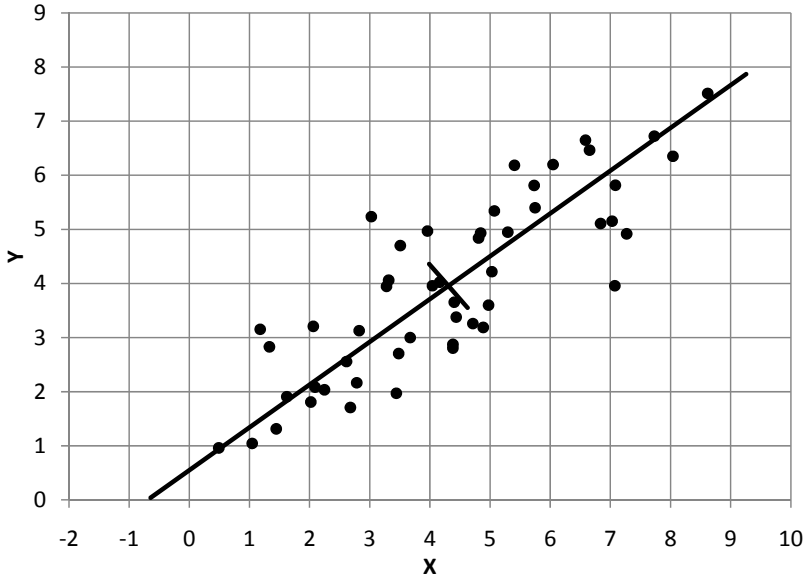

Figure A.5. A scatter plot of the two-dimensional data with the principal components superimposed. The first principal components (associated with the largest eigenvalue) passes through the centroid in the direction of greatest variance. The second principal component passes through the centroid in the direction of least variance.

eigenvectors and pass through the data centroid. The length of a particular principalcomponent is twice its eigenvalue. From Figure A.5 it can be seen that the largest principal component (corresponding to the largest eigenvalue) passes through the centroid of the data in the direction of greatest variance, thus showing graphically that the principal component with the largest eigenvalue does indeed transect the data cloud in the direction of maximum variance. Eigenvectors, and therefore principal components, are orthogonal by definition and each successive principal component transects the data in the direction orthogonal to all preceding eigenvectors and in the direction of the next largest amount of total variance.

The orthogonal principal components can be thought of as a rotated set of Cartesian axes. Data that exist in the original variable space can be transformed into the rotated principal component space by projecting the data onto the principal components.

The projections of data onto the several principal components are called the principal component scores. Figure A.6 is a scatter plot of the principal component scores of the same two-dimensional data. In this transformed space, most of the total variance of the data falls parallel to the first principal component axis (the horizontal axis) and the remaining variance falls parallel to the second principal component axis.

The variance-covariance matrix of the transformed data (Table A.4) shows that 92% of the total variance is accounted for by the first principal component; only 8% is accounted for by the second principal component. The second principal component can be safely disregarded with only a small amount (8%) of total variance being lost. The data are defined nearly exclusively by principal component 1. By contrast, the variance-covariance matrix of the original data (Table A.1) indicates that Variable *X* accounts for 60% of the variance and Variable *Y* accounts for 40% of the variance. Because both variables account for significant amounts of the total variance, both variables are required to define the data.

It is important to note that total variance of the transformed data is exactly the same as the total variance of the original example data. This indicates that the process of projecting data into the principal component space does not result in a loss of variance. It is also noteworthy that the covariance between the principal components as reported in Table A.4 is 0, indicating that there is no linear relationship between principal components, because principal components are orthogonal by definition.

As stated, the objective of principal components analysis is to rotate the data in such a way that the dimensionality of the data can be reduced by disregarding one or more principal components while minimizing the amount of lost variance. Although

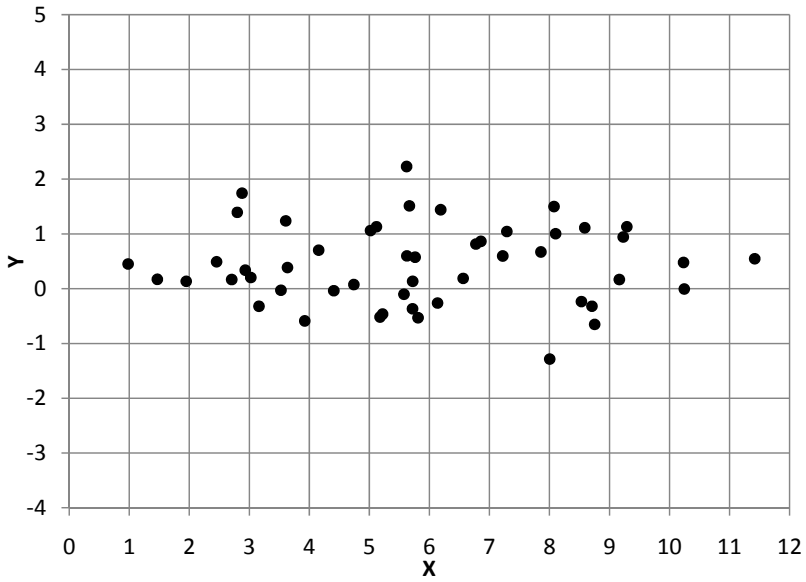

Figure A.6. A scatter plot of the principal component scores of the two-dimensional data. The original data have been transformed into principal component space.

Table A.4. Variance-covariance matrix of the principal component scores (shown in Figure A.6) of the two-dimensional example data.

	PC1	PC2
PC1	6.311	0
PC2	0	0.515

rotation of multivariate data into principal component space is a loss-less procedure (i.e., does not result of loss of data variance), there is loss of data variance when one or more principal components are disregarded. The decision to disregard one or more principal components is at least somewhat subjective and is left to the analyst. More will be said on the subject later.

If the variance or values of one variable are significantly larger than those of other variables or if variable units differ, the one variable may have a more significant affect on the outcome of the PCA than other variables. Data standardization ensures that each variable has a mean of zero and a standard deviation of one and, therefore, that each variable has equal weight in the analysis. Standardization is performed by first subtracting the variable mean value from each data point and then dividing the result by the standard deviation of the variable. Standardization is performed for each variable in the data set.

Data standardization was performed on the original two-dimensional example data. Because the variance of each standardized variable is one, when standardized data are analyzed, the total variance of the data is equal to the number of variables. Similarly, the data transformed into principal component space have a total variance equal to the number of variables. In this case, the first principal component accounts for 92% of the total variance while the second principal component accounts for only 8% of the total variance. In the present example, when data standardization is performed before PCA, the results are qualitatively similar to the results of the PCA of the original unstandardized data (see Figure A.7 and Tables A.5 and A.6). However, in a data set in which the variances of the several variables differ greatly, the results of PCA of

Table A.5. Variance-covariance matrix of the standardized example data.

	X	Y
X	1	0.843
Y	0.843	1

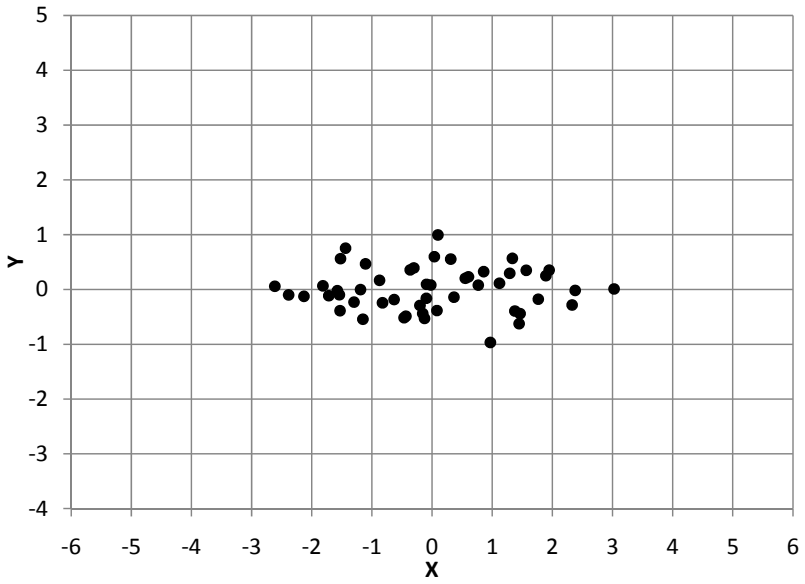

Figure A.7. Scatter plot of the principal component scores of the standardized example data. Note that the results are qualitatively similar to the results for the unstandardized data. This may not be the case when variances of the unstandardized variables differ greatly.

Table A.6. Variance-covariance matrix of the principal component scores of the standardized example data.

	PC1	PC2
PC1	1.843	0
PC2	0	0.157

standardized data would potentially be significantly different than the results of PCA of un-standardized data.

As stated, principal components analysis is a dimensionality reduction method. Dimensionality is reduced by disregarding one or more principal components. By disregarding a component, the variance accounted for by that component is also lost. The problem of determining the number of principal components which should be retained becomes an optimization problem. Although it is desirable to retain as much of the total variance as possible, reduction of dimensionality requires some loss of variance. The decision to disregard or retain a component will likely depend on the planned use of the data. For example, the desired result might be univariate data for application in a linear regression analysis. If this is the case, then only one principal component can be retained. There are guidelines and rules of thumb for determining the number of components to retain. For a complete discussion of principal components analysis as well as a discussion of methods for determining the number of components to retain, the reader is once again referred to Davis (2002).

Some principal components may lend themselves to interpretation in the original variable space. Variable loadings on principal components can be useful in interpreting the principal components. Principal components do not have any real inherent meaning other than that they are the linear combinations of measured variables. However, the loadings may indicate that particular principal components are related to certain variables of one type or other and may be interpreted as having meaning in the real variable space (Dunteman, 1989; Gonçalves, 1998).

A.3 Cluster Analysis

Cluster analysis deals with the grouping of observations into clusters such that the variance within each cluster is smaller than the variance between clusters. The number of the clusters will depend on the nature of the data set and the way in which the results will be used. Importantly, the clusters are defined during the analysis and the cluster definitions change throughout the course of the analysis. Groups are not defined *a priori,* with observations then placed in the groups as is the case in classification analyses, the traditional application of discriminant function analysis. Rather, the natures of the clusters change as the number and properties of cluster members change.

Three fundamental characteristics define a cluster analysis method: 1) the type of analysis algorithm, 2) the proximity measure, and 3) the method of determining distance between clusters. There are at least two basic types of cluster analysis algorithms, each with its own set of variants. Partitional algorithms require that the user specify the number of clusters. The algorithm then tests each observation for membership in the clusters. The numbers of members and center of each cluster change as new observations are assigned to and other observations are removed from the cluster. Hierarchical methods do not require that the user specify the number of clusters at the beginning of the analysis. Instead, observations are clustered together one at a time based on their distance from other observations and clusters. The results of hierarchical clustering are most commonly presented in the form of a dendogram. The analyst must then decide where to "cut" the dendogram, thus defining the number and nature of the clusters. Hierarchical methods are the most common in the geosciences and will be the focus of this discussion.

There are many ways of determining the distance or proximity between observations and clusters, each of which will produce a different result. Xu and Wunsch (2009) provide a synopsis of many different proximity measures including the Euclidian distance, Manhattan distance, and distance based on the correlation coefficient, while Davis (2002) uses the correlation coefficient directly as a proxy for proximity.

The distance between clusters can be determined in many ways. Examples include the single linkage algorithm, in which the distance between clusters is the minimum distance between all possible pairs of members of the two clusters; the complete linkage algorithm, in which the distance is the maximum possible distance between all possible pairs of members of the two clusters; the centroid linkage algorithms, in which distance is calculated as the distance between cluster centroids; and Ward's method which merges clusters in such a way as to minimize the within-cluster squared error for any given iteration.

A complete discussion of the possible permutations of clustering methods, proximity measures and distance algorithms is well beyond the scope of the current work. A detailed analysis of the algorithms and proximity and distance measures can be found in Xu and Wunsch (2009).

There are two types of hierarchical clustering methods. Divisive hierarchical clustering methods begin with all observations in one cluster. Each iteration results in a cluster being split into two clusters (for clarification and exactness it should be stated that a cluster may contain as few as one observation) until all clusters contain only one observation. Agglomerative hierarchical techniques work in the opposite direction: initially, each observation is in its own cluster and during each iteration, two clusters are

agglomerated until after many iterations, only one cluster, containing all observations, remains. The decisions about how to divide the clusters, in the case of divisive methods, and how to agglomerate clusters in the case of agglomerative methods, are based on the distances between clusters. Agglomerative methods are computationally less intensive and more common than divisive methods.

A two-dimensional data set is used once again to show how clustering algorithms proceed. Consider the two-dimensional data plotted in Figure A.8. If it is desired to place each data point in one of four groups based on the position of the data point in two-space, the task could be completed relatively easily by observation. Alternatively, a clustering algorithm could be used to methodically analyze the data, calculate proximity and distance measures, and objectively place each data point in a group.

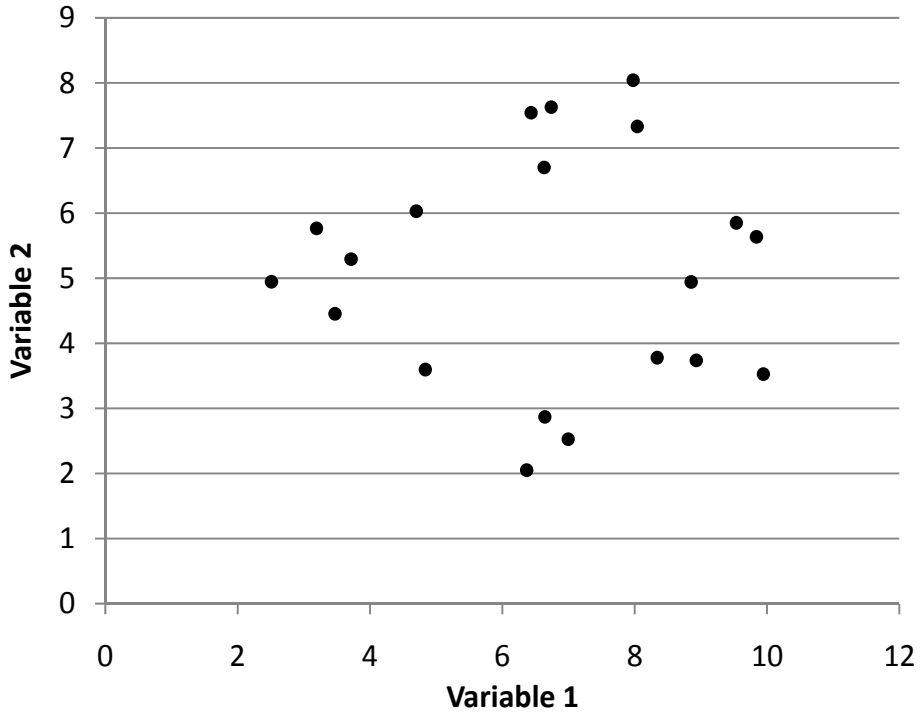

Figure A.8. A plot of a sample two-dimensional data set. The data seem to naturally fall into perhaps three to four groups. The task of defining the group memberships would be relatively easy in this case.

An agglomerative clustering algorithm can be used to generate a dendogram which indicates the structure of the data and how individual data points are clustered together. During each iteration through the algorithm, a single agglomeration is completed. The two clusters or data points agglomerated are chosen based on the distance between them. As stated before, there are many ways of calculating proximity and distance measures, and the different methods will give slightly different results (Davis, 2002). Figure A.9 is a dendogram that was generated by an agglomerative hierarchical clustering method using the Euclidean distance as the proximity measure and by calculating the distance between clusters as the group average distance.

The labels of the data points are listed along the vertical axis on the left side of the diagram. The horizontal axis is the distance measure. Agglomerations are indicated by the vertical lines connecting data points or clusters. The connecting lines representing agglomerations are drawn at the position on the horizontal axis corresponding to the distance between the clusters at the time they were agglomerated. The dashed line represents where the dendogram will be cut. The number of horizontal lines crossing the dashed vertical line is the number of clusters which will result. By moving the dotted line to the left or right, an investigator can choose to consider more or fewer clusters respectively.

Again, the decision of the number of clusters to consider depends on the structure of the data and the intended application of the analysis. In this case, the choice of four clusters seems logical since to the left of the dashed line, agglomerations happen more frequently and are more tightly grouped than to the right of the dashed line. There are methods of quantifying cluster validity (Xu and Wunsch, 2009).

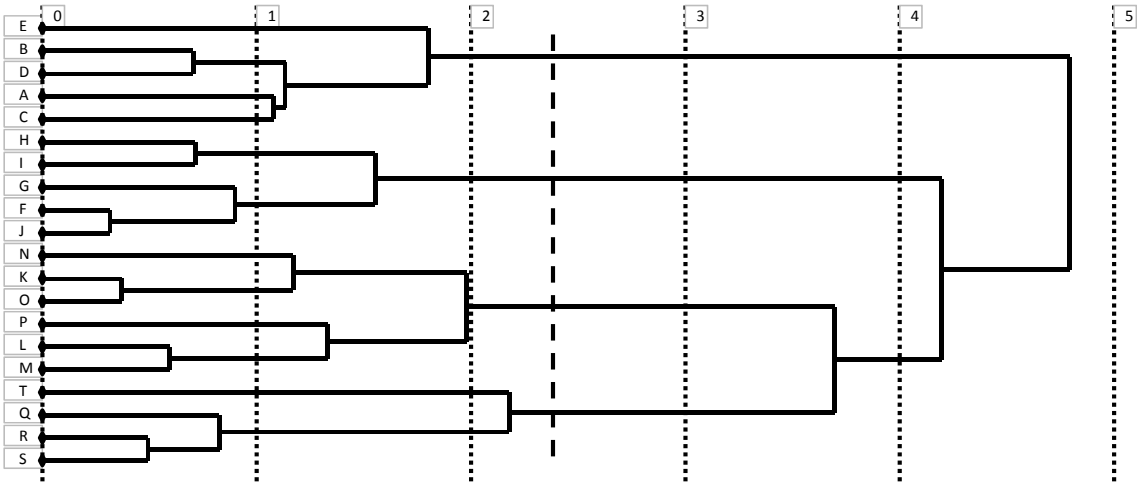

Figure A.9. Dendogram showing the results of an agglomerative hierarchical clustering algorithm employing the Euclidean distance as the proximity measure and calculating distances between clusters as the group average distance. The vertical axis lists the labels for each data point. The horizontal axis is the distance measure. Vertical lines represent agglomerations of data points or clusters and fall at the point on the horizontal axis corresponding to the distance between to the clusters or data points at the time the agglomeration was performed.

Figure A.10 shows the results of the same cluster analysis, now viewed graphically in the original data Cartesian space. Ellipses represent clusters. Only the first 16 iterations (and therefore 16 agglomerations) are shown. Larger clusters contain multiple data points and clusters. For the sake of demonstration, each cluster is given a number corresponding to the order in which it was formed. The cluster formed on the first iteration is labeled "1", the cluster formed on the second iteration is labeled "2", and so forth.

Cluster analysis has commonly been applied to well log facies classification problems. Hierarchical techniques seem to be more common, for example, Gill et al. (1993), Lim et al. (1997) and Moline and Bahr (1995); but nonhierarchical or divisive methods have also been used, for example Gonçalves (1998) and Crampin (2008). Gill et al. (1993) applied an adjacency constraint for cluster analysis of well log data. This

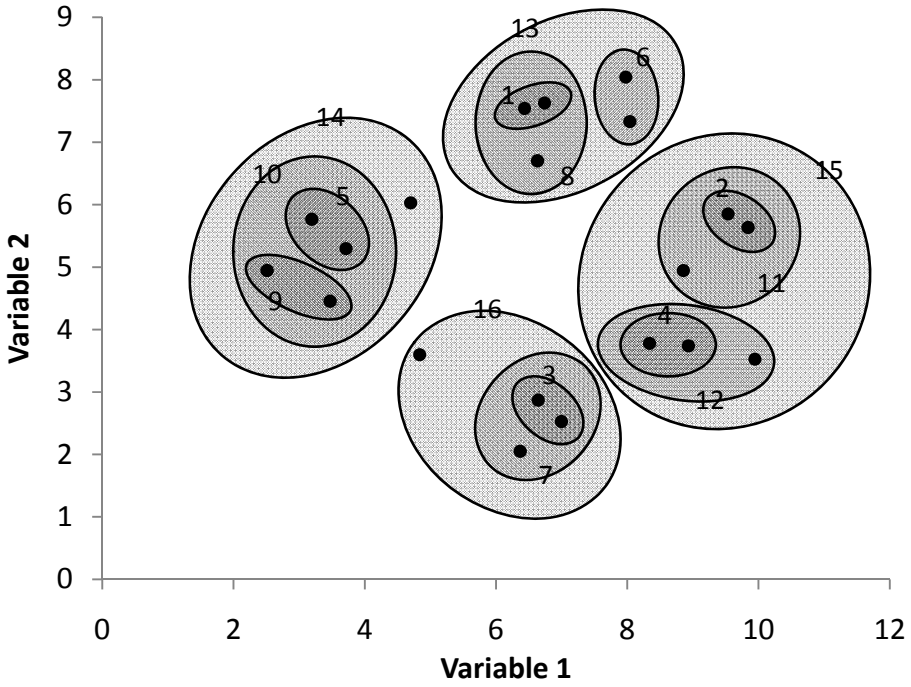

Figure A.10. Scatter plot of sample two-dimensional data with ellipses representing clusters superimposed. Each ellipse (cluster) is numbered according to the order it was formed. For example, the ellipse labeled "3" was formed during the third iteration of the clustering algorithm; the ellipse labeled "14" was formed on the fourteenth iteration.

adjacency constraint only allows the agglomeration of clusters if the clusters are contiguous with one another in the lithologic column. Gonçalves (1998) performed a cluster analysis on a suite of well logs and performed another cluster analysis on the principal component logs of those same well logs and found that the cluster analysis based on PCA logs performed somewhat better. Moline and Bahr (1995) established a work flow for cluster analysis of well log data: principal component logs were constructed, univariate segmentation of the principal component log was conducted, and finally cluster analysis was performed on the segments. Crampin (2008) carefully selected and conditioned a set of well logs for use with over 100 borehole side wall samples in a cluster analysis and correctly classified a large percentage of those samples.

APPENDIX B

TECHNICAL DRAWINGS

Technical drawings of equipment used in tests of proppant stability under simulated geothermal conditions and in tests of proppant crushability are included for reference.

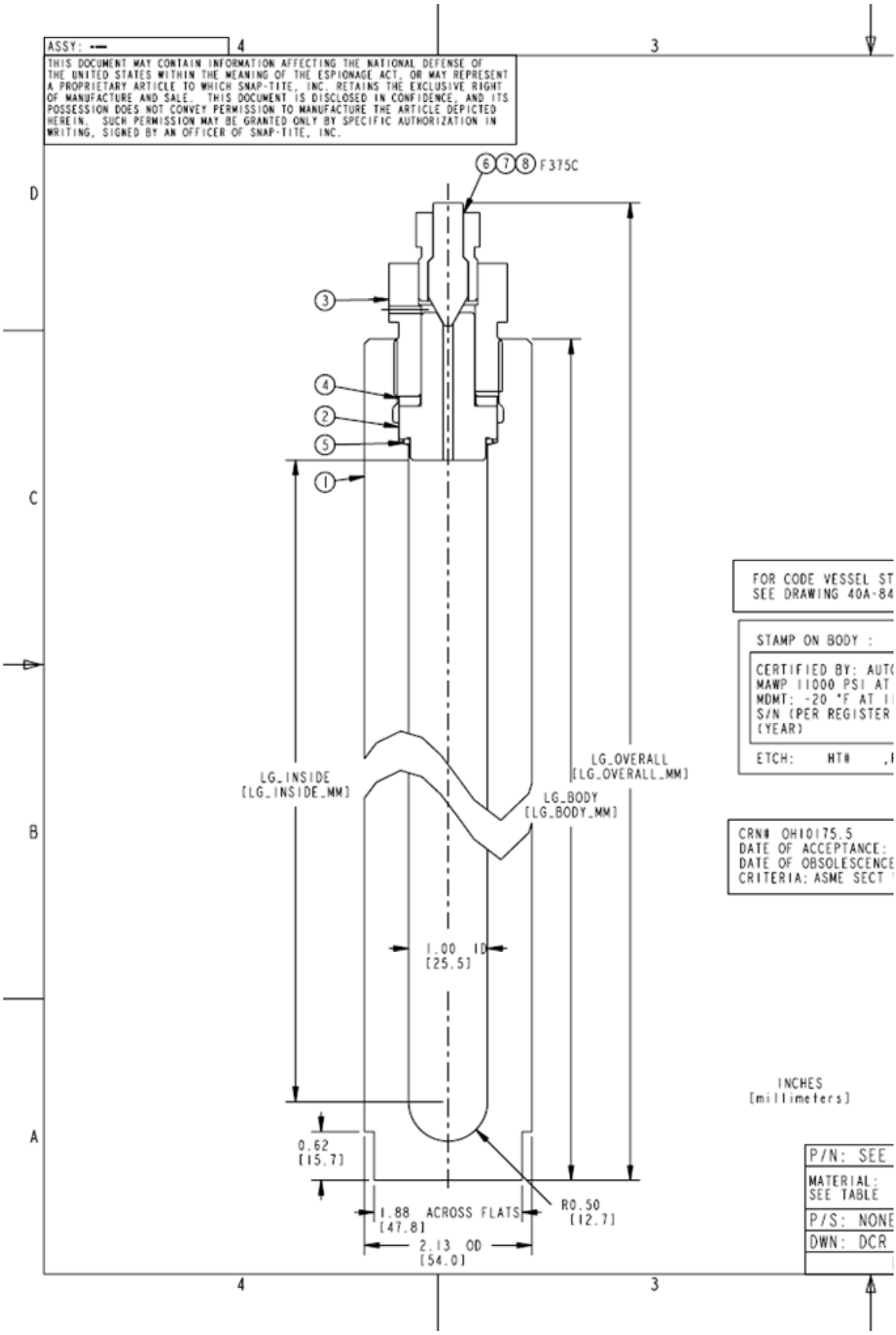

Figure B.1. Technical drawing of Kuentzel closure pressure vessel provided by Autoclave Engineers.

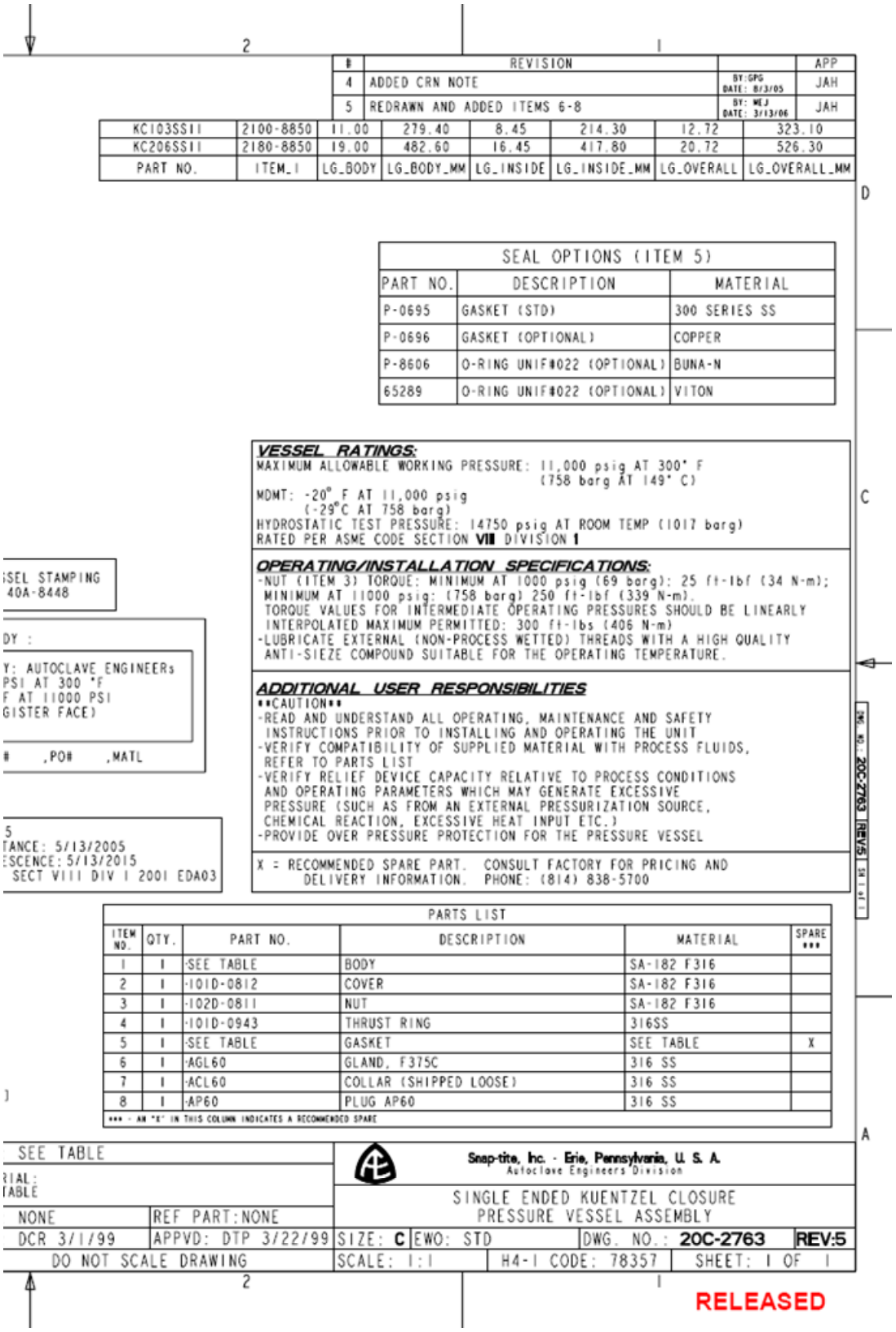

Figure B.1 (continued).

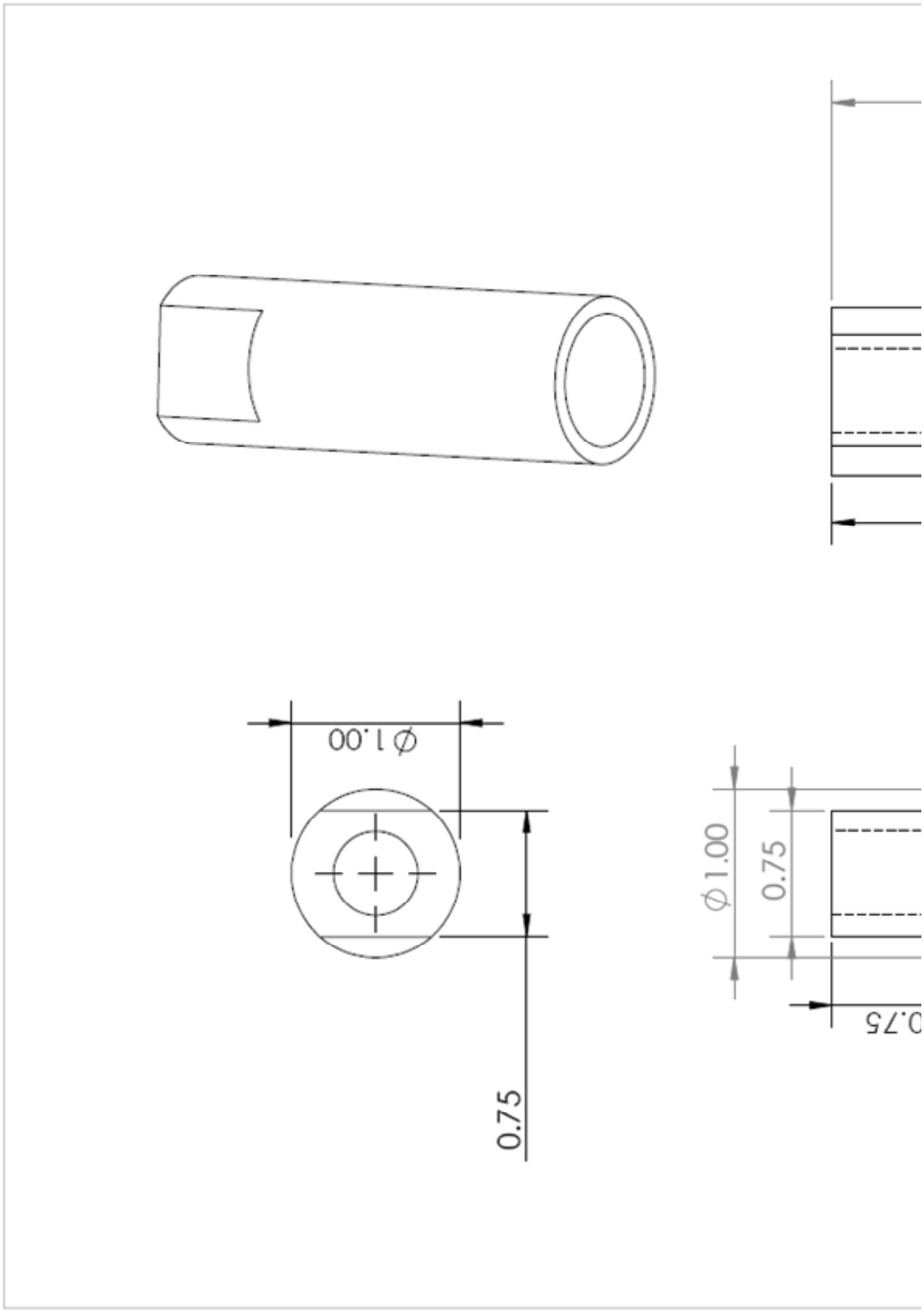

Figure B.2. Technical drawing of proppant crush test cell tube.

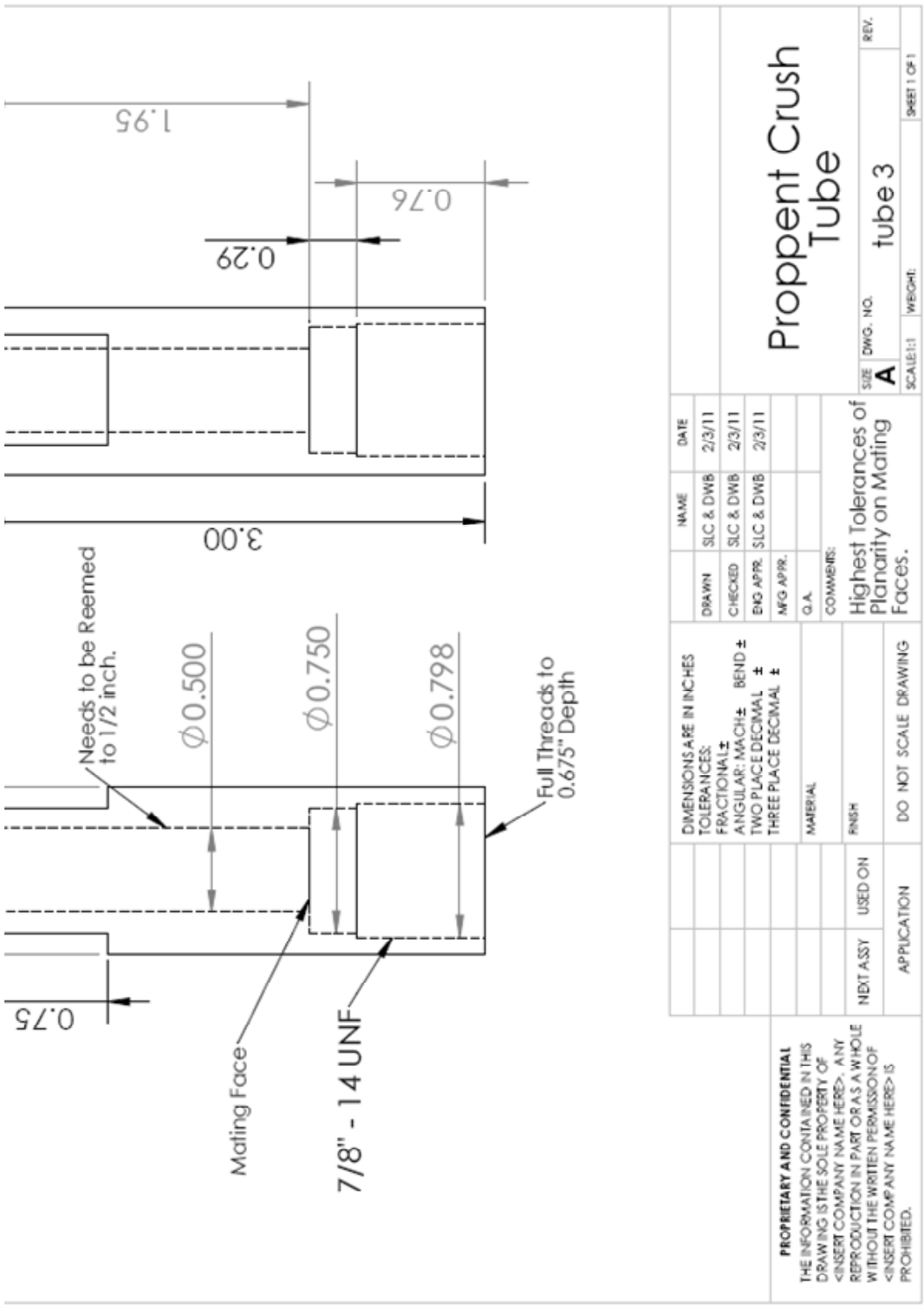

Figure B.2 (continued).

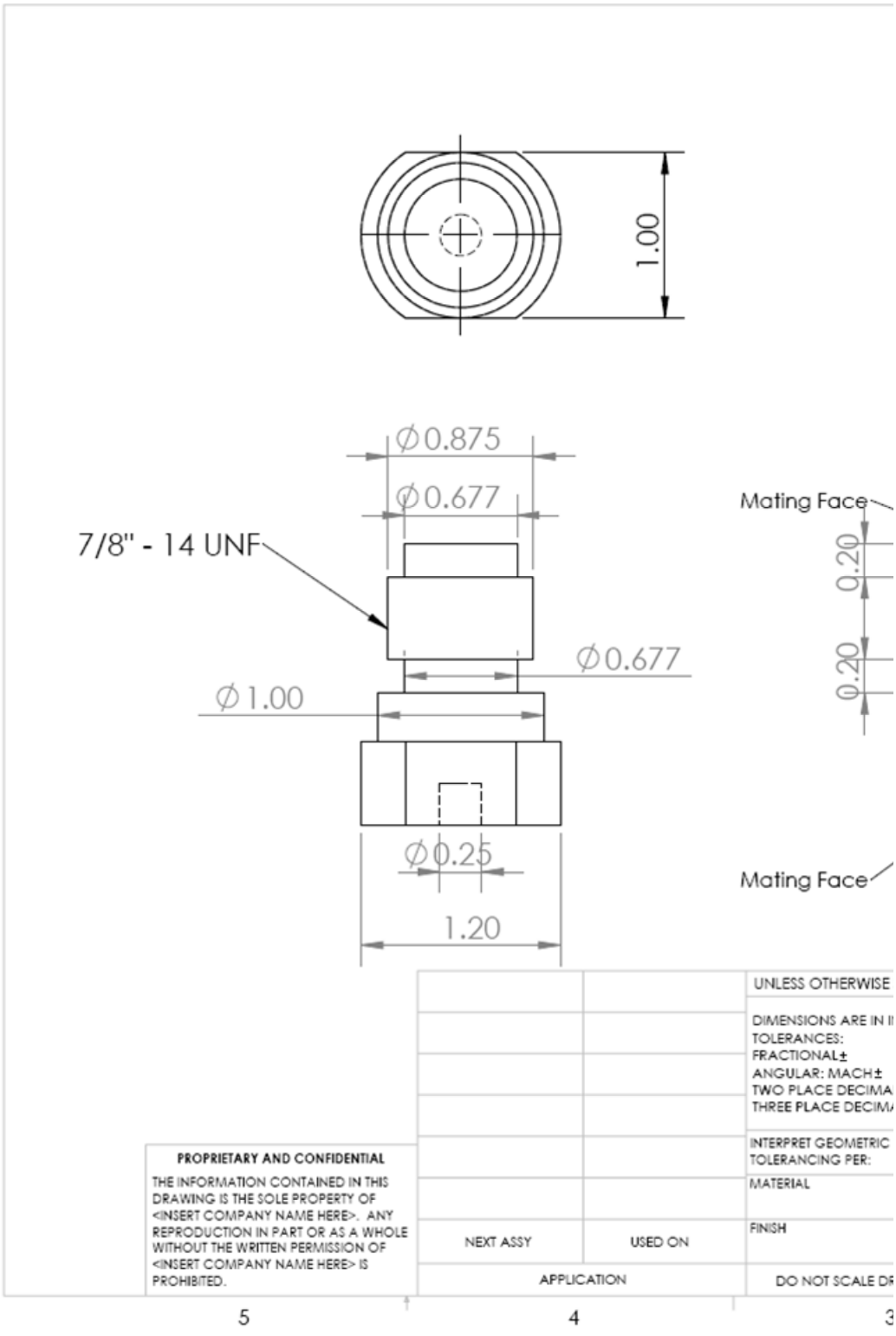

Figure B.3. Technical drawing of proppant crush test cell plug.

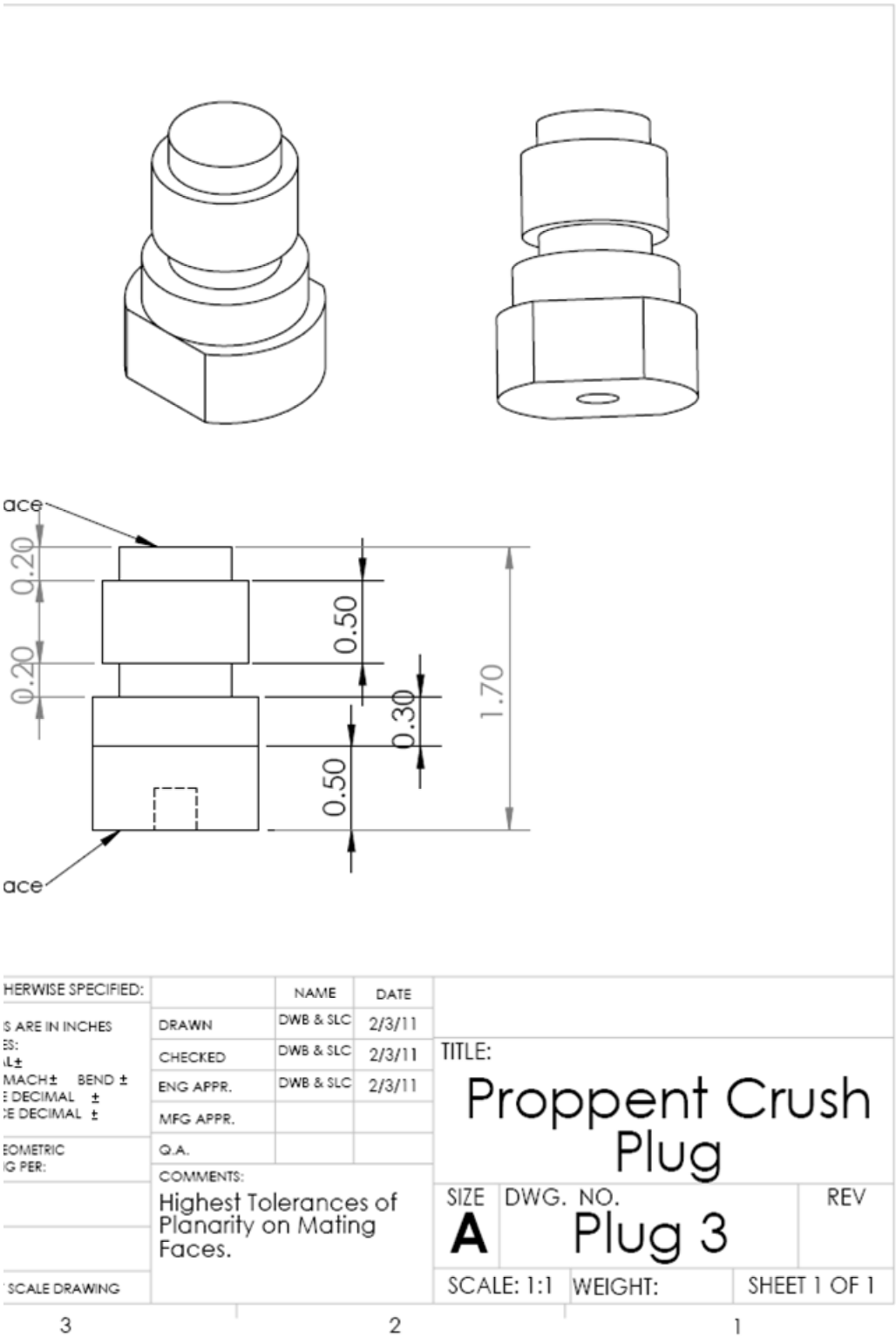

Figure B.3 (continued).

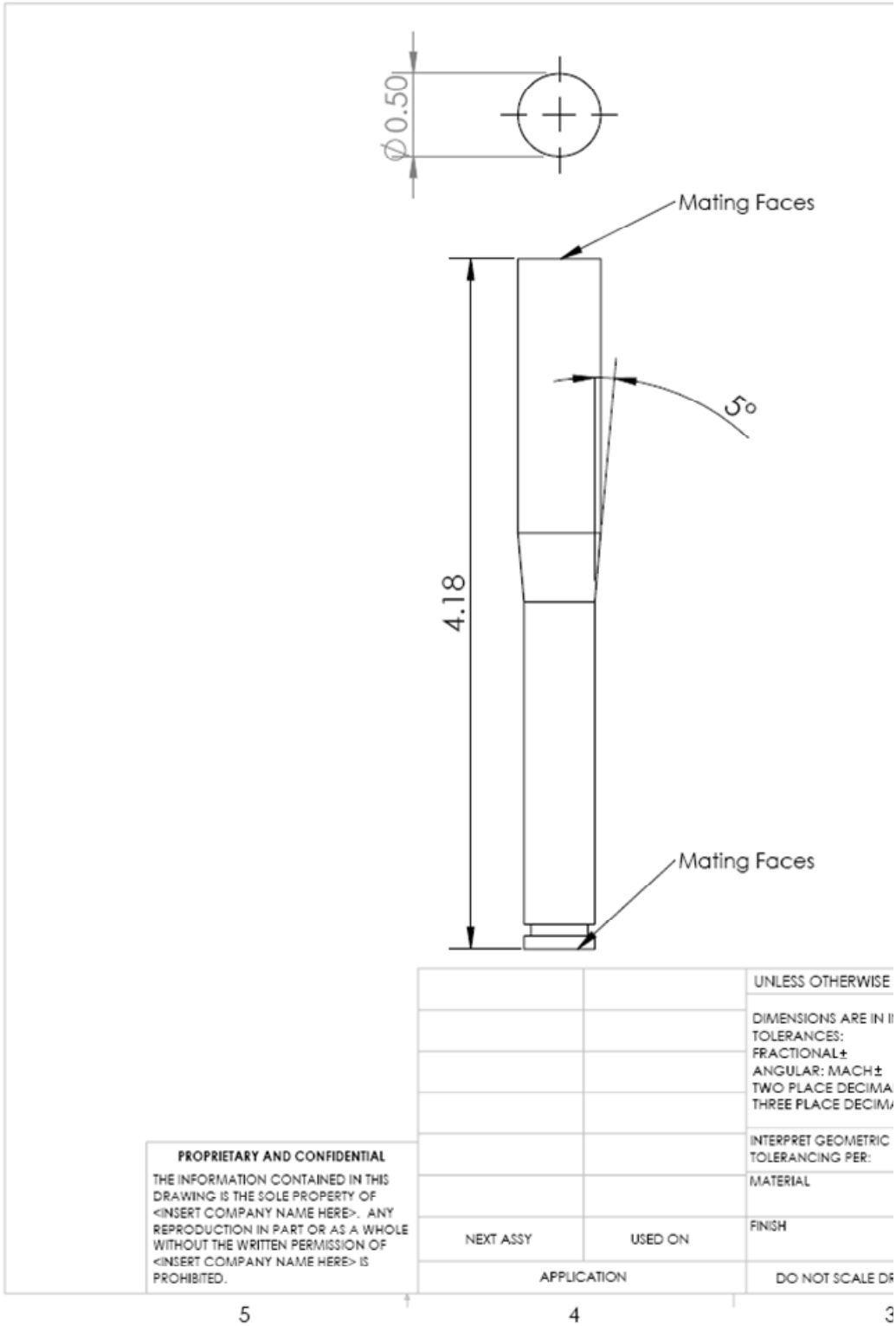

Figure B.4. Technical drawing of proppant crush test cell rod.

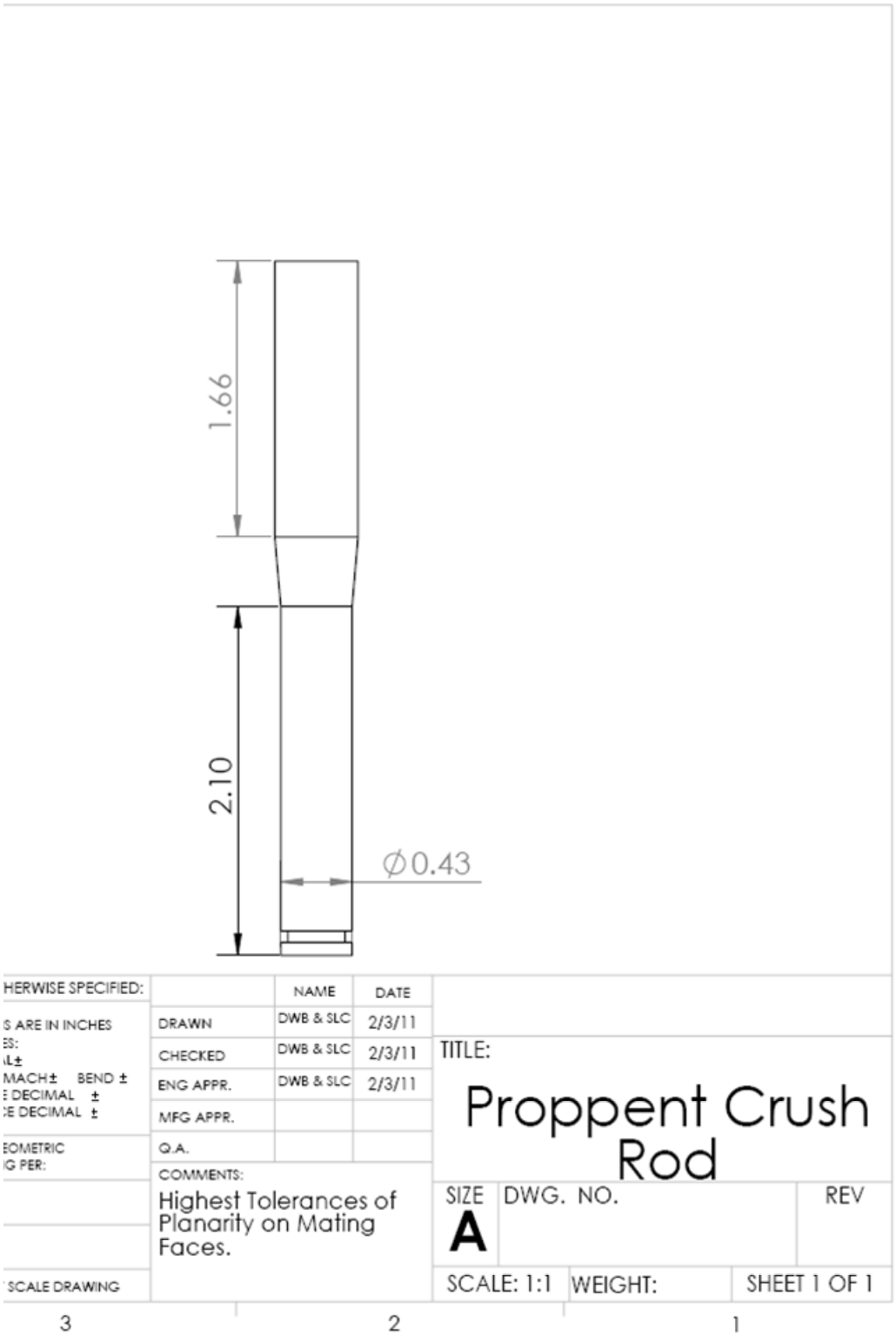

Figure B.4 (continued).

REFERENCES

Adams, M. C.; Ahn, J. H.; Bentley, H.; Moore, J. N.; Veggeberg, S. Tracer Developments: Results of Experimental Studies. *Proceedings of the Eleventh Workshop on Geothermal Reservoir Engineering*, Stanford University, Stanford, CA, Jan 21–23, 1986.

Atteberry, R. D.; Tucker, R. L.; Ritz, J. W. Application of Sintered Bauxite Proppants to Stimulation of Low Permeability South Texas Gas Reservoirs. *Proceedings of the SPE Symposium on Low-Permeability Gas Reservoirs*, Denver, CO, May 20–22, 1979.

Baria, R.; Baumgärtner, J.; Gérard, A.; Jung, R.; Garnish, J. European HDR Research Programme at Soultz-sous-Forêts (France) 1987–1996. *Geothermics* **1999,** *28* (4–5), pp 655–669.

Blackett, R. E.; Kolesar, P. T. Geology and Alteration of the Raft River Geothermal System, Idaho. *Trans. - Geotherm. Resour. Counc.* **1983,** *7,* pp 123–127.

Brocher, T. M. Empirical Relations between Elastic Wavespeeds and Density in the Earth's Crust. *Bull. Seismol. Soc. Am.* **2005,** *95* (6), pp 2081–2092.

Campbell, D. A.; Hanold, R. J.; Sinclair, A. R.; Vetter, O. J. A Review of the Geothermal Reservoir Well Stimulation Program. *Proceedings of the International Geothermal Drilling and Completions Technology Conference*, Albuquerque, NM, Jan 21, 1981.

Chang, C.; Zoback, M. D.; Khaksar, A. Empirical Relations Between Rock Strength and Physical Properties in Sedimentary Rocks. *J. Petrol. Sci. Eng.* **2006,** *51* (3–4), pp 223–237.

Covington, H. R. Subsurface Geology of the Raft River Geothermal Area, Idaho. *Trans. - Geotherm. Resour. Counc.* **1980,** *4,* pp 113–115.

Crampin, T. Well Log Facies Classification for Improved Regional Exploration. *Explor. Geophys. (Collingwood, Aust.)* **2008,** *39,* pp 115–123.

Davis, J. C. *Statistics and Data Analysis in Geology*, 3rd ed.; John Wiley and Sons: New York, 2002.

Duchane, D.; Brown, D. Hot Dry Rock (HDR) Geothermal Energy Research and Development at Fenton Hill, New Mexico. *Geoheat Cent. Bull.* **2002,** *23* (4), pp 13–19.

Dunteman, G. H. *Principal Components Analysis;* Sage Publications: Newbury Park, CA, 1989.

Ellis, D. Formation Porosity Estimation from Density Logs. *Petrophysics* **2003,** *44* (5), pp 306–316.

Ellis, D. *Well Logging for Earth Scientists;* Elsevier: New York, 1987.

Entingh, D. J. Geothermal Well Stimulation Experiments in the United States. *Proceedings of the World Geothermal Congress*, Kyushu-Tohoku, Japan, May 28–June 10, 2000.

Fournier, R. O. Application of Water Geochemistry to Geothermal Exploration and Reservoir Engineering. In *Geothermal Systems: Principals and Case Histories;* Rybach, L., Muffler, L. J. P., Eds.; Wiley: Chichester, U.K., 1981, pp 109–143.

Fournier, R. O.; Potter, R. W. A Revised and Expanded Silica (Quartz) Geothermometer. *Geoth. Res. Counc. Bull*. **1982,** *11* (10), pp 3–12.

Freeman, E. R.; Anschutz, D. A.; Rickards, A. R.; PropTester, Inc.; Callanan, M. J. Modified API/ISO Crust Tests with a Liquid-Saturated Proppant Under Pressure Incorporating Temperature, Time and Cyclic Loading: What Does It Tell Us? *Proceedings of the SPE Hydraulic Fracturing Technology Conference*, The Woodlands, TX, Jan 19–21, 2009.

Genter, A.; Fritsch, D.; Cuenot, N.; Baumgärtner, J.; Graff, J-J. Overview of the Current Activities of the European EGS Soultz Project: From Exploration to Electricity Production. *Proceedings of the Thirty-Fourth Workshop on Geothermal Reservoir Engineering*, Stanford University, Stanford, CA, Feb 9–11, 2009.

Gill, D.; Shomrony, A.; Fligelman, H. Numerical Zonation of Log Suites and Logfacies Recognition by Multivariate Clustering. *AAPG Bull.* **1993,** *77* (10), pp 1781–1791.

Gonçalves, C. A. Lithologic Interpretation of Downhole Logging Data From The Côte D'Ivoire-Ghana Transform Margin: A Statistical Approach. *Proc. Ocean Drill. Program: Sci. Results* **1998,** *159,* pp 157–170.

Handbook of Mineralogy. http://www.handbookofmineralogy.org (accessed 2011).

Hearst, J. R.; Nelson, P. H. The Well Logging Technology. In *Well Logging for Physical Properties;* McGraw-Hill Book Company: New York, 1985; pp 3–18.

Hilchie, D. W. *Applied Openhole Log Interpretation for Geologists and Engineers;* Douglas W. Hilchie, Inc.: Golden, Colorado, 1982 (revised).

ISO 13503. *Petroleum and natural gas industries – Completion fluids and materials - Part 2: Measurement of properties of proppants used in hydraulic fracturing and gravel-packing operations*, 1st ed.; 2006.

Johnson, G. W.; Ehrlich, R.; Full, W. Principal Components Analysis and Receptor Models. In *Introduction to Environmental Forensics,* 1st ed.; Murphy, B. L., Morrison, R. D., Eds.; Elsevier Academic Press: Burlington, MA, 2001; pp 488–494.

Knox, J. A.; Weaver, J. D. A Solution to Proppant Dissolution in Hydrothermal Environments. *Proceedings of the Fourteenth Workshop on Geothermal Reservoir Engineering*, Stanford University, Stanford, CA, Jan 24–26, 1989.

Lim, J-S.; Kang, J. M.; Kim, J. Multivariate Statistical Analysis for Automatic Electrofacies Determination from Well Log Measurements. *Proceedings of the SPE Asia Pacific Oil and Gas Conference*, Kuala Lampur, Malaysia, April 14–16, 1997.

Maurer Engineering Inc. *Geothermal Fracture Stimulation Technology: Volume 2. High Temperature Proppant Testing*; DOE/AL/10563-T8(Vol.2); US Department of Energy: 1980.

Maurer Engineering Inc. *Geothermal Fracture Stimulation Technology: Volume 4. Proppant Analysis at Geothermal Conditions*; DOE/AL/10563-T8(Vol.4); US Department of Energy: 1981.

Miesch, A. T. Q-Mode Factor Analysis of Geochemical and Petrologic Data Matrices with Constant Row Sums. *U.S. Geol. Surv. Prof. Pap*. **1976,** *574G*.

Mineralogy Database. http://www.webmineral.com (accessed 2011).

Moline, G. R.; Bahr, J. M. Estimating Spatial Distribution of Heterogeneous Subsurface Characteristics by Regionalized Classification of Electrofacies. *Math. Geol.* **1995,** *27* (1), pp 3–22.

Ngothai, Y.; O'Neil, B.; Kuncoro, G.; Pring, A.; Brugger, J. *Geochemistry, Corrosion and Scaling in Hot Dry Rock Energy Extraction Systems*. Final Report: AGEG Tied Grant 4.1; 2009.

Perkins, T. K.; Gonzalez, J. A. The Effect of Thermoelastic Stresses on Injection Well Fracturing. *SPE J. (Soc. Pet. Eng.)* **1985,** *25* (1), pp 78–88.

Peterson, P. E.; Van Buskirk, R. G.; Prater, F. M.; Muller, C. S.; Bergosh, J. L. *Final Report – Laboratory Testing of Core Materials from the Raft River Geothermal*

Site; Technical Report Submitted to the US Department of Energy Division of Geothermal Energy, TR 81-75; 1982.

Pribnow, D. F. C.; Sass, J. H. Determination of Thermal Conductivity for Deep Boreholes. *J. Geophys. Res.* **1995,** *100* (B6), pp 9981–9994.

Sinclair, A. R. High Temperature Proppants and Fluids for Geothermal Well Stimulation. *Proceedings of the Geothermal Reservoir Well Stimulation Symposium*, San Francisco, CA, Feb 7, 1980.

Stoddard, T.; McLennan, J.; Moore, J. Fracture Conductivity of Bauxite-Propped Geothermal System at In-Situ Conditions. *Proceedings of the Thirty-Sixth Workshop on Geothermal Reservoir Engineering*, Stanford University, Stanford, CA, Jan 31–Feb 2, 2011.

Tavakoli, V.; Amini, A. Application of Multivariate Cluster Analysis in Logfacies Determination and Reservoir Zonation, Case Study of Marun Field, South of Iran. *J. Sci. Univ. Tehran, Int. Ed.* **2006,** *32* (2), pp 69–75.

Tester, J. W.; Potter, R. M. Fractured Geothermal Reservoir Growth Induced by Heat Extraction. *SPE Reservoir Eng*. **1989,** *4* (1), pp 97–104.

Tester, J. W.; Smith, M. C. Energy Extraction Characteristics of Hot Dry Rock Geothermal Systems. *Proceedings of the Twelfth Intersociety Energy Conversion Engineering Conference,* Washington, D.C., Aug 28–Sept 2, 1977.

Weaver, J. D.; van Batenburg, D. W.; Parker, M. A.; Nguyen, P. D. Sustaining Conductivity. *Proceedings of the SPE International Symposium and Exhibition on Formation Damage Control*, Lafayette, LA, Feb 15–17, 2006.

Williams, C. F. Heat and Fluid Flow within the Earth's Crust: In Situ Measurements and Mathematical Models. Doctoral Dissertation, Columbia University, New York, 1989.

Williams, C. F.; Anderson, R. N. Thermophysical Properties of the Earth's Crust: In Situ Measurements From Continental and Ocean Drilling. *J. Geophys. Res.* **1990,** *100* (B6), pp 9209–9236.

Xu, R.; Wunsch, D. C. *Clustering;* Wiley: Hoboken, NJ, 2009.